Kent Academic Repository

PhD thesis title: EEG-Based Mental States Identification

Number of pages: 220

Abstract:
In this thesis, we focus on the identification of mental states described according to the definition of awareness and wakefulness. Using algorithmic methods, we show that it is possible to differentiate between two brain states based on the brain electrical activity collected by EEG. We begin by explaining the overall theoretical framework which enabled us to develop the detection of brain states. It starts with data acquisition. Following that, we analyse the pre-processing of the data before the extraction of features. Finally, we go on to statistically evaluate the results. In order to achieve this task, we propose four experiments. We will first focus on exploring different brain states for patients in Intensive Care Unit (ICU) such as coma and quasi-brain-death states. To distinguish these states, we use a signal processing method based on the EEG signal phase. A phase synchrony index based on Shannon entropy was used to separate the two states. Statistical validation revealed a significant difference between the two via delta-alpha and theta-alpha frequency couplings. Next, we studied the neuronal mechanisms which is used to understand consciousness. We did that by using dipole modelling. This method was applied to local-global experiment and the paradigm of auditory deviance with two hierarchical levels. A modulation of this experiment is generated by a sedative Propofol to study the effect on conscious states. This experiment was analysed in greater detail using the Imaging Method to do the source localisation. We analysed three different time-windows. The first window corresponds to the local effect during the initial response of the brain. We assume that this input is related to auditory areas and activates the temporal lobe. The second window is at the interface between the local effect and the global effect. In here we are especially interested in the interaction between these two effects during the second window. Finally, the third window will enable us to study the overall effect. We hypothesize a global activation of neural networks corresponding to consciousness as described by the global workspace theory. The third experiment focused on brain states high-level athletes experience during a cognitive task. Two different groups of cyclists, endurances and sprinters, were asked to do a Stroop task for 30 minutes. We studied the influence of the task and the potential differences in brain activity between the two groups. We found through the frequency analysis that the brain activity between the two groups can be distinguished, but was not modified by the cognitive task. Finally, we studied the influence of the sensorimotor loop on the brain. A physical task was applied, consisting in lifting a weight with two measurements, where the lifting arm can also be in fatigued state. Using sources reconstruction from EEG, we studied the impact of weight-lifting and the physical fatigue upon neuronal activities and the neuronal origins of these effects. We found that only weight has an effect, whereas fatigue effect is not significant. We conclude with a discussion of the mechanisms of consciousness analysed via algorithmic methods and some future work for the possibility to distinguish better between different cognitive states.

Date of submission: February 2019

Adrien Witon

Faculty of science – School of computing

EEG-BASED MENTAL STATES IDENTIFICATION

A THESIS SUBMITTED TO

THE UNIVERSITY OF KENT

IN THE SUBJECT OF COMPUTER SCIENCE

FOR THE DEGREE

OF PHD.

By

Adrien J-B. Witon

February 2019

Abstract

In this thesis, we focus on the identification of mental states described according to the definition of awareness and wakefulness. Using algorithmic methods, we show that it is possible to differentiate between two brain states based on the brain electrical activity collected by EEG. We begin by explaining the overall theoretical framework which enabled us to develop the detection of brain states. It starts with data acquisition. Following that, we analyse the pre-processing of the data before the extraction of features. Finally, we go on to statistically evaluate the results. In order to achieve this task, we propose four experiments.

We will first focus on exploring different brain states for patients in Intensive Care Unit (ICU) such as coma and quasi-brain-death states. To distinguish these states, we use a signal processing method based on the EEG signal phase. A phase synchrony index based on Shannon entropy was used to separate the two states. Statistical validation revealed a significant difference between the two via delta-alpha and theta-alpha frequency couplings.

Next, we studied the neuronal mechanisms which is used to understand consciousness. We did that by using dipole modelling. This method was applied to local-global experiment and the paradigm of auditory deviance with two hierarchical levels. A modulation of this experiment is generated by a sedative Propofol to study the effect on conscious states. This experiment was analysed in greater

detail using the Imaging Method to do the source localisation. We analysed three different time-windows. The first window corresponds to the local effect during the initial response of the brain. We assume that this input is related to auditory areas and activates the temporal lobe. The second window is at the interface between the local effect and the global effect. In here we are especially interested in the interaction between these two effects during the second window. Finally, the third window will enable us to study the overall effect. We hypothesize a global activation of neural networks corresponding to consciousness as described by the global workspace theory.

The third experiment focused on brain states high-level athletes experience during a cognitive task. Two different groups of cyclists, endurances and sprinters, were asked to do a Stroop task for 30 minutes. We studied the influence of the task and the potential differences in brain activity between the two groups. We found through the frequency analysis that the brain activity between the two groups can be distinguished, but was not modified by the cognitive task.

Finally, we studied the influence of the sensorimotor loop on the brain. A physical task was applied, consisting in lifting a weight with two measurements, where the lifting arm can also be in fatigued state. Using sources reconstruction from EEG, we studied the impact of weight-lifting and the physical fatigue upon neuronal activities and the neuronal origins of these effects. We found that only weight has an effect, whereas fatigue effect is not significant.

We conclude with a discussion of the mechanisms of consciousness analysed via algorithmic methods and some future work for the possibility to distinguish better between different cognitive states.

Acknowledgements

I first want to thank my supervisors Caroline Ling Li and Howard Bowman who restlessly provided me with guidance and advices. They have been of great help all along my PhD and allowed me to develop a critical thinking and independent research activity. I also thank to Samuele Marcola for inspiring conversations on fatigue. I am particularly grateful for the opportunities of research communication, either to conferences, or during informal meetings with different collaborators, particularly Tristan Bekinschtein, Srivas Chennu, Vladimir Litvak, Guillaume Flandin, Jose López and Karl Friston. I want to thank also Amiralli Beheshti and Jennifer Cooke who welcomed me at the beginning of my PhD, as well as my panel Sally Fincher, Alex Freitas and Dominique Chu.

As it was my first academic experience in UK, I greatly appreciated the British way of life and academic atmosphere at University of Kent. This was made possible by the different persons I interacted with: George Parish, William Jones, Alexia Zoumpoulaki, Luise Gootjes-Dreesbach, James Brookhouse, Sam Cramer, Ayah Helal, Tristan Strange, Ismael Mohamed, Olivier Perrotin, Ian McLoughlin, Janine Jarvis, Shannon Harris and those I forgot.

Particularly, I thank my family and dear friends for their support and patience during my doctoral years. Finally, I dedicate this thesis to my mother.

List of Publications

Journal Papers

- A. Witon, A. Shirazi-Beheshti, J. Cooke, R. Adapa, D. K. Menon, S. Chennu, T. Bekinschtein, J. López, V. Litvak, L. Li, K. Friston, and H. Bowman. Localising the Local-Global: Fronto-Temporal Sources and Propofol Modulation of the Double Surprise Acceleration Effect. (in preparation)

- A. Shirazi-Beheshti, J. Cooke, S. Chennu, R. Adapa, D. K. Menon, A. Hojjat, A. Witon, L. Li, T. Bekinschtein, and H. Bowman. Placing Meta-stable States of Consciousness within the Predictive Coding Hierarchy: the Deceleration of the Accelerated Prediction Error. Consciousness and Cognition, 2018 (request for revisions).

- A. Witon, S. Marcora, H. Bowman and L. Li. Review on Effort Based and Resting EEG Measure of Fatigue. (in preparation)

- A. Witon, H. Bowman, and L. Li. Investigating the Within-Frequency and Cross-Frequency Phase Synchrony for Unconsciousness with a Strategy to Correct Multiple Comparison Problem. (in preparation)

Conferences Papers

- M. Berthelot, A. Witon, and L. Li, Unconsciousness State Identification Using Phase Information Extracted by Wavelet and Hilbert Transform. International Conference on Digital Signal Processing (DSP) 2017.

- L. Li, A. Witon, S. Marcora, H. Bowman, and D. Mandic, D. EEG-based Brain Connectivity Analysis of States of Unawareness. Engineering in Medicine and Biology Society (EMBC), 36th Annual International Conference of the IEEE, 1002-1005, 2014.

Abstracts

- A. Witon, A. Shirazi-Beheshti, H. Bowman and L. Li, Un-Mixing Components of a Hierarchical Auditory Paradigm from EEG Source Reconstruction. British Association on Cognitive Neuroscience (BACN) conference 2017. (poster presentation)

- A. Witon, W. Staiano, D. Martin, S. Hulson, S. Marcora, and L. Li, EEG Brain Waves During Cgnitive Load Reveal Differences of Cycling Expertise. Brain Informatics & Health (BIH), 2015.

- A. Witon, W. Staiano, D. Martin, S. Hulson, S. Marcora, and L. Li, EEG Disentanglement in Cortical Activity for Endurance and Sprinter Elite Cycling Athletes. 1st Endurance Research Conference, 2015, Chatham UK.

Contents

List of Tables

List of Figures

Chapter 1

Introduction

1.1 Chapter Outline

This introduction puts the boundaries for the thesis. First we present our initial approach of the scientific question we are dealing in this thesis, i.e. how EEG analysis can provides methods to distinguish between different mental states. Then, we present the contribution of the thesis, how these analysis will contribute to answer the scientific questions. Finally, we describe the organization of the thesis with the different chapters of research which have been done to answer the scientific question.

1.2 Problem Statement

Medical care is becoming an ever more important subject for our ageing and modern society. Moreover, mental health has a huge impact on society, as one out of four on average will have a mental health issue or neurological disorder during his/her life according to the WHO[1]. Research need to be conducted to investigate how different cognitive states in humans can be quantitatively measured. Cognitive states are defined by the brain state of one individual, either engaged in a particular cognitive activity, or in an idle resting state i.e. normal or pathological. This thesis investigates methods that can be used to identify between two different states. The aim is to find neuro-markers of conscious or unconscious states, and to produce a description of the variety of cognitive states. It is of particular interest to provide quantitative measures of cognitive states. With the following applications studied in this thesis, we raise for each of them a scientific question.

- In a clinical context, the identification of different pathological brain states is an important topic. One application is to distinguish between coma and brain death. It is challenging to implement brain death diagnosis accurately, mostly because of clinical issues: specialized procedures and trained medical doctors are needed. For example, some tests require a patient to have medical care instrument removed, or to be transported out of the Intensive Care Unit (ICU). These tests put the patient at risk. Is it possible to provide algorithmic tools to distinguish between these different levels of brain activity before the vital supportive care is removed?

- Another clinical application is related to cognitive states under anaesthesia. If the mechanism at a receptor level is well understood, consciousness during

---

[1]http://www.who.int/whr/2001/media_centre/press_release/en/

2

anaesthesia is difficult to monitor. It is, however, crucial to detect the loss of consciousness under anaesthesia for two reasons. 1) Be sure the patient is not aware of the current surgical operation. In anaesthesiology, the loss of consciousness is identified as a loss of motor control to verbal command. But even in lack of response, a patient can be conscious (Mashour and LaRock 2008). 2) Be sure the level of sedation is not too strong once the patient is unconscious, in order to not create side effects due to the drug. In these conditions, it is of utmost importance to understand the brain region activated during sedation and loss of consciousness. In this thesis, subjects were sedated and performed a hierarchical local-global auditory task. Then, how to monitor the effects of sedation and its role in loss of consciousness? How can a hierarchical auditory task be used to evaluate consciousness?

- The previous cases imply an impairment of cognitive activity for the brain states. The brain states of elite athletes present the opposite condition, i.e. subjects have developed skills after thousand hours of practice which may reflect in their brain activity. A better understanding of these states would allow new training practice and achievement monitoring. How can we distinguish EEG activity between groups of elite athletes?

- The last application of cognitive states detection is related more particularly to the sensory-motor loop, with subjects performing physical activity. In the first application, the subjects were in a resting state. In the second and third application, a mental task is done by the subject. In this application, subjects are performing a physical task of weightlifting. The lifting is performed with both an heavy and light weight and the arm lifting the weight can be in a normal condition of fatigued condition. The question is

to understand the effect of fatigue and weight during the lift experiment on the brain activity.

1.3   Proposed solution

The main goal of this research is to provide methods which are able to distinguish between different cognitive states. Therefore, methods are developed to study brain activity both at the scalp level and at the neuronal source level. They are also evaluated by advanced statistical procedures. The second objective is to understand the relationship between brain activity and cognition. The proposed solutions for these objectives of EEG-based detection of mental states lie in two different perspectives underlying study of consciousness. The first one explores cognitive states from level of consciousness. These levels of consciousness are useful to detect a global unified steady-state response of the brain. The second approach explores the mechanisms which can explain the manifestation of consciousness at a biological or neural level.

1.3.1   Levels of Consciousness Detection

We include our methods of mental state detection in the general framework of levels of consciousness proposed by Laureys (2005); Laureys and Schiff (2012). This framework allows us to describe different mental states in a two dimensional space, as shown in Fig. 1 with one level of consciousness related to wakefulness in x-axis, and in y-axis the content of consciousness related to awareness.

More particularly, this graph provides a high-level representation to study consciousness and mental states. It is particularly well adapted for a global measure of cognitive activity. EEG recorded on the scalp will be analysed to find specific
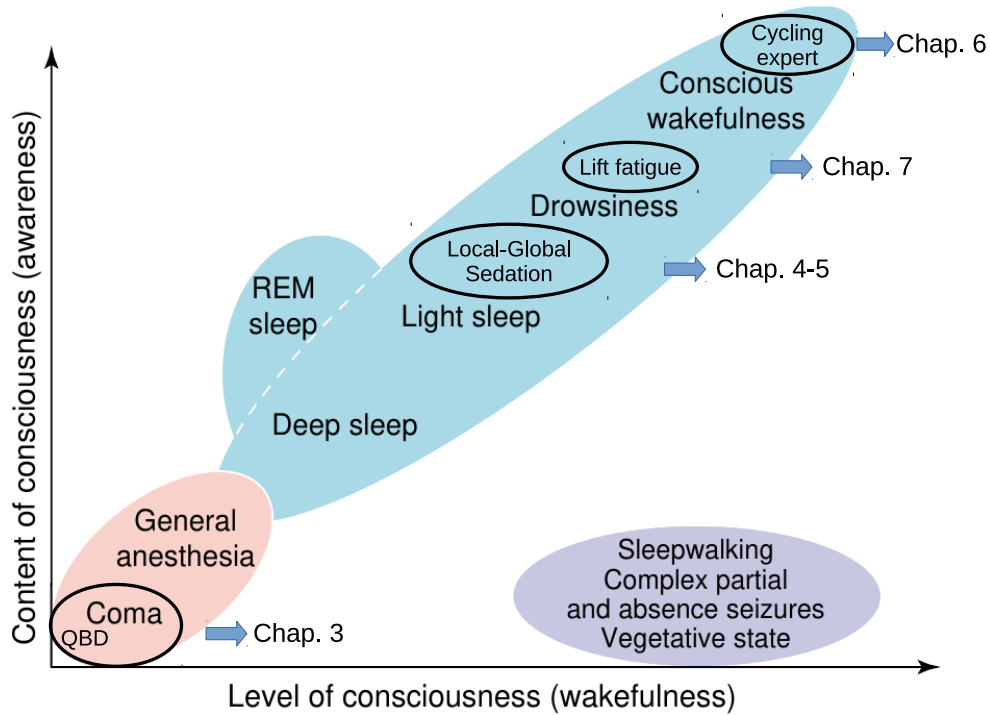
Figure 1: Illustration of two major components of consciousness. The x-axis is the level of consciousness as wakefulness and the y-axis represents the content of consciousness as awareness. Different states of consciousness are mapped, spanning along these two components. From low-level of consciousness to high-level, are presented successively coma, deep sleep, light sleep drowsiness and conscious wakefulness. In the context of this thesis the following states are studied: QBD vs coma, local and global effects modulated by sedation, a fatigue lift experiment and cycling expert states. The current mapping of these states is a preliminary proposition. Figure adapted from (Laureys 2005).

patterns related to cognitive states. The development of signal processing analysis applied to EEG provides new insight to broader mental states. Particularly, spectral analysis has long been applied to find patterns related to specific states. We do the hypothesis that brain activity of elite athletes exhibits different patterns of spectral power related to different groups of athletes.

Spectral analysis is a univariate method which does not take into account the relationship between brain areas. We then used phase information of the EEG

signal as a neuro-marker for brain states. Then, we applied Shannon entropy to study the phase synchrony between pairs of channels. We do the hypothesis that it is possible to find different phase synchrony index between states of coma and quasi-brain-death.

1.3.2   Modelling Access to Consciousness

If analysis at the scalp level allows distinguishing brain patterns, it does not provide an understanding of the relationship between different neural structures inside the brain. By doing analysis at the scalp level, there is no indication of neural source's location. Several methods have been developed to infer sources of EEG activity based on the scalp dataset. Using these methods, we looked at the structural connectivity at the source level to understand access to consciousness and mechanisms of brain integration.

Access to consciousness has a long history but gained scientific interest with the work of Baars (1988). Its main postulate is that conscious access is global information availability: what we perceive as conscious access is the selection, amplification and global communication to many distant areas, of a single object of perception selected for its relevance to current goals.

From a neuronal architecture standpoint as shown in Fig 2, two main computational spaces are distinguished within the brain, each characterized by a distinct pattern of connectivity, as developed in Dehaene et al. (2006). (1) A processing network, composed of a set of parallel, distributed and functionally specialized processors Baars (1988) in distinct cortical domains with highly specific local scale connections that process information relevant to its function. Processors typically operate in a bottom-up manner. (2) A global neuronal workspace (GNW),

consisting of a core network with a set of long-range connections characterized by their ability to bind together specialized circuits in a stable state to provide access to consciousness (Dehaene et al. 2006).
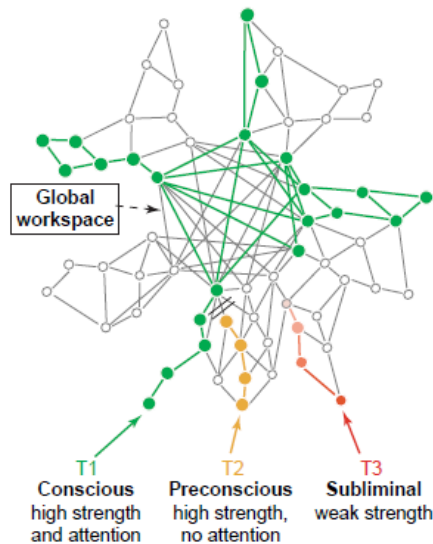
Figure 2: Global neuronal workspace. The global workspace defines a core of integrated neural circuits and peripheral neural circuits. When peripherals circuits are linked to the core circuit, a global workspace is ignited to give access to consciousness i.e. T1. When these peripherals circuits are not linked to the core circuit, only a preconscious (T2) or subliminal (T3) activation is available (Dehaene et al. 2006).

More recently, a theoretical framework has been developed to explain the role of neural circuits in the brain and how they can give rise to a unified representation of our world in a hierarchical level (Friston 2010). One hypothesis is the hierarchical communication between the cells assemblies. The different cortical structures communicate with each other by two directional pathways: a top-down and a bottom-up communication. On one hand, the cortical structures communicate from top-down with high-level neural processing, like concept representation, to more specialised cortical circuits, as sensory input. On the other hand, bottom-up communication originates from the low-level neural mechanisms, sensory input

to more complex or integrated circuits. A neural circuit received his input from a lower level circuit, and send information to a higher circuit for the bottom-up path. Then, it receives feedback from the higher circuit and also send at his turn feedback to the lower circuit for the top down path. The first path is also called feed-forward, where information as a prediction error goes from the lower sensory level to higher neural functions. While the opposite way is the backward or prediction path.
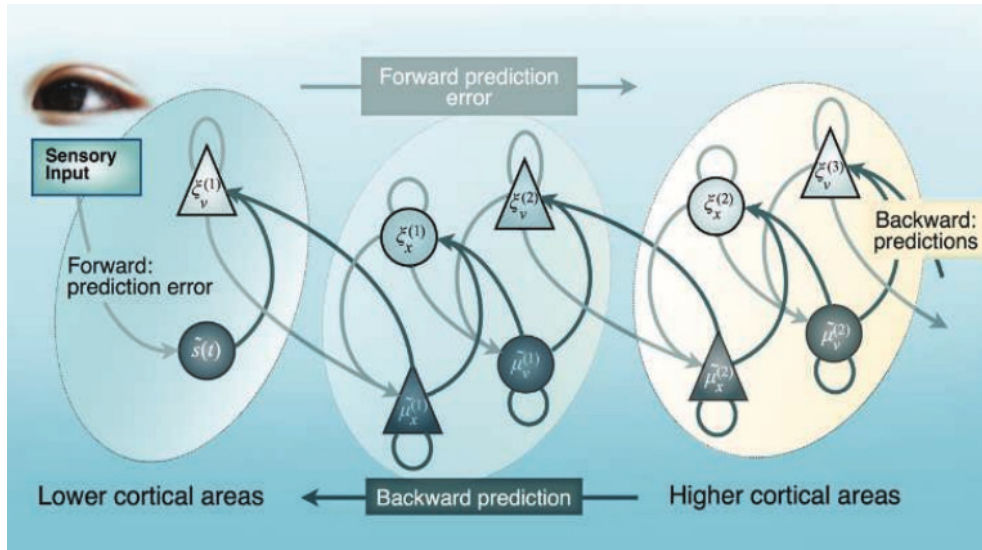
Figure 3: Predictive coding framework. Pathways of information are bottom-up (forward) and top-down (backward). Bottom-up process (starting from the left), sends information from lower levels (e.g. sensory input) to higher levels as a prediction error. Top-down process (starting from the right) sends information from higher levels to lower levels as a prediction of incoming information. Adapted from Park and Friston (2013).

Each circuit is hypothetically doing prediction of the forward message and send a backward message that is expected to reduce the prediction error, as shown in Fig. 3. Furthermore, the principle for this minimisation of error prediction, in order to keep the internal state coherent is called free energy (related to physical

statistic). This manages an equilibrium between the mental representation of our world and the information of the world we receive from our different sensory input, like vision and audition.

Based on source reconstruction applied on the local-global experiment, we explore the different levels of prediction due to the effects of local, global and sedation: in respect of brain sources, we plan to observe a progression from a localised (local effect) prediction hierarchy to a brain-scale meta-stable state (global effect). We will source localise where in the brain the transition between these two, which we postulate is an additional intermediate phase, resides in the brain. Finally, if sedation can influence these states, we will be able to localise from which source it originates.

We also applied the same framework to a lift experiment. We plan to evaluate neural activity for these effects. Then, we expect to detect an effect of physical fatigue and/or for different weights during the physical activity.

1.4 Contribution of the Thesis

In this work, different EEG methods have been applied to investigate mental states. Different experimental design have been used to investigate brain states under different stimulations.

- To evaluate the state of art in mental state detection, we made an exhaustive review of mental state detection applied to mental fatigue. Review on EEG-based detection of mental fatigue (Witon et al. 2016), as shown in Chapter 2.

- We applied phase synchrony analysis on coma state and quasi-brain-death (QBD) and show the phase synchrony index can be a marker for brain states

detection (Li et al. 2014; Berthelot, Witon and Li 2017; Witon, Bowman and Li. 2018), as shown in Chapter 3.

- We applied dipole modelling to explain the local deviant and global deviant conditions, as shown in Chapter 4. By analysing the local-global experiment modulated by sedation, we developed a three phases theory which combines global workspace theory and predictive coding, as shown in Chapter 5. It has been presented at the BACN conference (poster) (Witon et al. 2017), and detailed results are being published in a journal paper (Witon et al. 2018).

- For fatigue studies, we show that spectral power analysis can discriminate between a group of endurance cycling and sprinter cycling (Witon et al. 2015a,b), as shown in Chapter 6. Preliminary results of the lift experiment show a weight effect in the different sources. The time-course decomposes the muscle-related cortical potential between different sources and gives insights into the contribution of each source during lifting, as shown in Chapter 7.

1.5 Organization of the Thesis

The thesis is organized as shown in Fig. 4 with the analysis workflow. **Chapter 2** describes the methodology used for a study of cognitive state, and we focus the literature review on mental fatigue as a case study. **Chapter 3** illustrates the connectivity analysis at the scalp level between Coma and QBD states, based on the phase synchrony analysis. Due to the analysis of multiple pairs of electrodes, we also propose a statistical measure to deal with multiple comparisons which is less conservative than Bonferroni correction. **Chapter 4** presents the
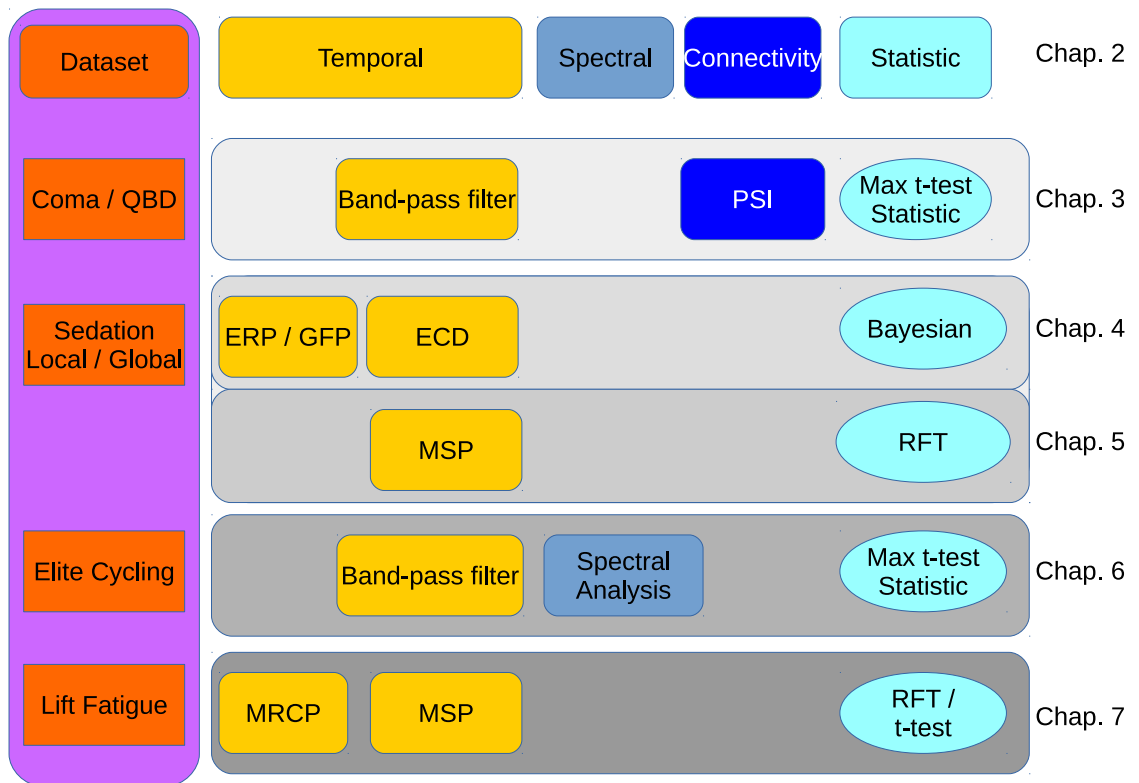
Figure 4: Analysis workflow for mental state identification. The first column represents the datasets used for analysis. For each experiment, the row describes which methods are used in the analysis. Analysis can be temporal, spectral or using connectivity, with a final column for the statistical method used. The link between a chapter and its corresponding analysis is presented in the last column. QBD: Quasi-Brain-Death, PSI: Phase Synchrony Index, ERP: Event-Related Potential, GFP: Global Field Power, ECD: Equivalent Current Dipole, MSP: Multiple Spare Priors, MRCP: Muscle Related Cortical Potential, RFT: Random Field Theory.

methods of source reconstruction and initial results based on Equivalent Current Dipole, for the local-global experiment. **Chapter 5** provides a full analysis of source reconstruction of the local-global experiment with Multiple Spare Priors (MSP) imaging method. A full second-level statistical analysis is applied to

find the activated neural sources for the different effects (local, global and sedation) as well as the interaction, in the early, middle and late processing of the ERP response. **Chapter 6** evaluates the spectral analysis during cognitive task between endurance and sprinter elite athlete and shows a statistical difference between athletes. **Chapter 7** provides source reconstruction analysis on muscle related cortical potential during a physical activity. Two factors are studying: a weight lift and an arm fatigued factors, with a significant weight effect. Finally, **Chapter 8** concludes the thesis by highlighting how the three phases effect for the local-global experiment provides a framework that combines predictive coding and global workspace for access to consciousness. A further discussion proposes future research on consciousness.

Chapter 2

Literature Review on Identification of Mental States

2.1 Chapter Outline

We present in this review the general framework for mental states identification based on EEG dataset. It starts with data acquisition. Following that, we used data pre-processing techniques before the extraction of features. Finally, we go on to statistically evaluate the results. This framework is applied to mental fatigue to illustrate the different steps. We also present different datasets used for the thesis. These datasets were used to evaluate how different cognitive states can be differentiated from EEG with different methods analysis, from phase synchrony analysis to source reconstruction and power spectrum analysis.

2.2 Introduction

The development of new algorithms and the increase of computational power will lead to new opportunities for brain research. In collaboration with clinicians, it may open doors to a better understanding of consciousness which remains a mystery. There are many conscious and non-conscious events occurring continuously in the brain (Braboszcz and Delorme 2011), but not a clear distinction to differentiate between different conscious states has been made yet. However, recent clinical advances make it possible to distinguish minimal levels of consciousness from patients in coma state (Laureys 2005; Laureys and Schiff 2012). Also, brain patterns have been highlighted from different populations, between professional and non-professional musicians (Bhattacharya and Petsche 2005), elite sportive (Yarrow, Brown and Krakauer 2009) or long-term practitioners of meditation (Lutz et al. 2004). These studies illustrate the broad spectrum of research for mental states identification. A less studied mental state is the state of mental fatigue. Fatigue is a familiar feeling of exhaustion that everyone has experienced. It is a bridge between healthy mental states, i.e. ones at their average mental capacity, and weak mental states when a person is unwilling to perform activities. In this literature review, we describe the framework for EEG-based mental states identification. More particularly, this framework is applied to an exhaustive description of mental fatigue detection, as an illustration of how to apply the framework.

It is important to gain the domain-specific knowledge before data analysis framework can be applied to solve a problem. For example, mental fatigue, as defined by Grandjean (1988), is a decrease in alertness and an unwillingness to work. Research has shown that 20-30% of road accidents occur as a result of driver

fatigue Camkin (1990). Also, an estimated 0.2-0.4% adults worldwide Wessely, Hotpf and Sharpe (1998); Prins, Van der Meer and Bleijenberg (2006) are affected by Chronic Fatigue Syndrome (CFS), which has now become a public health issue. Some research suggests that patients with cancer are more likely to be fatigued (Prue et al. 2006), and affected patients have no willingness to accomplish activities. Although the same 'fatigue' terminology is used, the cause of fatigue and the underlying mechanisms may vary from one application to another. For example, mental fatigue occurring in car driving implies a transient decrease of attention. This fatigue state is different from the one found in CFS patients, which involves more motivational mechanisms.

To be able to assess fatigue, we are very much interested in the concept of workload and its relationship with fatigue. Indeed, the workload is one's cognitive resources required to accomplish a task and is commonly used to induce mental fatigue. The first attempt to investigate workload is the research of Fitts and dates back to the World War II studies to improve pilots' performance in the Air Force. Fitts later worked on human performance theory (Fitts and Posner 1967) in an attempt to quantify the amount of work a person is given by information theory (Shannon and Weaver 1949). If we quantify the cognitive task given to a pilot as his/her workload, the higher the complexity the task is, the more information a pilot needs to deal with. If such information exceeds the pilot's ability to process (cognitive overload), it may cause an accident and is always regarded as a preliminary factor of mental fatigue.

The following sections will describe how fatigue is assessed by examining workload and performance. Many cognitive tasks have been developed, e.g. sensorimotor tasks, such as the oddball task, which requires the subject to press a button

when an infrequent stimulus is presented. The number of correct responses measures the subject's performance. A subject's performance decreases with time, although the cognitive workload (the task) remains constant (Mackworth 1948). Attention should also be drawn to the process of fatigue and effort. When fatigue occurs, a subject has to put more effort in doing the task to maintain the same performance (Marcora, Staiano and Manning 2009). Therefore, the subject can get fatigued even quicker. To be able to understand the whole process and relationship between workload, effort and fatigue, researchers have used the electroencephalogram (EEG) to derive a quantitative indicator (neuro-marker) of fatigue, together with other measurements (subjective, behaviour and physiological measurements).

We then conduct a systematic review of existing methods on EEG-based mental states identification. The following sections describe the experimental design, data acquisition and analysis.

2.3   Data Acquisition

In order to perform data acquisition, controlled tasks to induce a particular mental state were required. In order to quantify one's physiological state, measurements from four categories can be considered. These include subjective measurement, behavioural measurement, physiological measurement of the body and in particular, physiological measurement of the brain, as shown in Fig. 5. The box in the first column lists cognitive tasks to induce a mental state, and physiological measurements are listed in the four boxes to the right of the figure. The accuracy of measurement evolves from low to high, as measure get closer to the organ's origin of the cognitive state. Acronyms are detailed in Appendix 1.
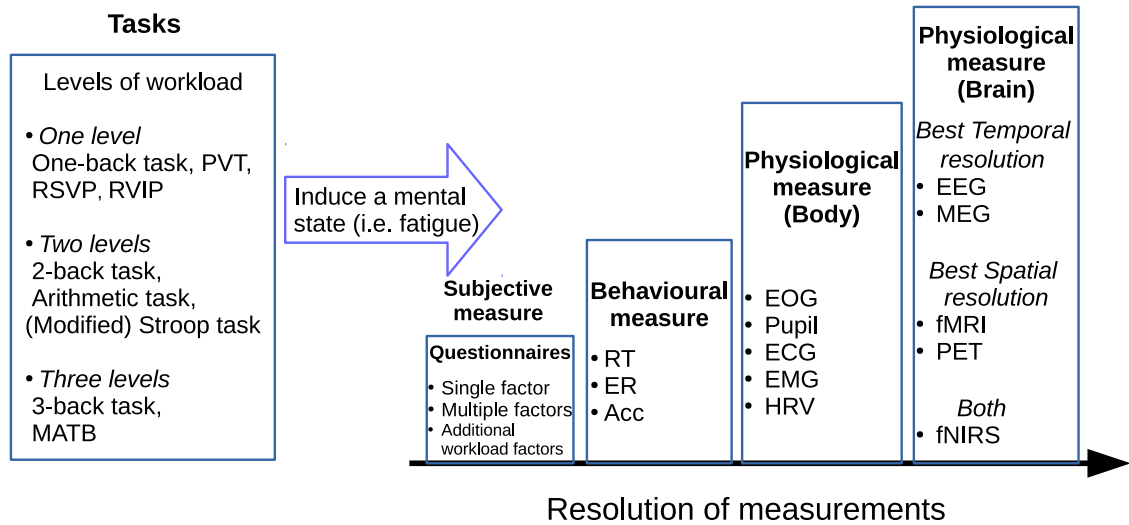
Figure 5: Process for cognitive states (e.g. fatigue) evaluation. To study mental states, one may present stimulus to induce a particular mental state. The workload tasks presented in the left panel produce stimuli. Different cognitive tasks have been available, and we can distinguish at least three levels of workload induced by these tasks. These tasks allow inducing the brain in a particular state, e.g. mental fatigue. From middle to right of the figure, four different measurements are proposed to evaluate the level of activity related to the task. These are subjective measures, behavioural measure, physiological measures (applied to body measurement) and physiological measures at the brain level. At the brain level, EEG provides the best temporal resolution, whereas fMRI offers the best spatial resolution. See Appendix 1 for a detailed meaning of acronyms.

2.3.1 Categories of Mental State Measurements

Subjective Measure

Subjective measurements are the feeling reported by subjects. Questionnaires can be designed to ask a subject about his/her feeling. In a fatigue scenario, questionnaires can be classified into three categories, dependent upon its simplicity. 1) A subject reports a number indicating the feeling of fatigue by a scale from

17

'not exhausted at all' to 'highly exhausted', as used in the Borg scale perceived exertion Borg (1982). A subject can also be asked to report a number indicating other feelings (sleepiness - Stanford Sleepiness Scale (SSS) Hoddes et al. (1973), Karolinska Sleepiness Scale (KSS) Akerstedt and Gillberg (1990)). It can be presented at the beginning, during (if available) and the end of the task, to report the level of fatigue they feel Liu, Zhang and Zheng (2010a).

2) Questionnaires can have multiples factors. It can ask a subject to report on a scale for each of the factors in the Activation-Deactivation Adjective Check List (wakeful, drowsy, active, energetic, calm, etc.) Thayer (1989); Lorist et al. (2009). This report is usually based on the scale of personal feeling 'right now', i.e. at the moment of questioning.

3) In addition to the above mentioned two types of questionnaires, subjects can also report the feeling of workload. To have a workload assessment, the following questionnaires, among others, can be used: NASA Task Load indeX (NASA-TLX) Hart and Staveland (1988), Subjective Workload Assessment Technique (SWAT) and Workload Profile (WP). A comparison study Rubio et al. (2004) has been performed on these three types of questionnaires using two different cognitive tasks. They have achieved similar results in general. However, when a subject is aware that cognitive effort required for the task will change, WP gives better score Rubio et al. (2004). Concerning the scale used in each of the questionnaires, WP uses eight different scales using the *resource model* of Wickens Wickens (2002). It includes stages of processing - perception/response, modality of processing - spatial/verbal, input - visual and auditory, output - manual and speech. Each of them is rated from 0 to 1. NASA-TLX uses six scales: Mental demand; physical demand; temporal demand; performance; effort and frustration. SWAT uses time-load; mental effort load; and psychological stress load. With, for each of these,

three scales to rate the perceived load of a subject.

Sometimes, subjective measurements are not possible. For example, a patient in coma/QBD is not able to describe his own mental state. Also in a sedation condition, a subject is introduced into a state of low consciousness. In the case we cannot rely on subjective report, behavioural measure can be used to evaluate how a subject respond to a task. We give detailed descriptions of behavioural measure in the following. Again, we used the fatigue case as an illustration.

Behavioural Measure

Typical behavioural measurement includes Reaction Times (RT), Error Rates (ER), and Accuracy (Acc). RT is reported to increase substantially with fatigue, e.g. in arithmetic tasks Liu, Zhang and Zheng (2010b) or Psycho-motor Vigilance Tasks (PVT) Sun et al. (2014) among others. The duration of a task to induce fatigue is usually referred as Time on Task (ToT). Error rates are reported to increase with ToTs requiring vigilance Mackworth (1948); Davies and Parasuraman (1982) and are associated with fatigue Liu, Zhang and Zheng (2010b).

Behavioural measurements give performance based on how a subject reacts to a stimulusor a task after a learning period. Two main approaches are used for this evaluation. The first one is to evaluate the performance at the beginning and the end. The difference between these two conditions indicates the effect of the workload. The second is to evaluate performance throughout the time course of the task, and the fatigue-inducing task itself can be used to evaluate the performance. The second approach gives a better temporal resolution and increases possibilities for analysis. In Fig. 6, these two are presented. The grey band represents the fatigue-inducing task, the hatched band is the task used for the quantification of fatigue (the two tasks could be the same), and the dark line
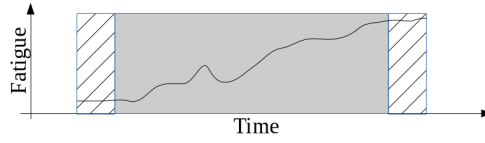
(a) Endpoint quantification of overall performance
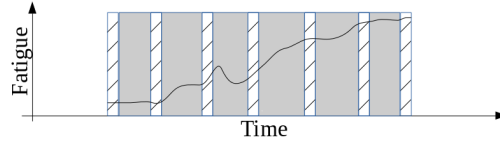
(b) Regular quantification of performance

Figure 6: Performance's quantification for cognitive studies. Two major evaluations of performance are available. (a) shows the case where the evaluation is done once at the beginning of the task and once at the end of the task. (b) shows an evaluation which is performed regularly during the task.

is the level of fatigue during the task.

Physiological Measure

Physiological measures take advantage of recent development in body sensors. Data can be recorded and analysed to quantify one's body and mind states. The movement of the eyes can be measured by electrooculography (EOG). Blink rate and blink duration significantly decrease with an increase of task complexity Borghini et al. (2014), but blink rate increases if drowsiness occurs in driving simulation Lal and Craig (2001). Pupil diameter decreased with ToT Hopstaken et al. (2014). Heart Rate, as well as power in low-frequency bands $[0.04-0.15Hz]$ of the Heart Rate Variability (HRV), increased with increasing workload Borghini et al. (2014). In fatigue studies, ECG showed a decrement in the lower frequency power, whereas an increment at the higher frequency power $[0.15-0.4Hz]$

of HRV Zhao et al. (2012). ECG Approximate Entropy (ApEn) increases during simulated driving tasks Zhao et al. (2012). For fatigue detection, electroencephalography (EEG) is widely used. EEG-detection will be discussed in detail in a later section.

By using functional brain imaging techniques, neuro-markers have been found to be related to fatigue. fMRI as an indirect measure of brain activity through the Blood-Oxygen-Level Dependent (BOLD) response, has shown a significant positive relationship ($p < 0.005$) in frontal regions in a cognitively demanding task compared to a non-fatiguing task (Cook et al. 2007). This is not specific to fatigue, for example, using Arterial Spin Labelling on functional magnetic resonance imaging (ASL-fMRI), Lim et al. (2010) shown a decrease of the fronto-parietal attentional network.

2.3.2   Cognitive Task Design

Cognitive task design is usually used to control an experiment, hence the underlying cognitive state. In the Cognitive Load Theory (Paas and Merrienboer 1994), Paas postulates that Working Memory (WM) is related to mental workload. The capacity of working memory has been first established by Miller in 1956 in his seminal paper (Miller 1956), he argued that only seven items can be maintained at the same time, while Cowan argues for 4 items, but the limit in a context of workload has not been elucidated yet. Instead, different levels of cognitively demanding tasks, usually up to three, are used to simulate different capacities. The process of working memory does not rely only on one anatomical structure but is most likely involved in a network comprising frontal and parietal

regions (Smith and Jonides 1999), which also have a role in the process of fatigue (Boksem and Tops 2008). Moreover, this network is linked to the vigilance network (Posner and Raichle 1994), which is directly impacted by fatigue (Mackworth 1948; Davies and Parasuraman 1982; Boksem, Meijmami and Lorist 2005) as reported by neuroimaging techniques (Lim et al. 2010). These research indicate that inducing fatigue by experimental design requires the cognitive task to have an impact on working memory load (Massar et al. 2010; Roy et al. 2013).

Within the cognitive psychology context, it has been argued mental workload to be the amount of cognitive capacity required by WM to perform a task (Paas and Merrienboer 1994). One significant difficulty in quantifying mental workload is the different amount of cognitive capacity available from individual to individual to perform a task. One example is related to driving: during a driving session, two subjects can have the same performance regarding the time to reach the goal, whereas one of the drivers could be at his maximum capacity, the other could be just at the middle of his. However, as the first task produces the same results in both subjects, a secondary concurrent task (Paas et al. 2003) additional to the primary workload task could be used to assess availability (or lack thereof) for cognitive resources. In a driving example, an oddball task, requiring the subject to pay attention to infrequent stimuli during driving, is a secondary concurrent task. This task is used to quantify the performance of the subject and could be compared to his feeling of fatigue due to his/her cognitive activity. Meanwhile, in most mental fatigue studies, the assessment of available cognitive resources is done by repeating the experiment on several sessions and varying the level of workload to increase the complexity of the task.

Cognitive workload tasks used for mental fatigue induction are as follows. 1) The Psychomotor Vigilance Task (PVT) which assessed sustained attention, as

the subject is asked to press a key when a target is presented in a random interval of few seconds. It is used in fatigue study, like in (Sun et al. 2014). 2) The N-back task, where N is the level of complexity of the task. Stimuli are presented with a randomly varying time interval. The subject is required to press a button if the presented stimulus is the same as the Nth previous stimulus. This stream: '*A Q **A** H F R T **R** K D*' is a 2-back task with salient stimuli in bold. As N increases (usually from 1 to 3), the task requires more workload to sustain in working memory the Nth N-back item. Different levels of complexity are available (up to N), as different back-tasks can be required during different sessions. 3) Multi-Attributes Task Battery (MATB) (Comstock and Arnegard 1992; Harris et al. 1995), is a remote aeroplane simulator developed by NASA, which presents six different panels. This task usually requires a few hours of training before a stable level of performance is reached. At this stage, various levels of complexity are available and can be utilised during a mental fatigue study.

4) Other cognitive tasks are also found in the literature, most often Go/NoGo tasks requiring a response to a congruent stimulus, or Stroop task (Gwizdka 2010) (or modified Stroop task). Arithmetic tasks have also been used to induce mental fatigue, as well as oddball paradigms (Zhao et al. 2012). Other tasks relying on the visual process like Rapid Serial Visual Presentation (RSVP) (Touryan et al. 2014), or Rapid Visual Information Presentation (RVIP) (Hilti et al. 2013) have been used for mental fatigue or sustained attention studies.

2.3.3 From Quasi-Brain-Death to Brain States of Elite Athletes

The thesis mainly focused on the measurement of the brain using EEG, due to its high temporal resolution and his particular applications which require time-varying monitoring of mental state evolutions. The data acquisition was performed on the following mental states.

1) Coma, QBD states (Chap 3): no task was used to induce the brain state. It was a natural progression due to pathological conditions.

2) Sedation, recovered states (Chap 4-5): the sedation state was introduced by using Propofol. The auditory task was given to subjects based on the local/global paradigm (Bekinschtein et al. 2009). It was used to control and understand the consciousness state.

3) Fatigue, non-fatigue (cognitive study) for two groups of athletes (sprinter/endurance cycling athletes) (Chap 6): the brain state of fatigue was induced via a cognitive task (Stroop task).

4) Fatigue, non-fatigue (physical study) (Chap 7): the physical fatigue was induced by physical exercise prior to the task in order to fatigue the arm's muscles.

We will elaborate more in following section, on the four mental states mentioned above.

Coma and QBD

The first dataset focussed on patients in Intensive Care Units (ICU) that suffer different levels of Disorders of Consciousness (DoC). Finding reliable neuro-markers from EEG recordings to distinguish brain states should be very useful. It is quite challenging to have an accurate view of the state of unawareness below the

deep coma to provide a precise diagnosis before brain death. We investigate the difference of brain activity between coma and QBD using multivariate analysis methods, based on phase synchrony.

Local-Global Experiment With Sedation

This second dataset consist of an auditory oddball with sedation experiment, and 18 participants were taken forward for analysis. EEG data was collected at two time-points, during sedation and then during recovery. The local-global auditory oddball task, devised by Bekinschtein et al. (2009), was implemented within this study. Local regularity was established using sequences of five tones, or quintuples, where the last tone may or may not very from the preceding four tones (deviant versus standard respectively). Furthermore, global regularity was established as the most frequently presented quintuple pattern (which may be standard or deviant). Violations in global regularity were expressed by the presentation of a quintuple that is not the frequently presented pattern. To ensure the establishment of global regularity, a habituation period of 20 to 30 quintuples was presented at the beginning of the experimental session. After the habituation period, 80% of the time participants were presented with standard quintuple, whilst the remaining 20% were deviant. This gives rise to four conditions, depending of presence/absence of local or global regularity: (1) local standard global standard (LSGS), (2) local deviant global standard (LDGS), (3) local standard global deviant (LSGD) and (4) local deviant global deviant (LDGD) and participants were asked to count the number of global deviants they heard.

Elite Endurance and Sprinter Cycling Athletes

The experiment was performed in collaboration with the Australia Institute of Sport and University of Canberra. The experiment consists of two groups. The first group had 10 participants who are elite endurance cyclists and the second group had 10 participants who are elite sprinter cyclists. The dataset consist of EEG recorded during resting state and a cognitive task. Each participant has been recorded for two minutes eyes open and two minutes eyes closed (resting state) before and after a 30 minutes cognitive task (Stroop task) performed on a computer. The task was selected to induce fatigue. The effects of time on task as well as the effect at the group level will investigated.

Lift Dataset Fatigue

For this study, 21 volunteers participated. The participants visited the laboratory twice. The first visit was a familiarization session, while the second visit was the experimental session. The first independent variable was weight: participants were asked to lift two weights based on the maximum weight (evaluated in preliminary session) they could lift, i.e. a lightweight and a heavier weight. The second independent variable was muscle fatigue, defined as an exercise-induced reduction in the ability to produce force with a muscle during a maximal voluntary contraction. Source reconstruction has been applied on the MRCP for each individual subject.

2.4   EEG Data Analysis Framework

The purpose of EEG-based mental states studies is to find a neuro-marker of brain activity related to the mental state. EEG is regarded as the best brain imaging

26

candidate due to its character of being portable, inexpensive, and having an excellent temporal resolution. Compared to other imaging modalities, like MEG or fMRI, an EEG system offers portability. EEG is currently the less expensive imaging modality system and systems available to a broad public. As mental fatigue results in the change of transient activity of neural sources, an excellent temporal resolution of EEG is needed to detect these events. EEG based mental state identification framework consist of a workflow of data acquisition, preprocessing, feature extraction and statistical evaluation, as shown in Fig. 7.
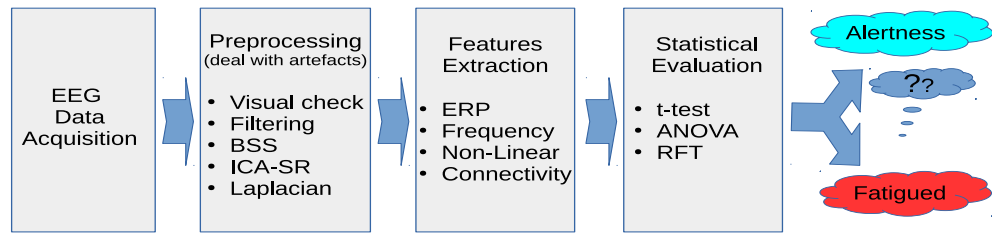
Figure 7: Workflow of mental states identification. Four elements are described for the workflow of mental states identification. It begins with the EEG acquisition (i.e. number of channels, sampling frequency). The second part is the preprocessing which is required to clean the data from artefact and to select trials with good signal to noise ratio. The third step is the features extraction, with with temporal, spectral, non-linear or connectivity analysis. Finally, the last step assesses if there is significantly difference between two mental states or conditions.

Brain activity can be recorded by the electric field produced by the neurons and propagated to the scalp. EEG signals result from the difference of potentials between electrodes placed on the scalp and a reference electrode (i.e. electrode on the earlobe). To study fatigue, the number of electrodes varies from as few as two electrodes (Jung et al. 1997) for a fatigue switch-based detector, up to

256 channels to take advantage of all the spatially features of the brain activities. A common practice is to follow the standardised 10-20 system, shown in Fig. 8, covering the main brain lobes homogeneously (Jasper 1958).
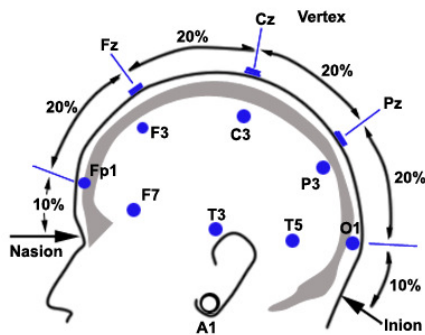
Figure 8: 10-20 System. The 10-20 system is a normalized procedure to place the channels in a regular distribution on the scalp, which covers the major brain areas: frontal, temporal, occipital and parietal.

2.5   Preprocessing

EEG signal has its advantage, but it also has its limitation. Indeed, there could be multiple sources of interference during EEG recording either internally (muscle contamination) or externally (ambient magnetic field), resulting in many artefacts. Several methods exist to deal with these artefacts, which will be investigated later. Several sources of noise can contaminate EEG signal:

- Electromagnetic perturbation (mobile phone, line power noise 50Hz/60Hz).

- Physiological perturbation: muscle signal or eyes blinks.

The primary sources of noise are the ones from electrooculogram (EOG) due to movement of eyes and their corresponding muscles, and electromyogram (EMG)

due to the activity of muscles of jaw or eyebrow. A first conventional step of preprocessing is to bandpass the brain signal to remove the lower (background fluctuation) and higher (muscle activity, line power) frequency in the signal. The signal could be down-sampled following the Nyquist criterion: sampling frequency is at least twice of the maximum frequency component of the signal. This down-sampling reduces the size of the signal, decreases the computational time of analysis, at the cost of lower the time resolution.

Then, it is important to ensure that the signal is free of artefacts as much as possible to get reliable analysis results. EOG is due to the movement of eyes or eye blinks, which produce big deflection visible across all channels, mainly in the frontal and temporal regions. To clean the signal from artefacts, it is either possible:

- To ask the subject to avoid strong movements or blinks, which is difficult in practice.

- To suppress the signal (or the trial) for the duration of the artefact (by a visual check or automatic rejection).

- To use algorithms which suppress the component of the artefactual source and reconstruct an EEG signal artefact-free.

The main method for the third case is the blind source separation (BSS) method implemented by Independent Component Analysis (ICA). The ICA reconstructs the data to have components statistically independent from each other. After applying this transformation, the component containing EOG signals is removed, and the original data are reconstructed from the remaining components. EMG artefacts are related to the muscles (like muscles of the face). EEG can contain

artefact in the frequency band of $20 - 200Hz$, due to the contraction of muscles (Goncharova et al. 2003). As the temporal and spectral natures of EMG overlap with EEG in the gamma band ($30 - 80Hz$ (Goncharova et al. 2003)), reliable methodologies should be implemented (Muthukumaraswamy 2013) to avoid misinterpretation of the results. ICA or ICA Spectral-Ratio (ICA-SR) (Ma et al. 2012) or other Blind Source Separation (BSS) methods are used to reduce the EMG artefact.

Scalp EEG are measurements of brain activity propagated over the scalp, the use of a spatial filter to remove the joint information collected by adjacent electrodes is advantageous, and Laplacian filters can be used to solve this issue (Muthukumaraswamy 2013), and to deal volume conduction issues. It will be beneficial for removing EOG/EMG when BSS is not able to isolate all the EOG/EMG activity.

We adopted appropriate data preprocessing technique on our data, which is described in each of the method section respectively.

2.6 Signal Analysis

The purpose of signal analysis is to extract useful patterns, and ultimately to be able to classify these patterns as belonging to a particular mental state. Features from EEG time-series data for fatigue detection can be extracted in different ways: time domain, frequency domain, and multivariate analysis.

2.6.1 ERP Studies

Event-Related Potential (ERP) is the measurement of brain response to a specific stimulus. It is applied by averaging short periods of signal (epochs) locked to a

stimulus (Luck 2005). ERPs define temporal characteristics of the brain during the first few seconds after stimulus' presentation to a subject. Different types of stimuli are used to study ERP. Based on auditory or visual paradigm, ERPs have been observed since the beginning of the 1960 and are still widely used today in research.

The field of ERP started with the discovery of the Contingent Negative Variation (CNV) by Walter (Walter et al. 1964). In his study, subjects were presented a warning signal followed one second later by a target stimulus. In mind wandering condition, each stimulus elicits a usual wave response that would be expected for these stimuli. However, if subjects were required to respond to the target, e.g. pressing a button, a substantial negative potential appeared during the period between the warning signal and the target. Then, this CNV is not just a sensory response but appears to reflect the subject's preparation of the goal response one has to execute.

Another major ERP component was discovered in the same period than the CNV. This is the P300 (P3). It is a component that appears under the effect of surprise and presents a large positive voltage which peaks around 300 ms post-stimulus. P3 is a wave occurring when a subject is asked to respond (mentally or physically) to a target. Targets can be infrequently presented as a single stimulus or be part of target discrimination among frequent standard stimuli. In a three-stimulus paradigm, as shown in Fig. 9, P300 can be decomposed in two sub-components: a first component with high amplitude and low latency, and the last component with low amplitude (compared to the early component) and high latency (Donchin 1981).

The first component called P3a is usually generated when the stimulus is a

distracter, i.e. neither the target nor standard stimuli; whereas the second component, P3b, is generated when the subject becomes aware of the target. Both components are somehow mixed and not always easily delineated. Theories suggest that P3a component relies on the attentional network, and the generators are mainly frontal. Its functional role is supposed to serve as an attentional filter, to inhibit neural processing of the wrong target by a top-down mechanism. The second component is proposed to relate on memory and context updating, whose generators are more in parietal cortex. Moreover, P300 generators are not accurately delineated, but a typical pathway between frontal and parietal/temporal brain areas is the most commonly accepted (Polich 2007).

A last essential ERP is the mismatch negativity (MMN), shown by Naatanen, Gaillard and Mantysalo (1978). The MMN is a negative component to any discriminable change ('deviant') in some repetitive stream of auditory stimulation ('standard'). This brain response can be elicited even in the absence of attention, which makes this component important for the study of cognition and consciousness. In this thesis, two different experimental paradigms are used to study ERP components. The first one is an oddball auditory paradigm and the second one is a motor related task.

Recently an experimental design gained interest by its possibility to embed different levels of irregularity. We used this paradigm to understand the brain state of sedation. Analysis were presented in Chap 5. This paradigm was devised by Bekinschtein et al. (2009) as shown in Fig. 10. It consists of a local irregularity build from five tones (a quintuple). The fifth can be similar (local standard) or different (local deviant) from the four previous ones. It is expected the local irregularity will elicit the MMN component. A global regularity is built-up with
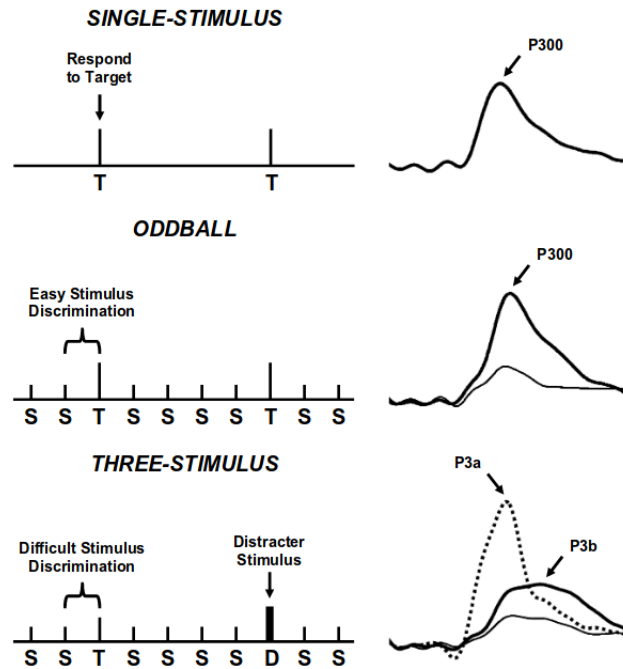
Figure 9: Oddball paradigms. Schematic illustration of the single-stimulus (top), oddball (middle), and three-stimulus (bottom) paradigm, with the elicit ERPs from the stimulus of each task at the right (Polich and Criado 2006). The single-stimulus task generates an infrequent target (T) but no other stimulus. The oddball task presents two specific stimuli in a random sequence, with one (target: T) occurring less frequently than the other (standard: S). The three-stimulus task add a compelling distractor (D) stimulus to the oddball task, that occurs irregularly. In those tasks, the subject is asked to respond only to the target but not to the other stimuli. In the three-stimulus case, the distractor elicits a P3a, and the target elicit a P3b.

the stream of the quintuples. From this stream of quintuples, 20% of the quintuples are globally deviant by changing the pitch of the fifth tone. Our hypothesis is the global irregularity will induce the P3 component. A combination of four conditions are created with these two factors, local and global, each comprising two levels, standard or deviant.

Notably, it was shown that the local effect is a spontaneous neural response and a short effect which is present also in vegetative patients. The global effect is

33
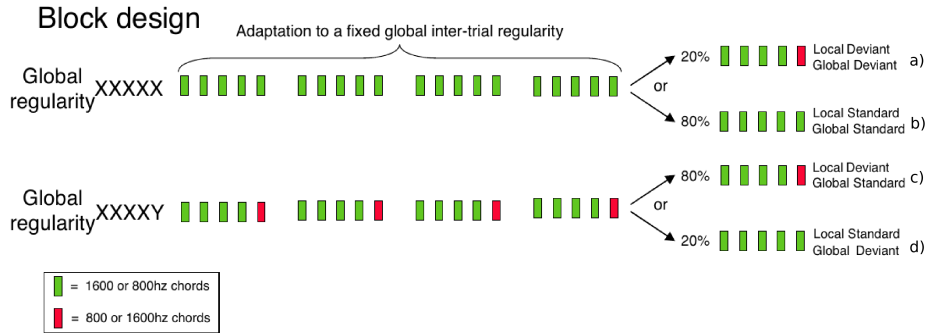
Figure 10: Experimental design for the local-global task. The local-global auditory task designed from (Bekinschtein et al. 2009) consist of five tones called quintuple whose last one is deviant or standard compared to the first tone. An higher block level from the stream of stimulus designs a global regularity. The block design presents the four conditions analysed in the experiment: (b) local standard / global standard (LSGS), (c) local deviant / global standard (LDGS), (d) local standard / global deviant (LSGD) and (a) local deviant / global deviant (LDGD). The adaptation period sets the global regularity of the session. The probability transition (20% and 80%) set up the two levels of irregularity.

related to conscious processing, occurs later and is longer active, requiring higher neural processing (Bekinschtein et al. 2009). Thus, looking at the MMN and P3 components for subjects in sedation and recovery would help us to gain in insight in consciousness.

Similar to Event Related Potential, there is also Muscle Related Cortical Potential (MRCP), which represent cortical activities time-lock to a muscle contraction event. More details are given in Chap 7.

2.6.2 Frequency Domain Analysis

Temporal information of the EEG raw data gives only one aspect of brain activity as the neuronal signal is a result of micro-cortical columns of neurons firing together at different rhythmic (oscillatory) activities. It is necessary to translate the time-series signal of EEG into a frequency domain, to extract the power of

the signal in specific frequency bands. EEG brain signal analysis takes advantage of the recent improvement in signal processing to extract time-frequency power. Five major frequency bands have been established: delta band $[0.5-4\ Hz]$, theta band $[4-7\ Hz]$, alpha band $[8-12\ Hz]$, beta band $[13-30\ Hz]$ and gamma band $[30-80\ Hz]$. The boundaries of the bands are not strictly established. They are also subject to fluctuations from individual to individual, and sometimes each of the established frequency band can be divided further into sub-bands (i.e. low alpha, high alpha) (Klimesch 1999). Nevertheless, each frequency band could be interpreted in light of a similar behaviour: delta band is present during sleep. Theta relates to memory retrieval and encoding; alpha is present during relaxed states or eyes closed and inhibited for attention. It is also the more predominant frequency band in human brain activity. Beta increases with arousal and alertness and gamma is related to higher level of cognitive processing. Other more specific bands or rhythmic activity are also defined (e.g. *mu* rhythm, related to muscular movement).

It has been found that theta power increased with a workload, related with the requirement of attentional resources, whereas alpha decreased during workload experiment (Gevins et al. 1998). Decreasing of alpha is known as a 'desynchronisation' effect (Niedermeyer and da Silva 2005). Moreover, by increasing the complexity of the task, the power in Theta is found to increase mainly in the frontal area. When a subject is carrying a mental fatigue task, one's level of arousal decreases and a shift of power in the lower frequency is reported (Klimesch 1999): theta activity increases in the frontal areas (Wascher et al. 2014) and alpha activity increases over the scalp. Gamma was reported to decrease as subject feels fatigue, in central and parietal areas for a driving fatigue study (Papadelis et al. 2007). Correlation between beta waves and mental fatigue is not consistent. In

some studies, one's activity increased in the frontal area as an attempt to stay in a level of vigilance. While in other studies, level of beta decreased with fatigue (Zhao et al. 2012). In a driving study, sleep-deprived subjects had their level of power in beta band decreasing over the whole scalp except in frontal lobe. This can be explained as their level of vigilance is reduced by sleep deprivation. In the delta band, no significant change is found with fatigue. We therefore performed such analysis on the fatigue dataset, as detailed in Chap 6.

2.6.3 Non-Linear Analysis

Complexity parameters can be used to assess the change in EEG signal, based on information theory and Shannon entropy (Shannon and Weaver 1949). Shannon entropy describes the uncertain in time-series data: a very predictive signal is poor in information and has low entropy. Also, with the work of Kolmogorov on information theory ('algorithmic information theory'), a Kolmogorov complexity (Kc) was proposed as a way to quantify the complexity of a signal. E.g. given two strings of ten symbols, the string *'99999999999'* can be reduced as *'ten9'*, whereas the random string *'Htd5l0Sc3r'* could not be more reduced: the latter case has the highest complexity. These works are the basis for numerous entropy developed recently and also characterised the rate of information in the times-series. As discussed in Dauwels, Vialatte and Cichocki (2010), Approximate Entropy (ApEn), Sample Entropy (SEn), and Tsallis Entropy (TE) are usually used as features in bio-physiological signals. ApEn reflects the probability of patterns in a signal not to be followed by some 'similar' patterns (Pincus 1991), and then a low value of ApEn reflects regularities in the signal. SEn, developed to overcome some statistical bias with ApEn, have been successfully applied to cardio-vascular

dataset (Richman and Moorman 2000). TE is a family of entropy characterised by a real number q and is equal to Shannon entropy for $q = 1$.

A study used ApEn, Kc, and TE features to analyse one-minute pre-task versus one minute post-task. TE did not give a significant change in these two conditions. ApEn and Kc were significant for all channels. More specifically, in beta band, ApEn and Kc decreased in the parietal area after performing fatigue induced task, while in alpha band, Kc feature shown significantly decreased for the whole scalp (Liu, Zhang and Zheng 2010a). In a driving experiment with sleep deprivation, ApEn did not present a significant change in any of EEG channels (Papadelis et al. 2007). However, Shannon Entropy decreased significantly between the first and last 15 minutes in all brain areas except for the frontal region. The Kullback-Leibler measure (measure of distance between two distributions) decreased significantly in the parietal and occipital regions (Papadelis et al. 2007). SE has been applied as a marker to detect brain change during mental fatigue (Tran et al. 2007).

Moreover, if EEG signal presents very irregular patterns that seem to occur randomly, underlying dynamical laws could appear. They describe the deterministic dynamical evolution of time-series. Such dynamical system can be described in a higher n-dimensional space, where 'strange' attractors (e.g. Lorentz attractors) characterise system's transition in stable states. In physiological systems, this decrease of complexity (stable states) is correlated with pathological states (Mackey and Glass 1977), like during epileptic seizure (Babloyantz and Destexhe 1986). Largest Lyapunov exponent, which reflects the rate of separation of closed trajectories in this phase state, is a measure used in chaos theory to quantify the complexity of the system (Pincus 1991). This measure has been related to error-prediction during monitoring task (Imanishi and Oyama-Higa 2006).

Although we did not used the non-linear analysis directly to measure brain activities, entropy-based measurement was used to do connectivity analysis, as described in the following section, as a way of phase synchrony quantification.

2.6.4 Connectivity Analysis

The methods mention in the previous sections focus on the analysis for each channel independently, but brain signal exhibits long-range connections between different brain areas (Varela et al. 2001). Methods need to be used to quantify these interactions among multiple channels. There are different approaches for connectivity analysis.

- Coherence-based Connectivity

- Mutual Information-based Connectivity

- Phase-based Connectivity

1) Coherence has been widely used in neuroscience analysis. With mental fatigue, coherence significantly increases (Lorist et al. 2009; Papadelis et al. 2007) compared to baseline. Coherence was found higher for subjects who recovered from disorder of consciousness (Schorr et al. 2016).

2) Cross-Approximate Entropy (C-ApEn), as mutual information-based connectivity, increased significantly in the parietal and central areas among pairs of electrode (Papadelis et al. 2007) concerning fatigue state. A return from consciousness was correlated with a rise of C-ApEn, after anaesthesia in (Hudetz et al. 2003).

3) However, previous methods, particularly coherence is not well adapted for EEG signal, as it takes into consideration a mixture of amplitude and phase of the

signals to observe. Phase analysis is more likely to give information of interactions between two channels, as proposed with the neural assembly hypothesis (Varela et al. 2001). Phase synchrony was investigated by Zhang et al. (2014) and shown a decrease of Phase Locking Value (PLV) related to fatigue in the beta band for central and parietal regions in an inter-hemispheric analysis. Similarly, the frontal area has shown a decrease in intra-hemispheric regions. PLV in the theta band increased in the frontal area in fatigue state Zhang et al. (2014).

We therefore performed analysis using entropy-based phase connectivity analysis in Chap 3. The previous connectivity measures can be extended to functional connectivity (see Bressler and Seth (2011) for a methodology review) and also be used for further graph theory analysis.

2.6.5   Source Reconstruction

Analysing the brain activity at the scalp level does not give information about the neural sources (dipoles) involved. To figure out what activity arise inside the brain at the source level, advanced mathematical techniques have been developed, and a high number of channels are necessary with at least 64 channels. Many inversion methods have been developed but all required a two step procedure. The first one is the 'forward model' to map the dipoles activity to the scalp activity. The most important step is the second one, called 'inverse model', to know the source level activity from the scalp activity. Two categories of inverse model exist. One is a model with few dipoles called 'Equivalent Current Dipoles', and the other a model with thousand of dipoles called 'imaging'. Different methods also have been developped for the imaging methods (Baillet and Garnero 1997), starting from the most popular which is minimum norm. The algorithm we use is Multiple Spare

Prior (MSP) (Friston et al. 2008). It avoids the broadness of the source activity found using the minimum norm method. We used these methods to find sources of activity during different states of consciousness in the local/global task with sedation, in Chap 4 and 5, and in the fatigue lift study, in Chap 7. We did not applied source reconstruction methods for coma and QBD study, as well as with the cycling study, due to the low number of channels.

2.7 Statistical Evaluation

2.7.1 Hypothesis Testing

Classical parametric statistical analysis are based on hypothesis testing. From two groups of population, one may want to know for example if one group is taller than the other, and make statistical tests to evaluate this assumption.

True State	Decision	
	Accept Null	Reject Null
Null is true	Correct	Type I error ($\alpha\ error$)
Null is false	Type II error ($\beta\ error$)	Correct

Table 1: Hypothesis testing.

From the table 1 the first column is the true state about the assumption. We call 'Null Hypothesis' or H_0 hypothesis the assumption that both populations have the same mean, or that the difference of mean between these two population is zero (Null). The second and third columns are the decision. The decision after the statistical testing can be either to accept the Null hypothesis or to reject the Null hypothesis. In case the Null hypothesis is accepted, and the true state is Null, this decision is correct. If the Null hypothesis is rejected after the test, but the true state is Null, this gives rise to a Type I error, also call α error. If both the

40

true state and the decision are against the Null hypothesis, it is correct. Finally, if the true state is against the Null hypothesis, but the decision accept the Null hypothesis, this is a Type II error, also call β error, as shown in Fig. 11.
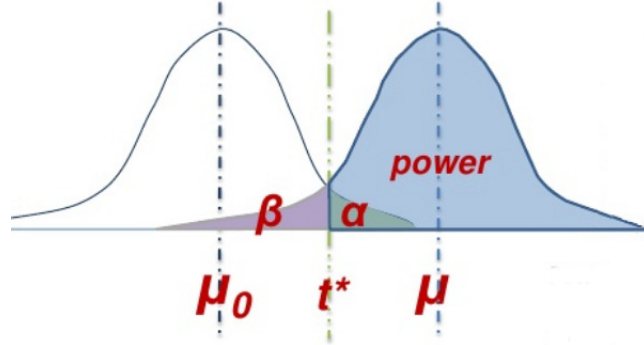
Figure 11: Significance testing.

Based on the hypothesis testing, the decision should be as accurate as possible (decision should reflect the true state) and minimising Type I error and Type II error. Under the assumption that the population follows a normal curve (central limit theorem), 95% of the curve are under 3 Standard Deviation (SD). On the 5% of outliers, they can be considered not belonging to the population. Therefore, an α level of 0.05 is usually accepted for the statistical analysis.

The t-test has been developed to test the distribution against a Null distribution. Then for a one sample t-test, the t-value between two distributions is:

$$t = \frac{\mu_1 - \mu_0}{\frac{\sigma_1}{\sqrt{N}}} \tag{1}$$

Were μ_1 the mean of the sample population and μ_0 the Hypothesis testing mean. The variance of the sample population is σ_1, and N is the sample size.

For a comparison between two different populations a two-sample is used, with

H_0 the Null hypothesis is: $\mu_1 = \mu_2$ to test the mean of the population are equal. If the same population is tested twice with a different factor, a repeated paired t-test need to be performed to measure the effect of the factor on the population.

2.7.2   ANOVA

The *t*-test statistical analysis is used for one *factor* with a maximum of two *levels*. It can be generalised with a ANOVA, analyse of variance, for more than one factor, each with two or more levels. ANOVA is an example of the General Linear Model (GLM). Consider an ANOVA with one factor A of three levels, each level measured on an independent group of e.g. 30 subjects. This can be expressed formally as the following GLM:

$$y_{s,a} = x_1\beta_1 + x_2\beta_2 + x_3\beta_3 + \epsilon_s, a \tag{2}$$

where $y_{s,a}$ stands for the data from the sth subject in the group who received the ath level of factor A, represented as a column vector (with $n = 1..90$ -3x30- values in this case); x_a is a *regressor*, an indicator variable whose values of 0 or 1 code whether the nth measurement in y comes from the ath level of A. The parameter β_a refers to the ath level of A whose values are estimated by fitting the model i.e. here correspond to the mean across subjects for that level; and finally $\epsilon_{s,a}$ is the residual error for the sth subject and a^{th} level. Fitting the model requires estimating the values of the three parameters such that the sum of the squares of the residuals errors is minimized (i.e. least square error). It can then be rewritten in matrix format as:

$$Y = X\beta + \epsilon \qquad where\ \epsilon \sim N(0, C_e),\ C_e = \sigma^2 I \tag{3}$$

and with X being the design matrix in which the three regressors have been combined. The ϵ terms shows that the residuals are assumed to be drawn from a zero-mean, multivariate normal distribution with covariance C_e, expressed as a N-by-N identity matrix scaled by a single variance term σ^2.

The model being fit, the main effect of factor A refers to the standard statistical test of the null hypothesis that the three means of each level are identical, i.e. that $\beta_1 = beta_2 = beta_3$. This is validated by establishing an F-statistic, which have several formulations. One of them is the mean sum of squares of the treatment effects: β_{1-3}, divided by the mean sum of squares of the residuals:

$$F(df_A, df_\epsilon) = \frac{SS_A/df_A}{SS_\epsilon/df_\epsilon} \tag{4}$$

where SS are the sum of squares and df are the degree of freedom. Given those df, the probability of obtaining at least that value of F under the null hypothesis, p, can be calculated from the standard F-distribution and declared significant if p is less than a certain value, e.g. $p < 0.05$. The F-statistic can also be expressed by a contrast matrix, $\mathbf{c}$, also called F-contrast.

When the same group is taken to test for example two factors, each with two levels, a within-subject design matrix is used. The resulting four conditions are measured on each of the 30 subjects, and one possible GLM for this repeated-measures 2x2 ANOVA is:

$$y_{s,a,b} = x_{11}\beta_{11} + x_{21}\beta_{21} + x_{12}\beta_{12} + x_{22}\beta_{22} + X_s\beta_s + \epsilon_{s,a,b} \tag{5}$$

where x_{11} indicates whether or not the nth measures comes from the first level of A and the first level of B. The matrix X_s has one column per subject and captures

the mean across conditions for each subject. Within this model, we can test three F-contrasts:

$$c_A = \begin{bmatrix} 1 & 1 & -1 & -1 \end{bmatrix}$$

$$c_B = \begin{bmatrix} 1 & -1 & 1 & -1 \end{bmatrix}$$

$$c_{AB} = \begin{bmatrix} 1 & -1 & -1 & 1 \end{bmatrix}$$

where c_A corresponds to the main effect of A (padded with 30 extra zeros for the subject effect), c_B is the main effect of B and c_{AB} stands for the interaction between level A and level B. This can be generalized to K-way ANOVAs, with K factors each with L_k levels (Henson 2015).

Interaction between effect A and effect B appears when the effect on one variable e.g. A is not the same depending of the level on the other variable e.g. B. If the first effect A is for example a local effect with two levels standard and deviant, and factor B a global effect with two levels standard and deviant, the interaction can be interpreted as shown in Fig. 12. Interaction is shown in Fig. 12a) between local effect and global effect. The global effect i.e. global deviant minus global standard interact with the level of the other factor i.e. local effect. In case of a local standard, the global effect is shown in the blue arrow on the left. The global effect for the local deviant is the represented by the blue arrow on the right. Local by global interaction is 'the difference of difference' i.e. global effect for local standard minus global effect for local deviant: (LSGD-LSGS) - (LDGD-LDGS). In Fig. 12a) the interaction shown by the difference between both blue arrows is important which favours a significant interaction. In Fig. 12b) the interaction shown by the difference between both blue arrows is close to zero, which explains an absence of interaction.

(a) Interaction between local and global effect

(b) No interaction between local and global effect
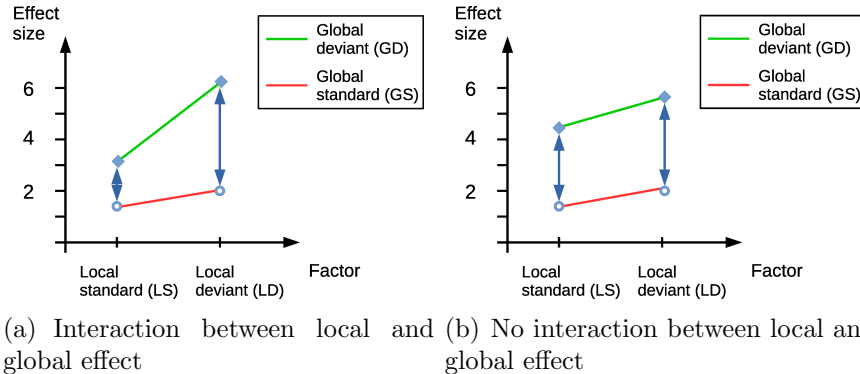
Figure 12: Interaction for a 2x2 experimental design. a) Interaction is the difference of difference: (LSGD-LSGS)-(LDGD-LDGS). It is important for a significant interaction, as shown by the difference between both arrows. b) Global effect is similar for both local standard and local deviant, which suggests an absence of interaction.

It should be notice that a three way interaction is the interaction with a third factor. For the local and global factor, a third factor e.g. of sedation can be explored. Then, the difference of interaction between Figs. 12a) and b) represents the three way interaction.

2.7.3 Controlling for Family-Wise Error Rate

When making inferences about a statistical test with neuro-imaging dataset, we are dealing with multivariate analysis. For k features extracted from EEG, with c channels, there can be several hundreds of hypothesis testing to be applied. In case of brain analysis, the hypothesis testing applies for each voxel i.e. several thousands of different tests. This brings a massive *multiple comparisons issue*, with an error rate being important due to the false positive. For a α level of 0.05, one statistical test other 20 may be positive by chance where it should not be. This Type I error is also known as the Family Wise Error Rate (FWER).

One method to counteract this multiple comparisons issue is the *Bonferroni*

correction[1], which compensates the number of m testing by reducing the significance level to α/m, where α is the overall alpha level, and m the number of hypothesis (Nichols and Hayasaka 2003). For example, if an analysis is testing $m = 20$ different channels with a desired $\alpha = 0.05$, then the Bonferroni correction would test each individual hypothesis at $\alpha_i = 0.05/20 = 0.0025$. However, Bonferroni correction is very conservative and should be used when the different hypothesis testing are independent from each other. In the case of neuro-imaging dataset, there are correlation underlying the features to test for, and the Bonferroni correction would be too strict. Then, it is not the most appropriate method to avoid properly the multiple comparison.

In the following chapters for EEG surface analysis, we developed non-parametric test to deal with this issue (Nichols and Holmes 2002). For analysis at the source level, statistical maps of the brain are involved and the SPM12 toolbox is used (Friston 2007). The theory behind FWER for brain imaging rely on Random Field Theory. The assumptions implicit in this approach are that 1) the SPMs are reasonable lattice representations of underlying continuous fields, 2) the components of the fields have a multivariate Gaussian distribution and 3) the height thresholds are high enough. These assumption are reasonable for neuro-imaging dataset, as long as the voxel-size or bin-size is small relative to the smoothness. This leads to topological inference, with three different topological features:

- Peak height, (Fig. 13a), analysis looks at the amplitude or intensity of statistical values to make statistical inference. This gives the best spatial specificity compared to cluster and set level.

- Cluster extent, (Fig. 13b), analysis refers to the extent of clusters across

---

[1]Named after the mathematician Carlo Emilio Bonferroni (1892 - 1960).

space to make statistical inference. It has a better sensitivity but worse spatial specificity compared to peak level analysis.

- Number of cluster, (Fig. 13c), analysis looks at the whole search region and evaluates the number of active clusters. It has the worst spatial specificity.

More particularly, it is possible to construct an expression for the probability of getting c, or more, clusters of volume k, or more, above a threshold u, as:

$$P(u, k, c) = 1 - \sum_{i=0}^{c-1} \lambda(i, \Psi_0 p(n \geq k)) \tag{6}$$

which can be expressed as: consider clusters as 'rare events' that occur in a volume according to the Poisson distribution with expectation Ψ_0. The proportion of rare events that meet the spatial extent criterion will be $p(n \geq k)$. These criterion events will themselves occur according to a Poisson distribution with expectation $\Psi_0 \, p(n \geq k)$. The probability that the number of events will be c or more is finally one minus the probability that the number of events lies between 0 and c minus one.

The peak level analysis provides a critical value for the maximum height of a peak, while the cluster-extent topological inference defines a critical value for the maximum size of a cluster, or blob, in terms of voxels which compose it (M Kilner, J Kiebel and Friston 2005).

We used FWE correction in our analysis for the source localisation in chapter 5, to deal with multiple comparison due to the high number of voxels after source reconstruction.
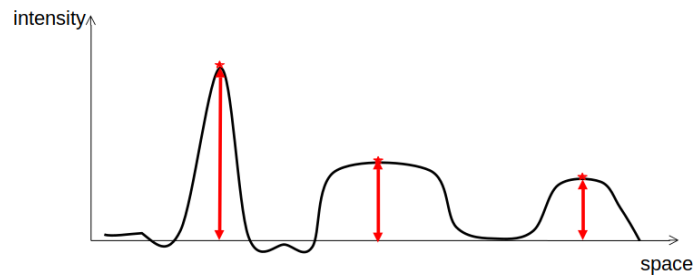
(a) Peak level
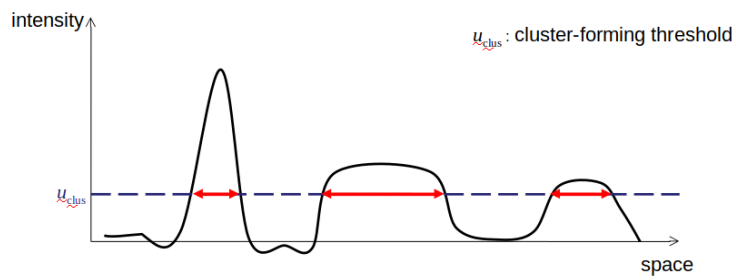
(b) Cluster level
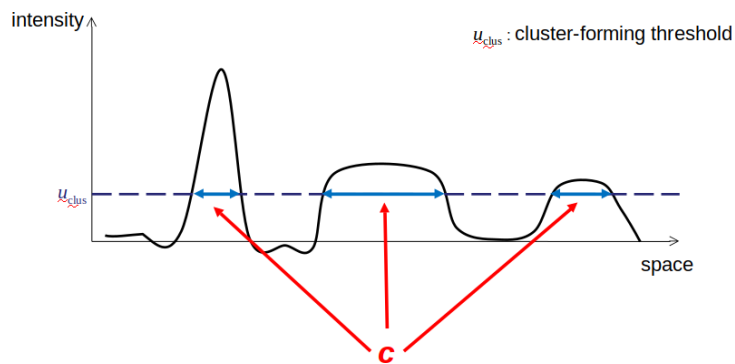
(c) Set level

Figure 13: Topological inferences implemented in SPM12, based on Random Field Theory. Three topological inferences are possible: a) peak level, b) cluster level, C) Set level. For b) and c) a cluster forming threshold is set up to define voxels that survive this cluster. A second level is used to select the cluster threshold level (b) or the set level (c).

Chapter 3

Phase Synchrony Analysis Between Coma and QBD

3.1   Chapter Outline

In this chapter, we applied connectivity measures on a clinical dataset. Using a group of patients in coma and quasi-brain death condition, we looked for EEG patterns that can distinguish between these two impaired states. We first describe the method of phase synchrony analysis, which has been applied to the scalp EEG. Then a non-parametric statistical measures were used to assess the differences between the two brain states (Li et al. 2014). Within-frequency phase synchrony analysis, as well as cross-frequency phase synchrony analysis were used. Statistical analysis were applied to assess the robustness of phase synchrony measure. We conclude by showing the potential of this measurement for cognitive and clinical assessment.

3.2 Introduction

Connectivity analysis for EEG data is very useful to identify brain's networks. As shown in the previous chapter, it examines interactions between different brain regions (either at the scalp level or source level) rather than only analysing which brain region are active. Therefore, we conducted the analysis of EEG data to be able to implement such analysis using phase synchrony algorithm. We make the following hypothesis: if the phase difference between two signals remains constant over time, the entropy would be null, indicating perfect synchrony as the signals from the two electrodes are activated in a close relation to each other. Hence, a strong connectivity between the underlying two signals. If the phase difference has a higher entropy due to strong fluctuation over time, it indicates lower synchrony of EEG channels. In this case the connection between two signals is weak.

As shown previously, different cognitive states can be quantified from brain activity measured via scalp EEG. We described in this chapter by identifying brain activity patterns of coma and QBD state. Indeed, a coma state can progress in QBD, and medical doctors need to regularly monitor the evolution of coma patients' brain states. Patients at the Intensive Care Unit (ICU) may have to face different levels of Disorders of Consciousness (DoC). It is a great challenge to understand the different aspects of DoC. Finding reliable neuro-markers from EEG recordings for distinguishing brain states is a very promising area of research. Studies have been done to understand the states of consciousness in pathological subjects, with a focus on understanding the emergence of brain states transit from complete unawareness (i.e. coma), towards the Unresponsive Wakefulness Syndrome (UWS), proposed by Laureys et al. (2010). The UWS starts from a lower boundary with coma patients who begin to show sleep-awake cycles but still

have the clinical signs of unresponsiveness. One step upward in UWS is the Minimally Conscious State (MCS). The upper boundary of MCS is: Severe Disorders of Consciousness (SDC). The lower boundary towards unawareness (from coma to brain death) still requires understanding. A recent publication distinguished between vegetative and minimally conscious states using phase-based analysis on resting-state EEG is proposed in Lehembre et al. (2012). Reviews in consciousness studies using connectivity analysis in pathological patients can also be found in Boly et al. (2012). It is challenging to have an accurate understanding of the state of unawareness below the deep coma to provide a precise diagnosis before brain death. From a legal point of view, brain death is defined as an irreversible loss of brain-stem and fore-brain function. The clinical diagnosis process of brain death varies from country to country, but they all involved an important number of tests to make a diagnosis.

For a patient in a deep coma to be diagnosed as QBD, pupil and brainstem reflexes test are applied before further examination of EEG. If a patient failed the tests, the medical doctor has the authority to decide, in regard to the EEG, if further tests should be done to evaluate brain death or if the medical care can be sustained. A patient is regarded as quasi-brain-death (QBD) if he failed brainstem reflexes tests, as shown in Fig. 14. A robust neuro-marker would help this process as a pre-diagnosis tool to help doctors to confirm their diagnosis of QBD. We aim to develop algorithm procedures for these clinical evaluations. In particular, it would give pre-diagnosis tool related to the EEG wave, for the decision-making process, before either medical care or apnea test and further monitoring.
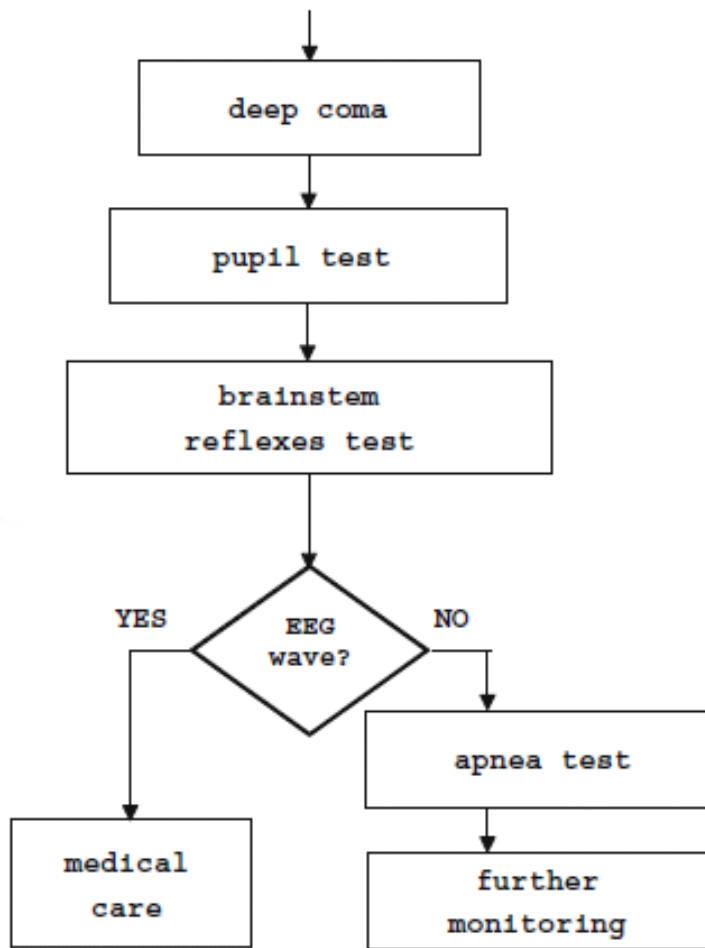
Figure 14: Diagnosis procedure to distinguish between coma and QBD state (Cao and Chen 2008). A patient in deep coma state has to pass through several medical tests, from pupil test, brainstem reflexes test, up to EEG evaluation. An algorithm to evaluate brain waves would provide an evaluation to assist the medical staff for diagnosis.

3.3 Clinical Dataset

The dataset used to distinguish between coma and QBD were recorded from 34 patients (18 males and 16 females) of ages ranging from 17 to 85 years old. They have been recorded at the ICU in HuaShan Hospital, Shanghai, China[1]. The EEG acquisition device was a portable NEUROSCAN ESI system. As patients were lying on the back with their heads up, EEG electrodes were attached to the scalp on the frontal part of the head. Nine electrodes were used for recording. Among them, two electrodes were positioned on the ears (left and right) as references (A1, A2). Other electrodes (Fp1, Fp2, F3, F4, F7, F8, Cz) were used for data acquisition, with Cz being the ground electrode, as shown in Fig. 15.
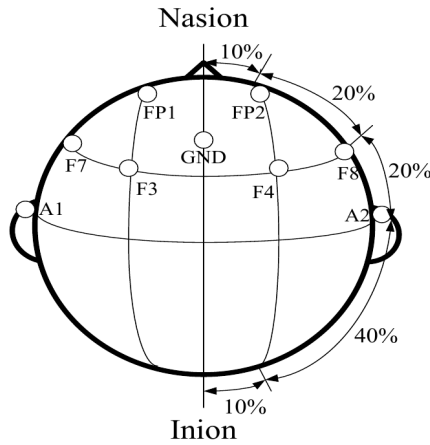
Figure 15: Electrodes placement for EEG recording in coma and QBD patients.

The corresponding channel numbers for the electrodes were: Fp1 - channel 1, Fp2 - channel 2, F3 - channel 3, F4 - channel 4, F7 - channel 5, F8 - channel 6. The sampling rate of the recordings was set to 1000 Hz, the mean recording time is 13 min per subject.

---

[1]These data were provided by Prof. Jianting Cao, Brain Science Institute, RIKEN, Japan

3.4 Phase Synchrony Estimation of EEG - The Method

We used phase synchrony analysis to evaluate the relationship between pairs of channels. The proposed method uses two successive steps to obtain phase synchrony between pairs of electrodes. First, for each channel of the EEG recording, phase features were extracted. The second step is to calculate a Phase Synchrony Index (PSI) between each pair of electrodes. Algorithms for estimating the phase synchrony feature are described in detail in this section.

3.4.1 Phase Estimation for Each Channel of Data

Phase estimation was proposed in (Lachaux et al. 1999; Varela et al. 2001; Tass et al. 1998). The aim is to differentiate the temporal signal $x(t)$ to a complex one, which carries both amplitude and phase information as: $a(t)e^{(j2\pi f(t)+\theta(t))}$, where $a(t)$ carries the envelope of the signal, and the phase is retrieved by $\theta(t)$. In our study, we used the established method in Lachaux et al. (1999). This method does not require computation in the complex domain and is suitable for real-time analysis as the complexity of computation is low. The process is:

Step 1: Apply band pass filter to the data, the frequency band is a frequency of interest (eg. alpha).

Step 2: Extract the local maxima M_i as an index vector. These are the peak of a cycle and this is done for each of the band passed data using first derivative.

Step 3: For each local maxima, or peak, compare the time shift from a peak of perfect sinusoidal signal at the same frequency of interest.

Step 4: The phase is obtained from the time shift between observed and ideal

maxima.

Step 5: Construct a signal of phase changes over time.

This measure is interesting for a signal with low noise in the frequency of interest. In our analysis, we focussed on signals at different frequency bands. A Finite Response Filter with order 100 (101 samples of data) was used to perform filtering. A frequency band range of 0.5-4 Hz was used for delta, 4-6 Hz for theta, 8-12 Hz for alpha, 18-22 Hz for beta and 28-32 Hz for gamma. Next, we computed the relative phase compared to an ideal sinusoidal signal at the frequency of interest (middle of the frequency band). The phase information was then estimated by:

$$\theta = (N \ mod \ \frac{F_e}{F_f}) \times \frac{F_f}{F_e} \times 2\pi, \tag{7}$$

where mod is the modulus operator, F_e and F_f are respectively the sampling frequency of the signal and the frequency of interest (i.e. 10 Hz for alpha waves); $\frac{F_e}{F_f}$ is the number of samples for one cycle, and N is the number of samples corresponding to the local maximum. After the relative phase was computed for each local maxima, the phase of the signal along the time is then reconstructed.

3.4.2 Quantifying Phase Synchrony via Phase Synchrony Index

Different terms are used to define phase relationships, i.e. "in phase", "out of phase", "phase locking". We followed "phase locking" defined in Varela et al. (2001) for phase synchrony estimation, measuring phase locking instead of phase-amplitude coupling. That is, for signals $s_1(t)$, $s_2(t)$, and their corresponding

phases $\theta_1(t)$, $\theta_2(t)$,

$$\theta_{12}(t) = |n\theta_1(t) - m\theta_2(t)| \tag{8}$$

where n, m are integers indicating the ratios of possible frequency. We focussed on the case $n = m = 1$ for within frequency analysis and $n \neq m \neq 1$ for between frequency analysis. If $\theta_{12}(t)$ is a constant, it means that the events detected by two individual electrodes are phase locked, therefore indicating there is a strong relationship between two channels of the EEG signals.

Having obtained phase information from the data, phase synchrony was quantified by an entropy-based method as described below. The phase difference between the two observed signals is given by $\theta_{ij}(t)$, for the electrodes i and j. In order to statistically quantify the phase synchrony, an index is used to indicate the degree of phase synchrony, i.e. the PSI. It can be quantified using Shannon entropy by the phase coherence value (PCV) (Tass et al. 1998; Looney et al. 2009; Li et al. 2012):

$$\rho_{ij}(t) = \frac{E_{max} - E}{E_{max}} \tag{9}$$

where $E = -\sum_{n=1}^{N} p_n \ln p_n$, Shannon's entropy of $\theta_{ij}(t)$, is calculated using time window $(t : t + W)$, with W being the window length. N is the number of phase bins, whereas p_n is the probability of θ_{ij} being obtained within time window $(t : t+W)$. The best suitable number of bins N is calculated from $N = \exp(0.626 + 0.4 \ln(W - 1))$, and $E_{max} = ln(N)$. In this way, phase synchrony varies between 0 and 1, with 1 being perfect synchrony, and 0 being anti-phase.

The effectiveness of this method for phase synchrony extraction is demonstrated using two synthetic signals in section 3.5.1. Then analysis results on data from 34 patients are presented from section 3.5.2. The level of synchrony among pairs of electrodes recorded from EEG signals are shown in matrices for coma and quasi-brain-death subjects respectively. Statistical analysis was also performed to evaluate the effect.

3.5 Within-Frequency Phase Synchrony Analysis

First, we conducted within-frequency phase synchrony analysis, which means setting $n = m = 1$, in Eq. 8. An analysis was applied to synthetic data, where we quantified the relationship between the two signals using PSI. Then, these analyses were applied to clinical dataset to see if PSI can be used as a feature to distinguish between coma and QBD patients.

3.5.1 Phase Synchrony Analysis on Synthetic Signals

The phase synchrony approach was first demonstrated using two synthetic signals, as shown in Fig. 16, where the top panel shows two signals. Signal $S1 = sin(wt)$, shown in dotted red line, is a sinewave of 2 seconds, with a frequency of $F = 2\pi/w = 10Hz$. Signal $S2$, shown in solid blue line, is plotted using $S2 = sin(wt + \phi(t))$ with the same frequency but $\phi(t)$ being $\pi/3$ for the first second. After that, the phase for $S2$ changed randomly. Phase synchrony for each time point was calculated using a sliding window of 0.1 second. As shown in the bottom panel of Fig. 16, phase synchrony index is 1 for the first second, indicating perfect
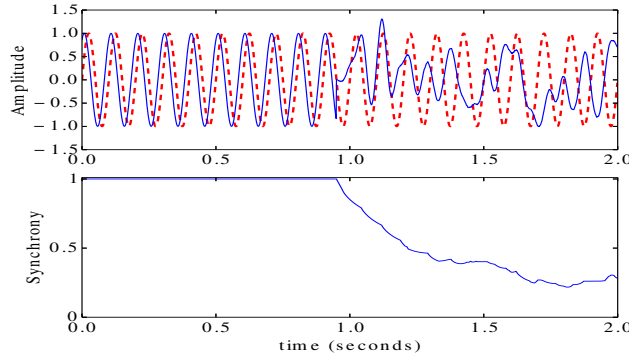
Figure 16: Phase synchrony analysis on synthetic signals. Top panel: $S1$ (dotted red line) phase changes with time compared to $S2$ (blue solid line), bottom panel: phase synchrony index computed between $S1$ and $S2$.

synchrony/phase locking of $S1$ and $S2$. From first second onward, $S1$ and $S2$ are out of phase, shown in the figure as reduced synchrony. As expected, there is higher synchrony when the two signals are phase-locked, but reduced synchrony when phase of one signal shifts away from the other. We can notice a slow decay of synchrony as we used a sliding window. Further analysis would be required to study signal to noise ratio.

3.5.2 Within-Frequency Phase Synchrony on Clinical Data

The Phase Synchrony Index (PSI) described in the previous section, was estimated for each pair of electrodes (15 combinations), with a window of 1 second ($W = 1000$) and a step between each window of 5 seconds for within-frequency analysis ($m = n = 1$ in Eq. 8). For each pair of electrodes, we obtained a PSI for each non-overlapping window. Then we calculated the mean by averaging PSI across all windows. The mean is shown in Fig. 17 with blue for lower synchrony, and red for higher synchrony. The maximum synchrony detected is below 0.6, so the colour scale is between 0 and 0.6. The matrices are plotted in two columns and five

rows. The first column shows the matrices of mean phase synchrony for all pairs of electrodes across all coma patients. The second column shows the matrices for all QBD patients. The matrices in each row indicate the phase synchrony for each frequency band (from top to bottom: delta, theta, alpha, beta, gamma). Each element in a matrix represents the PSI between a pair of electrodes. For each matrix, the diagonal from the bottom left corner to the upper right corner indicates the relationship to itself; thus the synchrony (PSI) for all diagonal elements are 1 (perfect synchrony). Each non-diagonal element in a matrix indicates the PSI between two different electrodes. For example, the top left corner element in a matrix indicates the PSI between row 1 (channel 1) and column 1 (channel 6).

The results are interpreted by the physical meaning of phase synchrony locking: in chaos theory, the process of phase locking occurs whenever the chaotic actions of the individual shift to the ordered actions of a collective system (Peat and briggs 1990). This gives a fundamental background to why phase synchrony is important for understanding neuron integration, especially why it is particularly useful for the identification of coma and quasi-brain-death. Coma patients have the ability to shift individual chaotic actions to the ordered actions of a collective system. The "chaotic to ordered" process is reflected by phase synchrony, whereas brain death patients do not have the ability to perform brain functions. Therefore, phase synchrony for coma patients should be higher than that of QBD. The analysis results suggest the mean PSI for coma data, as shown in the matrices, is higher than in QBD.

(a) Delta matrix - Coma   (b) Delta matrix - QBD

(c) Theta matrix - Coma   (d) Theta matrix - QBD

(e) Alpha matrix - Coma   (f) Alpha matrix - QBD

(g) Beta matrix - Coma   (h) Beta matrix - QBD

(i) Gamma matrix - Coma   (j) Gamma matrix - QBD
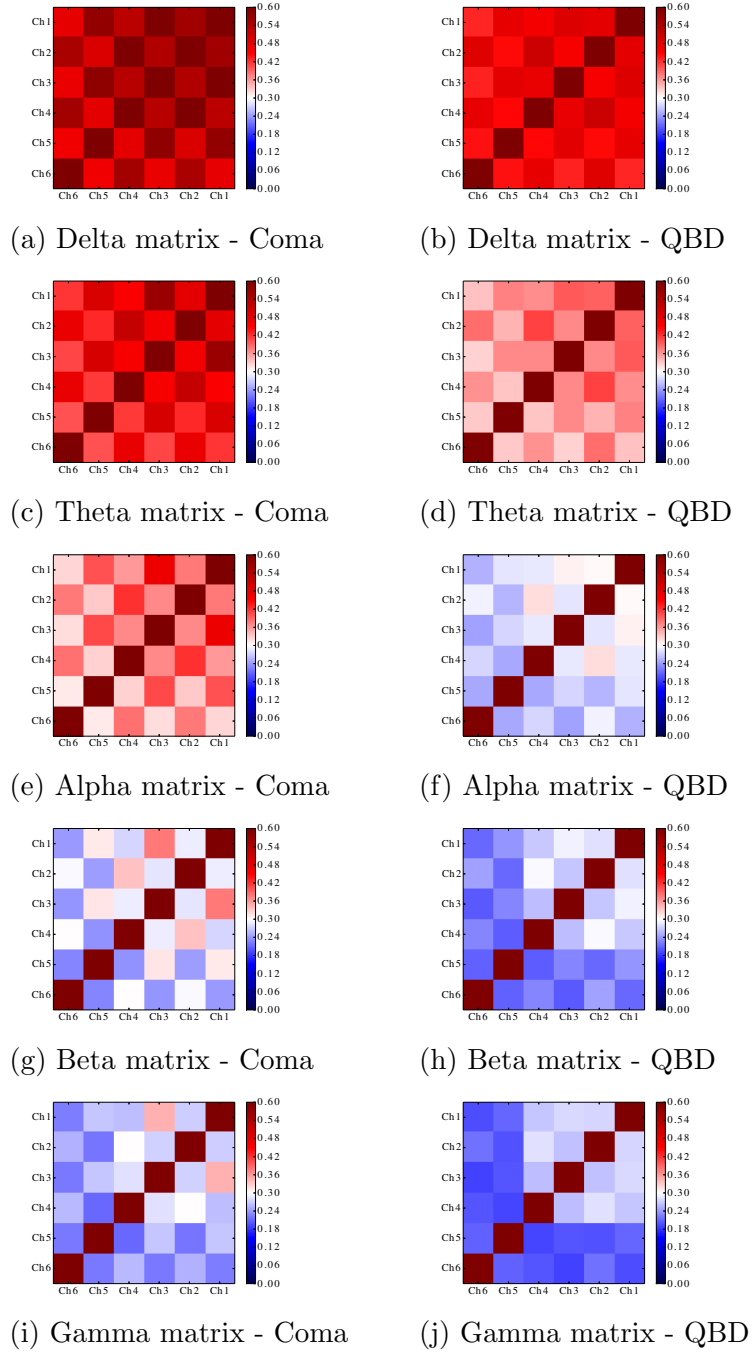
Figure 17: Phase Synchrony Matrix: Coma vs QBD, averaged from all the subjects. The matrices show the phase synchrony index between pairs of channels for the frequency bands, respectively a,b) delta, c,d) theta, e,f) alpha, g,h) beta and i,j) gamma. The first column presents the PSI for coma state and the second column the PSI for QBD state. Each matrix has six by six dimension, to represent the PSI for each pair of electrodes, from channel 1 to channel 6. These matrices are symmetric, with no PSI in the diagonal.

3.5.3 Statistical Analysis

Once PSI was computed for all the windows of recording, the mean PSI was calculated for each subject to be compared between the two groups: coma and QBD group. There were 17 subjects in each group, and the H_0 hypothesis was used to test whether these two groups have a statistically different mean. In this section, we first used a two-sample t-test to evaluate the results, and then performed a further permutation test to solve multiple comparisons problem.

The H_0 hypothesis is that they are similar, and statistical methods were used to test if this hypothesis has to be rejected in favour of its alternative (the two groups are significantly different) or not (the two groups are not significantly different). To further investigate the effectiveness of the phase synchrony feature, we performed a statistical test (two-sample independent t-test) to compare the PSI between coma and QBD for each of the 15 pairs of channels: $Ch1 - Ch2, ..., Ch1 - Ch6, ..., Ch5 - Ch6$ available in each frequency band. The significance threshold set to reject null hypothesis was 0.05. One limitation here is due to multiple comparisons. Indeed, the H_0 hypothesis rejection, i.e. when the two sets are statistically different, has a significant level of 5%. Considering this hypothesis, for twenty trials, we could have one false positive.

Thus, Bonferroni correction was performed to correct from multiple comparisons (Nichols and Hayasaka 2003). We divided the p-values with the number of statistical comparisons of 15 pairs of connections as we are looking for each frequency band individually , and the significance threshold was corrected to 0.0033. Results demonstrate all electrode pairs at alpha or theta bands are significant after correction, whereas only nine electrode pairs are significant in the delta band. Beta band sees nine pairs of electrodes significant. For gamma band, only one

electrode pair is significant. The analysis is done by comparing the p-value for a 2-sample independent t-test with 0.0033. All electrode pairs in theta or alpha bands had p-values smaller than 0.0033 indicate the coma patients' phase synchrony are stronger in Theta or Alpha band than that in QBD.

We also performed a non-parametric permutation test with no assumptions on the distribution of the PSI. In theory, the multinomial coefficient states that there are $2.3336 \times 10^9 = 34!/(17! \times 17!)$ possible permutations. Empirically, 1,000 iterations are regarded as sufficient to build a high-signal-to-noise-ratio distribution, but we performed 10,000 iterations for our analysis to achieve robust results. The statistical test results suggest all electrode pairs are significant after correcting multiple comparison (p-value<0.0033) in the theta or alpha band, whereas only 10 pairs in the delta band, 2 pairs in the beta band, and 1 pair in the gamma band were observed to be significant, as shown in Fig 18.

However, this correction is too conservative because this postulates that the signals measured from different pairs of electrodes are independent from each other, whereas we are not able to conclude on their independence as different brain regions tend to communicate with each other. We therefore proposed to use the maximum statistic, based on randomization test (Manly 2007). With this method, the t-value of two sample independent t-test between the two groups was compared with a distribution of maximum t-value. We consider the distribution from the maximum t-value for multiple channels comparisons within a frequency. For each of the frequency band, the algorithm to do the maximum distribution is as follows:

a) Shuffle the PSI matrices of the two groups to obtain a randomize and virtual group of coma and QBD PSI matrices.

b) Compute the t-value for each pair of electrodes with a two-sample t-test.
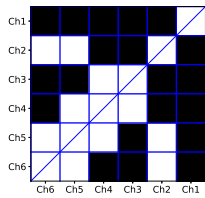
(a) Delta connectivity (b) Theta connectivity (c) Alpha connectivity
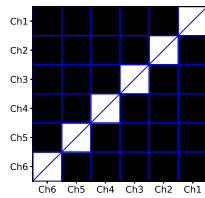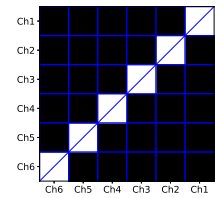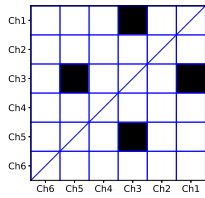
(d) Beta connectivity (e) Gamma connectivity
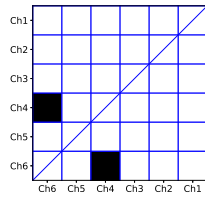
Figure 18: Connectivity Matrices: Coma vs QBD. The matrices show the connectivity of significant pairs of channels for the frequency bands, respectively a) delta, b) theta, c) alpha, d) beta and e) gamma. Significant pairs of channels after permutation are represented in black. Each matrix has six by six dimension, to represent each pair of electrodes, from channel 1 to channel 6. These matrices are symmetric, with no connectivity in the diagonal.

c) Take the maximum of t-value among the 15 pairs of electrodes.

d) The above steps are repeated several times. In this case, it was repeated 100000 times, to create the distribution using the t-values obtained in c).

e) The original t-value is compared to this distribution to evaluate the final p-value. To obtain the significance level, the ratio of values in the distribution above the original t-value compared to the 100000 number of values in the distribution was used.

Frequency Bands	Delta	Theta	Alpha	Beta	Gamma-L	Gamma-H
Frequency Used (Hz)	0.5-4.5	3-7	8-12	18-22	28-32	38-42
Max. Stat. p-value	0.1526	0.003	0.0026	0.5783	0.868	0.931
Original t-value	1.852	3.466	3.656	0.609	-0.142	-0.351

Table 2: Statistical Results Within-Frequency. The first row indicates the names of the frequency bands included for the analysis, for the frequency range shown in the second row. The third row presents the maximum statistic p-value for each frequency band. The p-values below the alpha threshold level are highlight in magenta. The last row shows the original t-value for each frequency band used to derive the maximum statistic p-value.

Table 2 shows the maximum statistic with permutation test, following the description above, for each frequency band. The frequency band are described in the first row, and the frequency range used is shown in the second row (i.e. for the alpha band, the frequency is from $8Hz$ to $12Hz$), the p-value after maximum statistic is given on the third row. The significant bands for an alpha level of 0.05 have their cells filled in magenta. The last row is the original t-value, obtained by an independent two-sample t-test performed for each pair of electrodes between the coma and QBD groups. After maximum statistic, theta and alpha bands discriminate between the two conditions.

3.6 Cross-Frequency Coupling Analysis

Our interest in this section was to observe the phase of two EEG signals at different frequency bands, known as cross-frequency coupling (CFC). What was shown for the within-frequency synchrony apply also in cross-frequency with $n \neq m \neq 1$ phase locking. Recent studies propose that communication in the brain could be possible by a mechanism of coupling across different frequency bands in healthy human (Canolty and Knight 2010; Canolty et al. 2006) or in pathological patients (Allen et al. 2011). We have shown in the previous section that two phases can be compared by the phase difference for the electrodes i and j, $\phi_{ij}(t)$. For signals $s_1(t)$, $s_2(t)$ filtered at frequency bands respectively $F1$ and $F2$ with their corresponding phases $\phi_1(t)$, $\phi_2(t)$, phase locking is then:

$$\phi_{12}(t) = |n\phi_1(t) - m\phi_2(t)| \tag{10}$$

where n, m are integers indicating the ratios of possible frequency locking. Within frequency phase synchrony differences were obtained by setting $n : m = 1 : 1$. To examine the phase difference e.g. within alpha band, then $F1 = F2 = 10Hz$ the $n : m = 10Hz : 10Hz = 1 : 1$. And the phase difference is: $\phi_{12}(t) = |\phi_1(t) - \phi_2(t)|$. Given $F1$ and $F2$ the filtered frequency of $s_1(t)$ and $s_2(t)$; for example $10Hz$ and $20Hz$, then $n : m = F2 : F1 = 20Hz : 10Hz = 2 : 1$. Then, ϕ_1 should be scaled to $n = 2$. The phase range before scaling is $[0 : 2\pi]$ and after scaling by 2 is $[0 : 4\pi]$. The modulus of 2π is required to get the phase in the same range than $\phi_2 : [0 : 2\pi]$. ϕ_2 remains identical as $m = 1$. Finally the two signals could be compared, having their phase in the same scale.

We performed analysis on the 17 subjects on coma and 17 subjects on QBD

for cross-frequency phase synchrony (n:m phase locking). We computed the phase synchrony between one frequency band over a second frequency band. Windows of data have a length of one second with a step between each window of 5 seconds. After band-pass filter in specific frequencies, we extracted PSI between pairs of electrodes. Then we computed the mean of PSI for all windows for each subject. Furthermore, statistical analysis was carried out to evaluate the effectiveness of phase synchrony features by the maximum statistic method.

For cross-frequency coupling, we first present the different matrices of synchrony among the cross-frequency bands, then look at these matrices the ones significant. Gamma band is divided in two sub-bands, gammaL (28-32 Hz, low gamma) and gammaH (38-42 Hz, high gamma). Because gammaH was not found significant with any other bands (see table 3), only cross frequency analysis with gammaL is shown in the synchrony matrices. The figures below present the cross-frequency phase synchrony between two different frequency bands. The matrices in each group of patients (coma and QBD) for the cross-frequency synchrony in the delta band is plotted in Fig. 19. This figure shows the phase synchrony with two rows and four columns for the delta frequency and the higher frequency bands. The first row is for coma state and the second row is for QBD state. Each column is the phase synchrony of the delta band with another frequency bands, from left to right respectively, a) theta, b) alpha, c) beta and d) gammaL (low gamma). The highest synchrony is 0.6, with red colour for high synchrony, and the blue colour is for lower synchrony. In cross-frequency coupling, the diagonal elements are not equals to one, as it highlights the synchrony in different frequency bands for the same channel. We see that delta/theta and delta/alpha have a higher PSI, compared to delta/beta and delta/gamma. Fig. 20 shows the phase synchrony matrices of cross-frequency coupling between coma (first row) and QBD (second

66

(a) Delta/Theta   (b) Delta/Alpha   (c) Delta/Beta   (d) Delta/GammaL
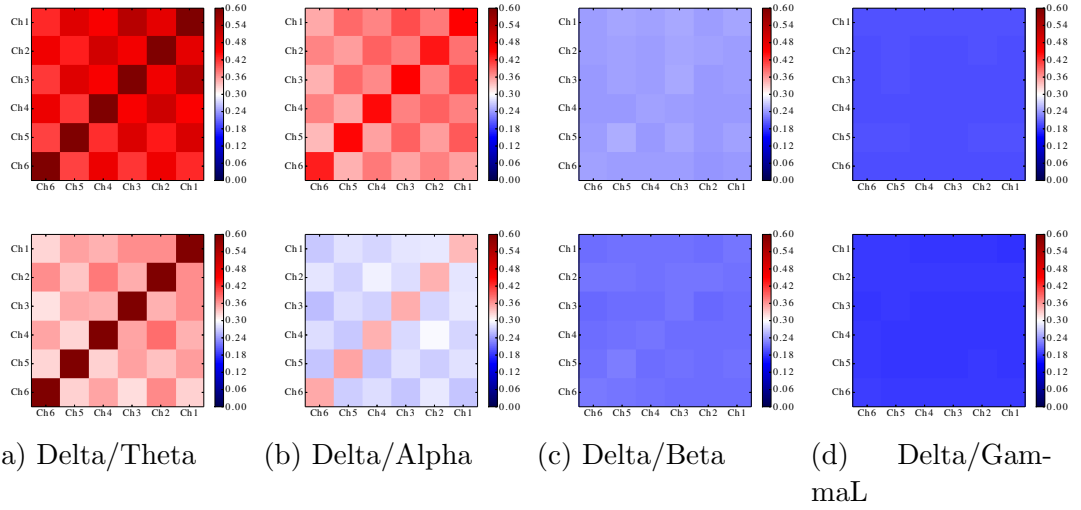
Figure 19: Cross-frequency coupling with delta - Coma (Up) vs QBD (Down). The matrices of phase synchrony index show the cross-frequency coupling for delta with respectively a) theta, b) alpha, c) beta, and d) gammaL. The first row of matrices is related to the coma state, and the second row is related to the QBD state. Each matrix has six by six dimension, to represent the PSI for each pair of electrodes, from Ch1 to Ch6.

row) for the theta frequency versus higher bands, from left to right respectively: a) alpha, b) beta and c) gammaL. For the theta cross-frequency coupling, we see that theta/alpha has the highest PSI. Fig. 21 presents the phase synchrony matrices of cross-frequency coupling between coma (first row) and QBD (second row), for the frequency alpha versus beta in the first column and gammaL in the second column.

We then applied maximum statistic analysis to know statistically which cross-frequency band is significant to differentiate between the two brain states. Table 3 presents the statistical results for each cross-frequency analysis. The lower-left part of the table is the t-value observed after a two-sample t-test statistic in the related cross-frequency band: for each pair of electrodes, a two-sample t-test is applied between the coma and QBD group, and the lowest is chosen for the table. In the upper-right part of the table are the p-values obtained after maximum

(a) Theta vs Alpha   (b) Theta vs Beta   (c) Theta vs GammaL
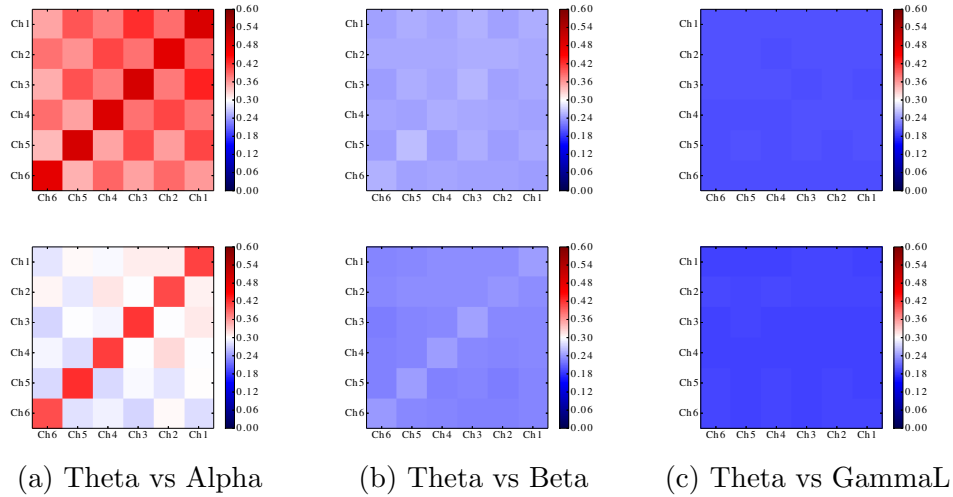
Figure 20: Cross-frequency phase synchrony matrix for theta: Coma (Up) vs QBD (Down). The matrices of phase synchrony index show the cross-frequency coupling for theta with respectively a) alpha, b) beta and c) gammaL. The first row of matrices is related to the coma state; the second row is related to the QBD state. Each matrix has six by six dimension, to represent the PSI for each pair of electrodes, from Ch1 to Ch6.

(a) Alpha vs Beta   (b) Alpha vs GammaL
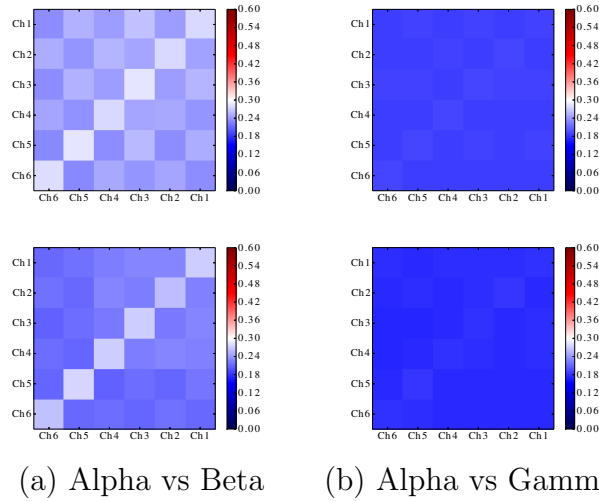
Figure 21: Cross-frequency phase synchrony matrices for alpha: coma (up) vs QBD (down). The matrices of phase synchrony index show the cross-frequency coupling for alpha with respectively a) beta and b) gamma. The first row of matrices is related to the coma state; the second row is related to the QBD state. Each matrix has six by six dimension, to represent the PSI for each pair of electrodes, from Ch1 to Ch6.

statistic, as explained for the within-frequency phase analysis, section 3.5.3. Computing the final p-value is as follow: the number of samples in the distribution above the original t-value (lower-left part of the table) is divided by the total number of samples in the distribution. For example, phase synchrony between delta and alpha bands are significantly different ($p = 0.1\% < 5\%$) between the state of coma and QBD. Phase synchrony between alpha and beta is not significant ($p = 57.8\% > 5\%$). The statistically significant cross-frequency bands are highlighted in red.

	Delta	Theta	Alpha	Beta	GammaL	GammaH
Freq. (Hz)	0.5-4.5	3-7	8-12	18-22	28-32	38-42
Delta		0.016	0.001	0.009	0.056	0.073
Theta	2.928		0.004	0.123	0.347	0.436
Alpha	3.867	3.417		0.578	0.038	0.055
Beta	2.983	1.778	0.799			0.997
GammaL	2.264	1.363	2.512			
GammaH	2.204	1.404	2.392	-0.910		

Table 3: Statistical results in cross-frequency coupling. It presents the results for the cross-frequency coupling between delta, theta, alpha, beta, gammaL and gammaH (gammaH is not significant with any frequency). The frequency band is indicated in the second row. The table is divided between the top-right part and the bottom left to indicate the statistical results of cross-frequency, respectively the p-value and the original t-value. Significant p-values are highlight in magenta.

3.7 Maximum Statistics on Within and Cross-Frequency

This analysis combines the results of within-frequency and cross-frequency coupling. It allows to avoid the multiple comparison issues due to the different within-frequency and cross-frequency comparison.

The surrogate groups are done by permuting the 17 values of PSI in coma

with the 17 values of PSI in QBD for a particular pair of electrodes. This is done for each pair of channels, and over all the frequency bands: within and cross-frequency. As a result there are two three-dimensional (channel by channel by frequency band) matrices, each entry containing 17 shuffled values from coma and QBD. For each entry of these both matrices, a two-sample t-test was applied between these two surrogate matrices, and the t-value recorded. The maximum t-value between the different pairs and frequency bands is selected. This is like section 3.5.3, step c) but including the different within and cross-frequency. This procedure is repeated to build the distribution with 100000 samples. This number of samples was chosen empirically to obtain a smooth distribution. To obtain the final p-value, we divide the number of values in the distribution which are above of the initial t-value with the 100000 values in the distribution.

Table 4 presents the statistical results. In this table, the lower-left part of the table is the t-value from the original two-sample t-test. For example, in the delta-theta coupling, the t-value is 2.928. The final statistics are presented at the upper-right part of the table 4. Each value is the p-value for each frequency band after maximum statistic. For example, for the cross-frequency delta versus theta, the value in the first line of the upper part of the table (delta) and the second column (theta) is 0.117.

3.8   Laplacian Filter

Volume conduction can be an issue when applying phase synchrony. As shown in figure 22, the same neural source can be recorded from two different channels, for example the source in green toward the top of the brain is recorded by Fz and Cz. This means that the phase synchrony between Fz and Cz can be high, but not

Freq. (Hz)	Delta 0.5-4.5	Theta 3-7	Alpha 8-12	Beta 18-22	Gamma L 28-32	Gamma H 38-42
Delta	0.147	0.117	0.018	0.117	0.387	0.387
Theta		0.043	0.043	0.645	0.809	0.809
Alpha			0.025	0.961	0.274	0.328
Beta				0.975		1
GammaL					0.999	
GammaH						1
Delta	2.831					
Theta	2.928	3.466				
Alpha	3.868	3.418	3.656			
Beta	2.984	1.779	0.799	0.609		
GammaL	2.264	1.364	2.513		-0.143	
GammaH	2.204	1.405	2.392	-0.910		-0.352

Table 4: Statistical results in overall frequencies. Results for the within and cross-frequency coupling between delta, theta, alpha, beta and gammaL are presented. The frequency band is indicated in the second row. The table is divided between the top-right part and the bottom left to indicate the statistical results of cross-frequency, respectfully the p-value and the t-value. Significant p-value with a threshold of 0.05 are highlight in magenta.

because of two different neural sources connected to each others and oscillating in synchrony, but because the same source is recorded by two different channels.
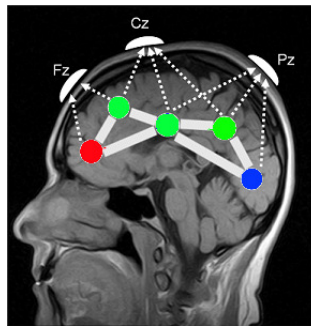
Figure 22: Volume conduction in the brain. The same neural source can propagates to different channels (e.g. two channels), which causes a spurious phase synchrony to be detected. (Adapted from: *http://www.oakland-mri.com/home.*)

To solve this issue, one possible solution is to use Laplacian filter. Each channel is transformed using the difference between the channel and a weighted average

of the surrounding ones, to get the sources away from the channel to be discarded (Carvalhaes and de Barros 2015). In Fig 22, Fz may records mainly (for example) the red source while Cz records the green source in the middle. Using this filter, activity from the green source on the left, common to both Fz and Cz, is diminished. The phase synchrony observed after Laplacian filter will take into account the red and the middle green activity. In the case of a relationship between these sources, phase synchrony can be detected between channels Cz and Fz. Phase synchrony analysis has been applied with and without Laplacian filter and results in stronger connectivity with the Hilbert method, but weaker connectivity with the wavelet method, after applying Laplacian filter (Berthelot, Witon and Li 2017).

Because analysing scalp level EEG data doesn't reveal sources (dipoles) in the brain, in the following Chap 4 and 5 we will investigate more on sources localisation methods.

3.9   Discussion

The results reveal that phase synchrony analysis between coma and QBD are statistically significant for the coupling between delta-alpha, theta-alpha and in theta band and alpha band, as shown in table 4. Synchrony is also detected between the lower cross-frequency coupling in theta-alpha in coma but not in QBD as shown in Fig. 20. An exception is a quite high synchrony in QBD in delta-theta, as shown in Fig. 19, suggesting there can be residual slow waves until brain-death. Interestingly, the statistical results within-frequency show that theta and alpha bands are significant, and they are reliable enough to stay significant in the last statistical result (overall frequencies). Moreover, overall statistics give stronger

evidence for the cross-frequency results. The highest frequencies (i.e. gamma band), involved in higher levels of the cognitive process are neither significant, not in cross-frequency or within-frequency after a maximum statistics over all the frequencies.

These results are concordant with Canolty et al. (2006), as the theta and gamma bands are phase locked in healthy subjects, but not during severe pathological disease like coma. In these conditions the phase locking occurs in lower frequency as it has been found in our results for the theta-alpha frequency coupling. We postulate that in pathological conditions lower frequencies are more active and take the drive compared to higher frequencies. Also, a coupling is operating in coma state, where patients may have the ability to produce minimal brain activity, and a collective behaviour inside the brain could emerge (Peat and briggs 1990), which is not the case in QBD. We present to our knowlede the first study on connectivity analysis and demonstrate the potential of using phase synchrony to distinguish between coma and QBD patients, with both within-frequency analysis and cross-frequency analysis. Further recording and analysis should be conducted to be able to propose a reliable tool assisting doctors for monitoring and diagnosis purposes. Particularly, analysis could be done to evaluate the possibility to classify one subject either in coma or quasi-brain-death. This can be done by machine learning algorithm with a Jack knife method: all subject but one are use as a training set to create a classifier (e.g. support vector machine). The remaining subject can be used to test the classifier.

Chapter 4

Source Reconstruction, Theory and Dipole Modelling Application

4.1 Chapter Outline

In this chapter, we describe the theory behind the source reconstruction of EEG activity. First, we show the physiology of the brain and describe how their electromagnetic properties explain the propagation of the signal to the scalp. Then, we present the mathematical tools used for the source reconstruction using imaging method and Equivalent Current Dipole (ECD). Then, simulation of source inversion using ECD were presented with model comparisons. Using Bayesian framework, we applied the ECD to the sedation/recovery data with the local-global paradigm using successively 1) parameters optimisation, and 2) models comparison. The results show that the local effect can be explained by dipoles in the temporal region, while global effect needs a broader network of dipoles including frontal, temporal and parietal dipoles.

4.2 Biophysic of the Brain

4.2.1 Electro-Physiology of the Neuron

Every cognitive activity is the result of thousands of neurons firing together, the micro-columns with the interaction of multiple areas in the brain. In the cortex, cell assemblies, composed mainly of pyramidal cells, fire together and form the micro-columns responsible for the neuronal synchrony (Varela 1994). A neuron can be described by the 'integrate and fire' model with dendrites as the inputs of integration, soma as the integrator and threshold function and axon as the output. The connection between two neurons, the pre-synaptic neuron and the post-synaptic neuron, is realised by the synapses, as shown in Fig. 23[1]. Post-synaptic potentials are electrical potentials at the level of the synapse.
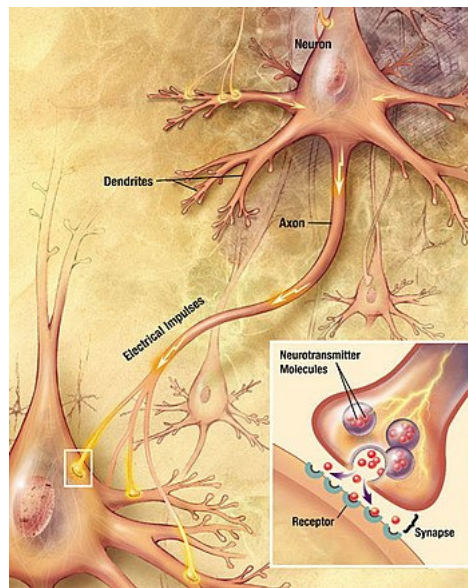
Figure 23: Propagation of electrical signal in the brain. The signal is propagating from a neuron's axon to a dendrite of another neuron. This creates an electromagnetic field which propagates up to the scalp.

---

[1]Figure in public domain from: *https://www.nia.nih.gov/*

Either a chemical synapse, by neurotransmitters' activation, or a direct electrical synapse generates the post-synaptic potential, which lasts for about 10 ms. The summation of post-synaptic potentials from other neurons' axon are summed up together up to the soma, and there might be excitatory post-synaptic potential (EPSP), or inhibitory post-synaptic potential (IPSP), depending on the type of neurotransmitter. Then, from the integration of all the EPSP and IPSP in the soma, when an electrical threshold is reached (about 20mV above the resting baseline), an action potential is generated. These action potentials are short electric potentials, lasting around one millisecond, and they propagate to the axon up to the dendrites of the next neurons, to generate other EPSPs or IPSPs (Spruston 2008).

At the level of the cortex, pyramidal cells have a parallel organisation responsive to the cells assemblies. When firing together, the electrical field can propagate to the scalp. In each neuron of the macro-column, the massive EPSP (generated mainly at the apical dendritic tree) and the massive IPSP (generated at the basal dendritic tree) generate a bipolar electrical imbalance. An electrical dipole can model this imbalance. Because cells' soma conducts the current, the dipole is located at the level of the cells. The dipole models a current generator, and the current traversing the cells is the primary current. The secondary current occurs when the current propagates in the conducting medium from the brain to the scalp. The recording of electrical activity at the scalp level (EEG) is due to secondary currents, while in the case of MEG the magnetic field recorded is due mainly to the magnetic field created by the dipole at the level of the primary current. This is summarized in Fig. 24 (Baillet, Mosher and Leahy 2001). In this figure, the panel on the left shows EPSE and primary and secondary current at the level of a pyramidal cell, as part of a macro-column. The middle panel presents

macro-columns in the brain with the different layers of cerebrospinal fluid (CSF), skull and scalp. Finally, the right panel shows the neural activity inside a head model.
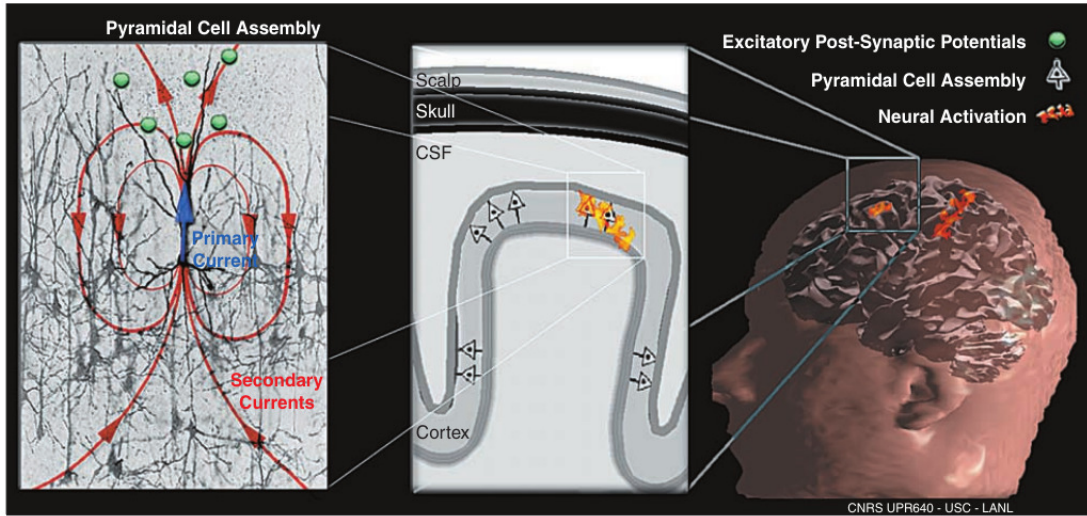
Figure 24: M/EEG generation: from cell assembly to neural activation. This shows respectively, from left to right, a pyramidal cell (left) from a macro-column inside the different brain layers (middle), and the brain activation in a head model (right).

4.2.2 Electromagnetic Field Propagation

This section describes the physical properties and the propagation of the electromagnetic field of the dipole. The equations describing the electric and magnetic field are possible using the quasi-static approximation of the Maxwell equations (see Baillet, Mosher and Leahy (2001) for detail).

In these conditions, $E = -\nabla V$. Where E is the electric field and V the primary potential of the dipole. We have seen that the current distribution can be divided into the primary current $\boldsymbol{J}^p$ at the level of cell assemblies, and the secondary currents $\boldsymbol{J}^v$, known as return current or volume current, which is the

current circulating through the medium of the head, composed of the different tissues (white matter, gray matter, CSF, skull, and scalp). Let r_q be the location of the dipole, and r being the location at the sensor level on the scalp. The secondary current, passive, is linked to the electric field by the conductance $\sigma(r)$ of the tissue by $\boldsymbol{J}^v = \sigma(r)\boldsymbol{E}(r)$. The equation for these two currents are: $\boldsymbol{J}(r) = \boldsymbol{J}(r)^p + \boldsymbol{J}(r)^v = \boldsymbol{J}(r)^p + \sigma(r)\boldsymbol{E}(r) = \boldsymbol{J}(r)^p - \sigma(r)\nabla\boldsymbol{V}(r)$. The primary current is modelized by a charge $\boldsymbol{q}$, as $\boldsymbol{J}^p = \boldsymbol{q}\delta\left(r - r_q\right)$, where δ is the dirac function.

4.2.3 Head Model

The electromagnetic fields need to pass from the assemblies responsible for the dipole equivalent activity through the conducting medium of the brain up to the scalp. Different head model complexities have been set up over years. The simplest one models the head as a single sphere. In this case, the contribution of an equivalent dipole i having a current density $\boldsymbol{J}^i$, is equivalent to: $\boldsymbol{\Phi} = \frac{1}{4\pi\sigma}\int_v \nabla\left(\frac{1}{r}\right) \cdot \boldsymbol{J}^i dv$. Where, $\boldsymbol{\Phi}$ is the electric potential, and r is the distant location of recording. More accurate models are made using Boundaries Element Methods (Kybic et al. 2005) and take into consideration the brain, skull and the scalp with their different propagation properties.

4.2.4 Forward Model

For EEG-based source inversion, the forward model aims to find the electric $\boldsymbol{E}(r)$ fields on the scalp, given the contributions of the dipole sources from the primary current $\boldsymbol{J}^p(r_q)$ within the brain.

The primary current from a dipole at the location $r_{qi}(i = 1, 2, ..., d)$ can be described by its moment (or amplitude) q_i, and its orientation $\Theta_i = \frac{\boldsymbol{q}}{q_i}$, with

$\Theta_i = \{\theta_i, \phi_i\}$ θ and ϕ being the spherical coordinates. We use the transfer function l to define the forward model of the electric field. Activation of the activity on the scalp results in the contribution of multiple dipoles, which can be added and result to the measurement: $y(r_c) = \sum_{i=1}^{d} l(r_c, r_q i, \Theta_i) q_i$, where c is the number of the channel recorded via the scalp EEG, and $i = 1, ..., d$ is the number of dipoles. Moreover, these equations can apply for any point of measurement, where $c = 1, ..., N$, with N being the total number of channels for the scalp EEG. For source reconstruction, it is common to have more than one hundred sensors. For N sensors and d dipoles, we can then use matrices form to compute $\boldsymbol{y}$:

$$\boldsymbol{y} = \begin{bmatrix} y(r_1) \\ \vdots \\ y(r_N) \end{bmatrix} = \begin{bmatrix} l(r_1, r_{q1}, \Theta_1) \ldots l(r_1, r_{qd}, \Theta_d) \\ \vdots \ddots \vdots \\ l(r_N, r_{q1}, \Theta_1) \ldots l(r_N, r_{qd}, \Theta_d) \end{bmatrix} \begin{bmatrix} q_1 \\ \vdots \\ q_d \end{bmatrix} = \boldsymbol{L}(r_c, r_{qi}, \Theta_i) \boldsymbol{a}, \quad (11)$$

where $\boldsymbol{L}$, is the lead-field, or gain matrix, which is the transfer matrix from the d dipoles with their coordinates (r_{qi}, Θ_i), to the activity of the $N^t h$ sensor at location r_s, where $s = 1, 2, ..., N$. Each of the columns of the matrix L is a gain vector, which explains the contribution of one dipole to the measures at the level of the N sensors. $\boldsymbol{A}$ is the vector of amplitudes produced by the dipoles q_i. Finally this model describes the neural propagation for a discrete single time point but can be extended for T time samples, by:

$$\boldsymbol{Y} = \begin{bmatrix} y(r_1, 1) \ldots y(r_1, T) \\ \vdots \ddots \vdots \\ y(r_N, 1) \ldots y(r_N, T) \end{bmatrix} = \boldsymbol{L}(r_c, r_{qi}, \Theta_i) \begin{bmatrix} \boldsymbol{a}_1^T \\ \vdots \\ \boldsymbol{a}_d^T \end{bmatrix} = \boldsymbol{L}(r_c, r_{qi}, \Theta_i) \boldsymbol{A}. \quad (12)$$

79

$$\boldsymbol{Y} = \boldsymbol{L}(r_c, r_{qi}, \Theta_i)\boldsymbol{A}. \tag{13}$$

Matrix A is for the sources time-series, $A \in \Re^{[d, T_s]}$ for the d dipoles. Each row of the matrix $\boldsymbol{Y}$ is the time-series of the measurement at the sensor level, while element $\boldsymbol{a}_i^T$ is a vector of time-series $\{q_i(1), q_i(2), ..., q_i(T)\}$ for the $i^t h$ dipole.

In practice, the location of the electrode r_c, and the location of the dipoles r_{qi} must be in the same coordinates. However, each of them is usually set up in their own coordinates: the dipoles are usually described in an MNI or similar coordinates related to brain imaging modalities, such as fMRI; whereas EEG sensor coordinates are described in their own system. A co-registration step is used to convert between these two coordinate systems. At least three points should be used in this case, usually the nasion, mastoid left, mastoid right, whose coordinates are common in both. Therefore, after this step one coordinate system is used, which is in MNI coordinates in our application.

4.3 Sources Activity: the Inverse Problem

4.3.1 General Overview

The previous section provides the general formulation of the following problem: given the measurement recorded via the scalp, how to reconstruct the original sources which has propagated through the lead-field? This is an ill-posed problem because there is no unique solution. Two main approaches have been developed to solve this problem. The first approach, Imaging Method, assumes that each dipole in the brain can be activated. Orientations in these conditions are constrained by an orthogonal orientation of the dipole to the surface of the scalp.

This problem is highly undetermined, given the number of known measurements: the N sensors are about a hundred, compared to the activity of d dipoles of the brain mesh, which usually include thousands of dipoles. However, because the position and orientations of dipoles are fixed, mathematical methods have been developed to turn this equation into a linear problem (Baillet and Garnero 1997). The second method, Equivalent Current Dipole (ECD), considers that few dipoles are activated to generate the brain activity. This method with few equivalent current dipoles is non-linear and can be solved by optimisation methods. Parameters $\{r_{qi}, \Theta_i\}$ defined the set of parameters to optimised, composed of three for the location, and two for the orientation.

4.3.2 Equivalent Current Dipole

On the Equivalent Current Dipole (ECD) method, the hypothesis is that the brain activity is the result of few activated dipoles in the brain (Kiebel et al. 2008). The small number of dipoles (< 10) used must be decided as a priori. This chapter focuses on ECD inversion with assumption of a small number of dipoles activated. We do the hypothesis that a small number of dipole can explain the local-global with sedation task. We will investigate more using MSP in the following chapter, where the brain is represented as a mesh of dipoles activity (few thousands). Bayesian framework is used for ECD inversion, and two levels of Bayesian inference are possible either *parameters fitting* or *model selection*, as presented in Fig. 25. The process for ECD source reconstruction can be resumed by the following steps:

1) Specify the model (number of dipoles, symmetry).

2) Add prior knowledge to the parameters of the model, like expected position of

a dipole in a specific brain area.

3) Run optimisation Bayesian scheme (Variational, EM...), this is the first level of inference.

4) When minimization is reached the parameters provide a solution, and the model evidence can be used for further model comparison.

5) Run the above steps for another model and/or others parameters, this is the second level of inference.

6) Select the best model based on Bayes factor.

An advantage of Bayesian statistic is to use the knowledge of the data as prior information $P(\theta)$. This allows finding the posterior distribution that best explain the brain activity observed. This framework is based on Bayes' rules which states that the posterior distribution is the likelihood time the prior scaled by the evidence.

ECD parameters fitting

At the first level of inference the ECD model is selected, we call it $\mathcal{H}$, that is expected to be correct. The aim is to find the optimised parameters of the dipoles included in the model, i.e. the location and orientation parameters. For example, a two dipoles model has been used in an oddball auditory task on a group of deaf and healthy people listening to music. It was found a statistical difference of the localisations from ECD reconstructed dipoles between both groups (Barascud et al. 2014).

We infer what the parameters θ might be, given the scalp-map data Y, with θ being the vector of parameters optimisation. Using Bayes' theorem, the posterior
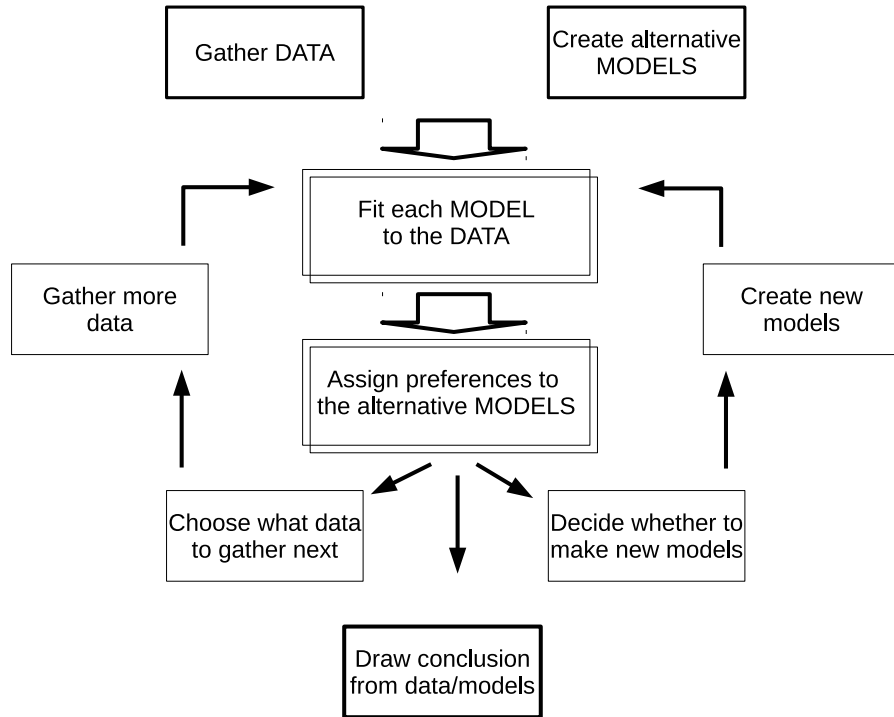
Figure 25: Graph showing Bayesian inference in the data modelling process. This figure, reproduced from Mackay (2003) Chap. 28, illustrates a part of the scientific process in which data are collected and modelled. The two-centred boxes refer to the two steps which involve *inference*. It is only in those two steps that Bayes' theorem can be used, as it does not tell, for example, how to invent models. The first box, 'Fit each model to the data', is the step of inferring what the ECD parameters might be used for the model and the scalp EEG. Variational Bayes methods are used to find the most probable parameters values for ECD parameters. The second inference task, the model comparison in the light of the data, is where Bayesian methods stand. This second inference problem requires a complexity term to penalise over-complex models. Free Energy method based on Variational Bayes, can assign objective preferences to the alternative models in a way that automatically embodies complexity.

probability of the parameters θ is:

$$P(\theta|Y, \mathcal{H}_k) = \frac{P(Y|\theta, \mathcal{H}_k)(P(w|\mathcal{H}_k)}{P(Y|\mathcal{H}_k)} \tag{14}$$

The normalising constant $P(Y|\mathcal{H}_k)$ is usually ignored as it is unnecessary to

the first level of inference, i.e. parameters optimisation, but it becomes important in the second level of inference. It is named the *evidence* for $\mathcal{H}_{\parallel}$. It is common practice to use gradient-based methods to find the maximum of the posterior, which search for the best value for the parameters θ. The method we used for the ECD inversion is the Variational Laplace (Kiebel et al. 2008). Symmetry between two dipoles were specified as prior parameters. For example, a pair of symmetric dipole is defined by having their x orientations of opposite side, i.e. $x_{left} = -x_{right}$. The y and z coordinates are the same for both left and right dipoles. These symmetric prior are defined by the covariance matrices of the parameters.

ECD Model Comparison

The purpose of this second inference is the possibility to compare between different models and select the best one (Penny et al. 2004). The performance of a model (m_k) is expressed by using the posterior probability:

$$P(\mathcal{H}_k|Y) \propto P(Y|\mathcal{H}_k)P(\mathcal{H}_k) \tag{15}$$

The data-dependant term $P(Y|\mathcal{H}_k)$ is the evidence for $\mathcal{H}_k$, which appeared as the normalising constant in the first level of inference. The last term, $P(\mathcal{H}_k)$, is the subjective prior over the model space. We assume the models to have the same probability. Then, ranking the models is equivalent to ranking the evidence $P(Y|\mathcal{H}_k)$. In particular, the log-evidence is used, which allows summing different evidences. This is particularly useful at a group level, where the evidence for each subject can add up together. Using the SPM 12 toolbox for dipole modelling, the evidence is equivalent to the Free Energy after dipole optimisation.

Then, a Bayes factor is computed, based on the comparison of the model evidence between two different models $\mathcal{H}$. Given two models k and m, we have:

$$B_{km} = \frac{P(Y|\mathcal{H}_k)}{P(Y|\mathcal{H}_m)} \qquad (16)$$

The interpretation of the Bayes factor is explained by the following table.

B_{km}	$p(\mathcal{H}_k|Y)(\%)$	Evidence in favour of model (k)
1-3	50-75	Weak
3-20	75-95	Positive
20-150	95-99	Strong
≥ 150	≥ 99	Very strong

Table 5: Inference of Bayes factor. The first column is the Bayes factor B_{km} between model k and m. The second column is the probability to favor for the model k, given a set of data.

Given model hypothesis m_k and m_m, a Bayes factor of 20 (third row in Table 5) corresponds to a belief of 95% in the statement 'hypothesis k is true'. This corresponds to a strong evidence of model k. Instead of dividing the two model evidence to have the Bayes factor, it is common to take the log-evidence, then the Bayes factor is the difference of log-evidence: $log(P(Y|m_k)) - log(P(Y|m_m))$. For a strong evidence of model k, the difference of the log-evidence between the two models should be at least: $log(20) = 3$.

Simulation: Source Inversion for ECD Model Comparison

In this section, we present simulations on a ECD-based source reconstruction. Firstly, we simulated a scalp map based on the activity of two symmetric dipoles. The first scalp map is generated using dipoles in temporal (A1, primary auditory cortex), and the second one using dipoles in parietal (SPC, Superior Parietal Cortex). Secondly, two different models were used for the ECD inversion. The

two models used for the source inversion were used for model comparisons.

The steps for this synthetic source reconstruction are: 1) Select the dipoles parameters (number of dipoles, location) for the data.

2) Build the scalp-map activation from the forward model and chosen dipoles' parameters.

3) Based on a model, find the sources and model evidence using ECD inversion.

4) Repeat the source reconstruction for another set of priors (model).

5) Using model selection, select the most appropriate model using the Bayes factor (log-evidence differences).

Simulation: Temporal Sources Dipoles

The two symmetric temporal source dipoles used to create the synthetic scalp-map are located in the primary auditory cortex. We used the following parameters from (Garrido et al. 2008), with S_0 being the location matrix: the coordinates for the left hemisphere are $(-42, -22, 7)$ and for the right hemisphere: $(46, -14, 8)$. The orientation of the dipoles was defined by the moment W_0, with the (x,y,z) coordinates for the left and right hemisphere are $(0, 0, 100)$. We selected arbitrarily a dipole oriented toward the top of the head. These parameters were used to simulate the scalp map and no noise was added. Fig. 26 shows the scalp map of activities generated from the temporal dipoles. Activity is symmetric, with a maximum in the middle of the scalp, around Cz. Then, activity decreases and goes negative in the lower part of the head. ECD inversion was applied to search for the expected dipoles location. Two different models were used: the first model included priors in temporal lobes, and the second model included priors in parietal lobes. The left and right coordinates for parietal were respectively $(-30, -57, 42)$ and $(33, -57, 45)$ chosen from Bekinschtein et al. (2009). The goal is to retrieve

the best model related to the dipoles used for the scalp-map generation, i.e. here in temporal.

Fig. 27 shows the output of ECD inversion based on the model with parietal priors. The left shows the predicted scalp EEG map using the sources found via ECD. This output is very similar to the original simulated data in Fig. 26. The right figure shows the relationship between original and simulated dataset for each channel. Each blue dot is a channel, and the x-axis is the original measured activity, while the y-axis is the predicted activity. If they are both exactly similar, there is a perfect similarity between the x-axis and the y-axis for each channel, and the dots should follow a straight line from the lowest value (bottom left), to the highest value (top right). In this inversion, even if the predicted data has been optimised using priors with dipoles in parietal, there is strong confidence between the predicted and the synthetic (measured) data. This is due to the simplicity of the simulated dataset: with very focal dipoles used for the simulation, even priors far from original source can give good results for the inversion. This also shows the importance for next step (model comparison).
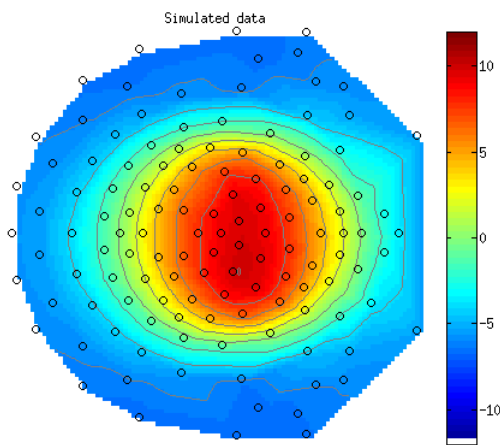
Figure 26: Simulated scalp map for auditory sources. The scalp map was generated with symmetric dipoles from primary auditory cortex.
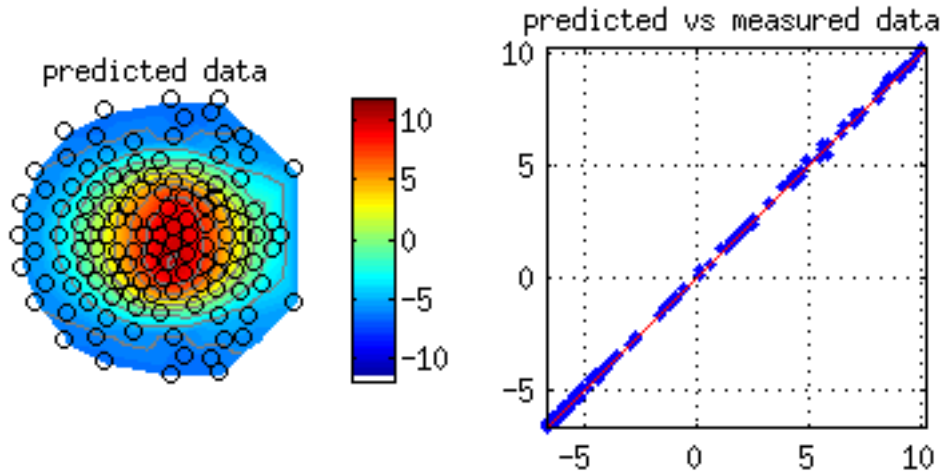
Figure 27: Source reconstruction from ECD inversion with parietal prior. The predicted scalp map is shown on the left, and relationship between the predicted and the synthetic (measured) data for each channel is on the right.

Finally, a model comparison was performed between the two different models. The first one is a model with priors in the temporal lobes, i.e. over-informative, and the other model has prior in the parietal lobe, i.e. under-informative. We compared the model evidence for each model described by the F-value, as shown in Fig. 28. This graph shows with the y-axis being the Free Energy for each model, and the different models are shown on the x-axis. The model indicated by A1 is the model with temporal priors, whereas the model indicated by SPC is with parietal priors. The bar on the left (F-value) is the Free Energy for the temporal model, while the bar on the right is the Free Energy for the parietal model. The difference between the two model is $F_{Temp} - F_{Parietal} = 1588 - 103 = 1485$, which favours very strongly the A1 model (temporal model).

Simulation 2: Parietal Sources Dipoles

The parietal source dipoles were chosen from the Superior Parietal Cortex
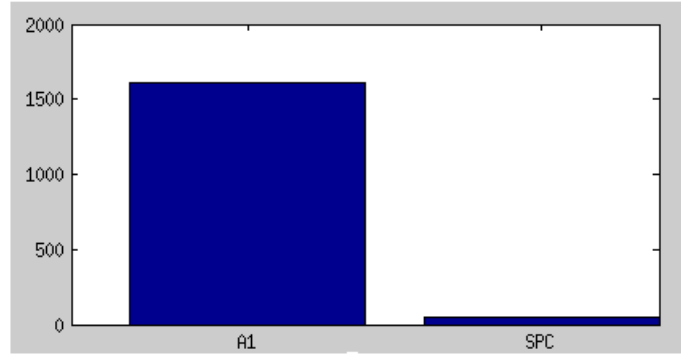
Figure 28: Free Energy model comparison for temporal sources. Model evidence based on the free energy for models with temporal prior on the left and parietal prior on the right.

(SPC). We used the following parameters, with S_0 the location matrix with the coordinates (x, y, z) for the left and right hemisphere respectively $(-30, -57, 42)$ and $(33, -57, 45)$. And the orientation of the dipoles was defined by the moment matrix W_0, with the first and second column for left and right hemisphere, and the three rows for x,y, and z coordinates. We selected arbitrarily a dipole oriented toward the top of the head, with S_0 the orientation for the left and right hemisphere respectively $(0, 0, 100)$ and $(0, 0, 100)$.

From these dipoles parameters, a scalp-map of EEG activity as shown in Fig. 29 was simulated using a forward model. The scalp map is symmetric, with a strong maximum in the middle of the scalp, slightly on the back of the head. ECD inversion was applied on this scalp map dataset, with two different models, to search for the best model which explain the data. The first model included priors in temporal lobes, while the second model included priors in parietal lobes. In Fig. 30 to the left, it shows the scalp map based on the temporal dipoles obtained from ECD inversion for the model with temporal dipoles, which is very similar to the original simulated data. The right figure shows the relationship between

the synthetic EEG and the predicted EEG for each channel. Each blue dot is a channel, and the x-axis is the synthetic (measured) EEG activities, while the y-axis is the predicted EEG activities.
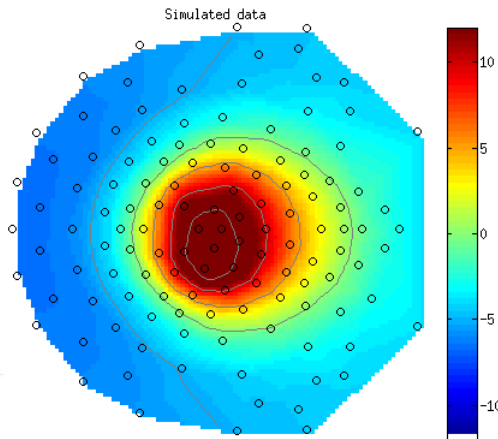
Figure 29: Simulated scalp-map for superior parietal sources. The synthetic scalp-map was generated with symmetric dipoles from superior parietal cortex.
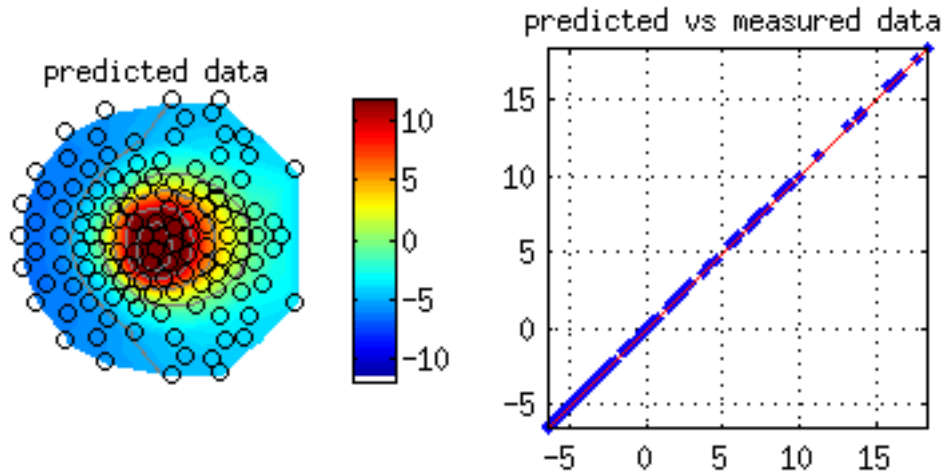
Figure 30: Predicted scalp map from ECD inversion (left), and relationship between predicted and measured data, for each channel (right).

Both Fig. 26 and Fig. 29 suggested even priors that are far away from the true location of the dipoles the scalp mapcan match the data well. Therefore model

comparisons were performed between two different models. The first model is a model with priors in the temporal lobe, and the other model have priors in the parietal lobe. We can compare the F-value for each model, as shown in Fig. 31. This figure shows Free Energy on the y-axis for each model shown on the x-axis. The left bar is the F-value for the temporal model, while the right bar is the F-value for the parietal model. The difference between the two model is $F_{Parietal} - F_{Temp} > 1500$, which favours very strongly for the parietal model.
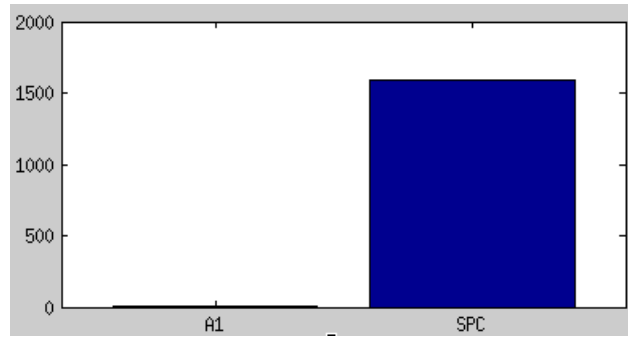
Figure 31: Free Energy comparison for parietal sources. Model evidence based on the Free Energy for models with temporal prior on the left and parietal prior on the right.

Model comparisons applied on these source inversions show that model comparison provides a genuine method to favour one model other another. Based on the scalp map, the predicted data converged similarly with both priors: either temporal or parietal. However, in term of model comparison, the model which has the closest prior wins largely. These simulation have been applied without added noise. It would be interesting to evaluate how the algorithm converges with decreased signal to noise ratio. Nevertheless, this method is suitable when few regions in the brain are engaged in the task to be modelled.

4.4 Application to the Sedation Dataset

4.4.1 Experimental Design

The local-global auditory oddball task, devised by (Bekinschtein et al. 2009), was implemented within this study to investigate differences between local and global effects after healthy sedation and subsequently in recovery. As shown in Fig. 32, local regularity was established using sequences of five tones, or quintuples, where the last tone may or may not vary from the preceding four tones (local deviance versus local standard respectively). Global regularity was established as the most frequently presented quintuple type within a block, either local standard (all five tones the same) or local deviant (different last tone). There were 4 block to counterbalance the pitch of the deviance. Thus, violations in global regularity were expressed by the presentation of a quintuple that was not the frequently presented pattern in the block. To ensure the establishment of global regularity, an habituation phase of 20 to 30 quintuples was presented at the beginning of the block. After the habituation period, the ratio between the standard and deviant quintuples was 80 to 20. This gave rise to four conditions: (1) local standard / global standard (LSGS), (2) local deviant / global standard (LDGS), (3) local standard / global deviant (LSGD) and (4) local deviant / global deviant (LDGD) (see b, c, d and a in Fig. 32). Quintuples were made up of 5 tones of 50ms duration each presented via headphones with an intensity of 70dB, an SOA of 150ms. All tones were synthesised with 7ms rise and 7ms fall times. Participants were asked to count the number of global deviants they heard during both sedation and recovery phases of the study.
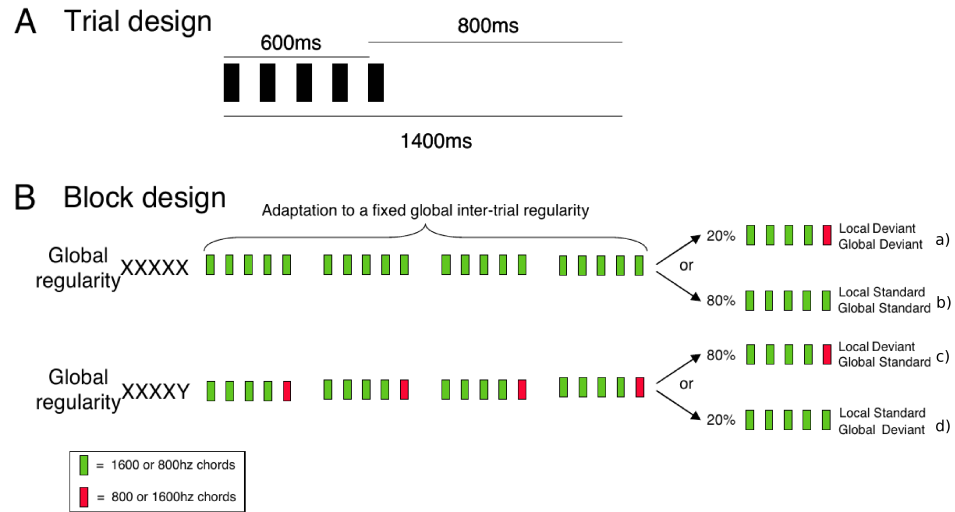
Figure 32: Experimental design for the local-global task. The local-global auditory task designed from (Bekinschtein et al. 2009). A) The trial design consists of five tones for 600ms, with a trial duration of 1400ms. B) The block design presents the four conditions analysed in the experiment: (b) local standard / global standard (LSGS), (c) local deviant / global standard (LDGS), (d) local standard / global deviant (LSGD) and (a) local deviant / global deviant (LDGD). The adaptation period sets the global regularity of the session. The probability transition (20% and 80%) set up the two levels of irregularity.

4.4.2 Sedation

The local-global task was presented on two occasions, once during either mild (half of participants) or moderate (the other half) sedation and once 20 minutes later, when participants were considered to be in recovery (ie. no longer sedated). Sedation in this study induced a heavily relaxed but still behaviourally responsive state in participants. All participants were tested both under sedation and subsequently in recovery creating a repeated measures design. Each experimental run began with an awake baseline period lasting 25-30 minutes followed by a target-controlled infusion of propofol (Marsh et al. 1991), administered via a computerized syringe driver (Alaris Asena PK, Carefusion, Berkshire, UK). Three

blood plasma levels were targeted – $0.6\mu g/ml$ (mild sedation),$1.2\mu g/ml$ (moderate sedation), and recovery from sedation. A period of 10 minutes was allowed for equilibration of calculated and actual plasma propofol concentrations before cognitive tests were commenced. Following cessation of infusion, plasma propofol concentration exponentially declined toward zero and would approach zero in 15 minutes leading up to behavioural recovery; hence why the recovery condition commenced 20 minutes after cessation of sedation.

All clinical investigations were conducted in accordance with the Declaration of Helsinki. The participants gave written informed consent and were healthy controls. Ethical approval for testing healthy controls was acknowledged by the Cambridgeshire 2 Regional Ethics Committee.

4.4.3 EEG Recording

Originally 22 participants were tested, but four recordings were lost due to technical issues. Therefore, 18 participants were taken forward for analysis. Participants were asked to close their eyes during data collection to avoid eye artefacts in the data. EEG data was collected at two occasions, during sedation and then recovery. A Net Amps 300 amplifier (Electrical Geodesic Inc., Oregon, USA) with a high-density cap of 129 channels was used for data collection. Channel locations were not digitalized per participants. The signal was recorded in microvolts (μV), with a sampling frequency of $250Hz$, and referenced to vertex (channel Cz). After recording, the data was segmented from -200ms before the first tone in a quintuple until 1296ms after that tone (for a total of 1500ms minus one sample per trial). Each trial was inspected for artefact rejection, and the remaining trials were re-referenced to average and band-pass filtered from 0.5 to $20Hz$ which are

the standard filter settings for this paradigm (Bekinschtein et al. 2009). Each participant dataset was then converted to the SPM toolbox for analysis.

Channels near the neck and eyes were discarded after conversion, due to confounding edge effects as a result of average referencing (36 out of the 129 channels). The reduced number of channels contributing to the inversion was compensated for by use of a mesh subspace to model the cortex.

The ECD source inversion was applied to the sedation dataset with local-global paradigm. We have described previously how the parameters of the ECD are optimised to find the best inversion with model evidence. For the rest of this chapter, we applied ECD method to distinguish the best sources for the local effect and the global effect for the sedation dataset. First, a sanity check was done to evaluate the effect of prior location from a pair of dipoles modelising the N1 after the first tone. We then applied statistical comparison to evaluate the location of the global effect by comparing both global standard and global deviant. Then, using more advanced Bayesian model evidence, we compared different models for local deviant and global deviant conditions. Some behavioural measurements were acquired but not analysed in the frame of this thesis.

4.4.4 Global Field Power and Evoked Potential

ECD inversion necessitates a scalp map as the input dataset. One possibility for selecting a scalp-map is by detecting the maximum of activation around a window of interest and to find the sources at this point of maximum activation. The Global Field Power (GFP) was used to find the time-course of global activation. It can be considered as a measure of spatial variance on the scalp and particularly useful to see global variation of activity on the scalp. For a particular subject s it is

defined by:

$$GFP_s(Spl) = \sqrt{\frac{\sum_{c=1}^{N} (Spl_c - \overline{Spl})^2}{N}} \tag{17}$$

where N is the number of channels, Spl is the recording amplitude for a particular time sample (Spl) and the channel c, and $\overline{Spl}$ is the mean of activity amongst all the channels. This value give the global scalp activation for one sample time point, and was applied to the ERP for each condition.
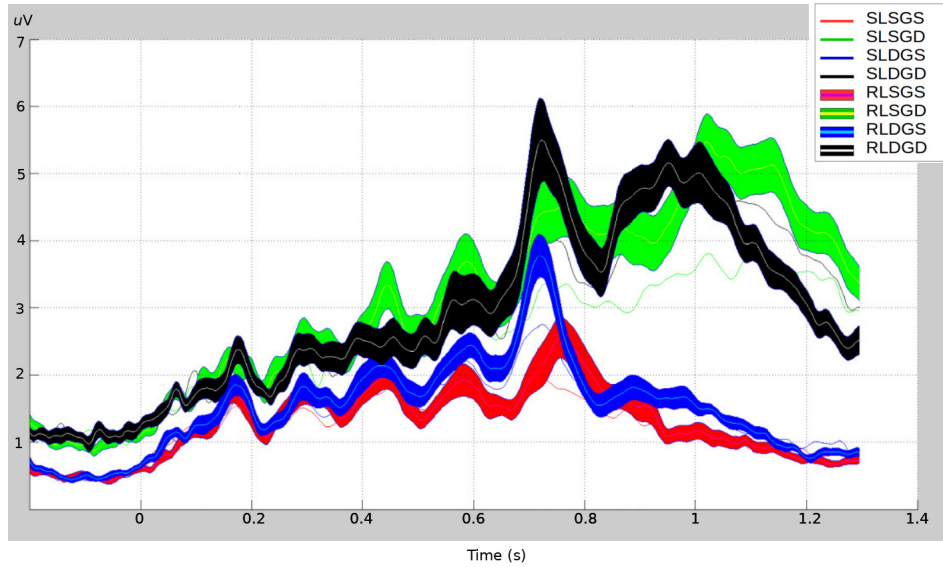
Figure 33: Global field power. The four recovery conditions are presented in green (RLSGD), black (RLDGD), red (RLSGS) and blue (RLDGS), with the standard error in the shaded area. The four sedations conditions are presented in the back in respectively green (SLSGD), black (SLDGD), red (SLSGS) and blue (SLDGS).

Then, the grand average of GFP has been applied amongst the 18 subjects for each condition (LSGD, LDGD, LSGS, LDGS). The Fig. 33 shows the GFP for the eight conditions of the local-global task. The baseline correction is applied to [-200; 0] ms before the beginning of the first tone. From this figure, a clear pattern is revealed between the global effect during the period with the window being [800; 1296] ms and local effect, covering window [650; 800] ms. Also, during

the baseline window, the global deviant (black and green curves) is different from the global standard (blue and red). This can be explained by the expectation that a subject puts in the incoming quintuple: it is higher during the global deviant while the global standard is the most familiar pattern. AS the subjects are listening the global standard, they expect more and more the global deviant to come. During the global deviant tone, there is a high expectation which create a stronger deviation during the baseline compare to the global standard. Indeed, after the global deviant, there is no more expectation for the next trial than to be globally standard. This tendency of the global effect during the occurrence of the five tones is less visible. Finally a clear pattern after 800 ms distinguishes between the global deviant and global standard conditions.

During the five tones, the pattern of brain response can be seen from the GFP for each condition (it is less clear on the LDGD), with a bump presents in the curve which correspond to the processing of each tone by the brain. Finally, the local deviant compared to the local standard is visible around 700 ms. The black and blue curves for local deviant have a big deflection while the red and green follow the pattern of the previous oscillations. We can also observe an early response of the global effect for LDGD compared to LSGD. For the LDGD condition, it occurs before 1000 ms and regularly declines at the end of the epoch, while for the LSGD, the maximum of activity for the global effect is after 1000 ms and sustains a more extended period. Finally, the global standard conditions return to normal (baseline level) at the end of the epoch, while for the global deviant the level is still high at the end of the window. This may reflect an engaged activity due to the global deviant pattern and link to a broad network of cognitive activity, that we explored with the source reconstruction.

The different condition at the ERP level are also shown in Fig. 34, for the

channel Cz. In this figure, we focus on the effect of the fifth tone, and the baseline is before 5th tone onset, from 400ms to 600ms. The dashed lines present the recovery conditions and stared ones the sedation. On recovery, the global deviant conditions are clearly present with the blue one for the local deviant (RLDGD), and with a delay there is the green one for local standard (RLSGD). For the global standard condition, the red dashed line shows the local deviant (RLDGS) and the black one the local standard (RLSGD). The same shapes apply for sedation conditions with a decrease in amplitude.
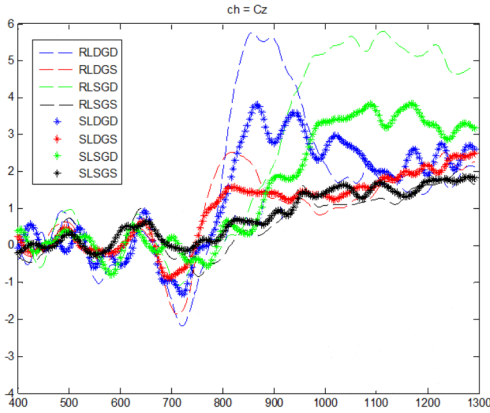
Figure 34: ERP of the local-global task. The different conditions are presented after the fifth tone for the channel Cz. The recovery conditions are in dashed line and the sedation conditions are shown with the stars. (Adapted from (Shirazi-Beheshti et al. 2018))

4.4.5   Sanity check

As shown in Fig. 33, the first tone elicits a bump of activity (i.e. N1) which is expected to be located in the auditory cortex. We applied ECD on this pattern of activity to explore the robustness of the method, as a sanity check. We explored the results of source inversion for each subject, by varying the location of the prior. In particular, we selected the primary auditory cortex as the prior ground

truth and modelled this activity by two symmetric dipoles close to the primary auditory cortex. The locations (x,y,z) of the auditory cortex as the ground truth are defined by $A1_{left} = (-42, -22, 7)$ and $A1_{right} = (46, -14, 8)$, using coordinates from literature (Garrido et al. 2008).

We successively changed the position of the prior in each direction: left, right, up, and down from the primary auditory cortex by steps of 5 mm up to 2 cm. Then a total of 24 source reconstructions were successively applied. For each source reconstruction, the source localisation algorithm ran 20 times to select the model which has the highest model evidence among the 20. We then evaluated the output location after source reconstruction.

Table 6 shows the mean output localisation for each subject. The grand average over the subjects is also presented and finally the location's difference from the auditory location. The first column indicates the index of the subject and group measures. The next three columns present the location for the dipole in the left hemisphere, and the last three columns are the locations for the right hemisphere. A constrain on the dipoles had been applied to have symmetric dipoles between left and right dipoles. This results in relative similar distances for y_l, y_r and for z_l, z_r, while x_l is opposite to x_r. Because the dipoles are symmetric, they are optimized together during the fitting dipole optimization (i.e. same variance parameters). We can see in the results that the difference (expected minus mean) for y and z coordinates are the same between left and right position. The Mean (group) row is the mean localisation over the 18 subjects. It can be compared with the expected location shown on the next line which is related to the primary auditory cortex (A1). The 'Diff. (Expected-Mean)' line shows the differences between A1 and the group mean. The source locations for the group mean are close to the auditory cortex, with a difference of 5.61mm for the y coordinate, 7.81 mm

for the z coordinate. The x-coordinate difference is between 6.92 to 7.48 mm. The

Subject	left			right		
	x_l	y_l	z_l	x_r	y_r	z_r
1	-51.47	-40.39	-25.83	54.56	-32.39	-24.83
2	-33.37	-19.90	-19.73	46.31	-11.90	-18.73
3	-45.10	10.82	-25.64	44.96	18.82	-24.64
4	-27.06	-12.40	14.73	29.28	-4.40	15.73
5	-40.10	-43.13	14.38	40.50	-35.13	15.38
6	-42.13	-13.47	20.93	45.50	-5.47	21.93
7	-38.79	-32.89	-13.12	37.76	-24.89	-12.12
8	-31.71	-53.21	2.40	34.56	-45.21	3.40
9	-37.04	-19.50	10.92	39.44	-11.50	11.92
10	-32.98	-45.62	9.25	39.67	-37.62	10.25
11	-20.56	-17.24	10.27	28.29	-9.24	11.27
12	-11.53	-45.76	-1.03	14.58	-37.76	-0.03
13	-34.61	-15.41	23.98	42.53	-7.41	24.98
14	-29.63	-49.16	-11.76	41.36	-41.16	-10.76
15	-32.37	-51.53	14.02	34.08	-43.53	15.02
16	-37.74	-43.15	-23.77	39.72	-35.15	-22.77
17	-39.90	12.83	-17.98	44.32	20.83	-16.98
18	-35.31	-17.84	3.45	46.02	-9.84	4.45
Mean (Group)	-34.52	-27.61	-0.81	39.08	-19.61	0.19
Expected (A1)	-42.00	-22.00	7.00	46.00	-14.00	8.00
Diff. (Expected - Mean)	7.48	-5.61	-7.81	-6.92	-5.61	-7.81
Std (Group)	8.98	20.35	16.91	8.82	20.35	16.91

Table 6: Mean location for each subject compared to primary auditory cortex. The first column is the index of the 18 subjects whose mean location are indicated in the next three columns for the left hemisphere and the last three columns for the right hemisphere. The 'Mean (Group)' row is the mean at the group level. It needs to be compared with the original prior shown in the 'Expected (A1)' row. The next row shows this difference, and the standard deviation of the group is in the last row.

last line presents the standard deviation of the measurement among the different subjects. The standard deviation is the same between left and right hemisphere due to symmetric prior. The standard deviation is 8.98 and 8.82 mm for the left and right x-coordinate respectively, 20.35 mm for the y-coordinate and 16.91mm for the z-coordinate.

These results show the mean of location for each subject and at the group level. The final locations are not precisely centred in the auditory cortex as expected. This may be due mainly to the approximation of the source inversion without MRI structural scan for each subject which generated inaccuracy. Also, this may be due to other neuronal contribution in the brain, which requires more than one pair of dipoles to reconstruct this brain activity. However, all the different inversions converge around the same location.

Then we analysed the standard deviation for each subject between the 24 source reconstructions, and we computed the mean of the standard deviation for the 18 subjects. The results are shown in Table 7. The first column is the index of subjects, the next three columns are the standard deviation for the (x, y, z) coordinates in the left hemisphere and the last three columns are the standard deviation for the coordinates in the right hemisphere. The top 18 rows show the standard deviation for each subject, while the last row is the mean of standard deviation over the subjects. The 'Group mean' for x coordinate, is 6.4 mm (between left and right hemisphere). This high value is mainly due to the two subjects (2 and 14). If these two subjects are rejected, the mean becomes 4.29 mm. For the y and z coordinates, the mean is respectively 3.45 and 3.41 mm, for both hemispheres.

Considering there is no structural scan of the subjects, the location found at the group level can be considerate a good approximation for the source reconstruction. However, the standard deviations show a large discrepancy between subjects. This may be due to anatomical differences amongst participants which makes an inaccurate forward model. These results show the good robustness of the ECD algorithm relative to the place of the priors and the availability to localise the output dipoles close to the expected position, even when the dipoles prior are moved forward from their expected location. This shows that ECD optimisation

does not fall in a local minimum, regarding of the initial prior.

Subject	left			right		
	x_l	y_l	z_l	x_r	y_r	z_r
1	4.03	7.59	14.03	4.36	7.59	14.03
2	18.21	2.16	6.15	17.47	2.16	6.15
3	8.78	4.47	4.38	7.65	4.47	4.38
4	4.23	2.52	2.65	4.04	2.52	2.65
5	1.32	0.72	0.63	1.14	0.72	0.63
6	4.63	4.13	4.53	4.42	4.13	4.53
7	3.37	2.09	2.04	3.70	2.09	2.04
8	2.72	1.03	1.30	2.55	1.03	1.30
9	4.95	3.90	3.55	3.29	3.90	3.55
10	14.82	3.08	2.25	15.20	3.08	2.25
11	8.18	13.00	4.41	7.81	13.00	4.41
12	7.24	3.80	3.09	6.90	3.80	3.09
13	3.31	2.33	1.54	1.84	2.33	1.54
14	22.69	1.23	1.33	23.07	1.23	1.33
15	3.59	5.60	4.85	3.42	5.60	4.85
16	1.18	0.38	0.56	1.03	0.38	0.56
17	2.29	2.81	2.53	2.41	2.81	2.53
18	2.46	1.31	1.57	1.53	1.31	1.57
Group mean	6.56	3.45	3.41	6.21	3.45	3.41

Table 7: Standard deviation of location per subject and group mean. The first column is the index of subjects whose standard deviation location are indicated in the next three columns for the left hemisphere and the last three columns for the right hemisphere. The last line is the mean of standard deviation at the group level.

4.4.6 Parameters Dipole Fitting

Dataset

We used the dataset to look at the differences of the ECD source localisation between the recovery local deviant global standard (RLDGS) and recovery local deviant global deviant (RLDGD) conditions. We analysed the effect of the first tone around 170 ms, then the fifth tone relative to the early response was studied

at 720 ms. Finally, the late effect was analysed for the peak of activation found at 894 ms. These time samples were chosen based on the GFP and adapted for each subject by the closest peak. The peak of activation correspond to the first tone, the fifth tone and the late effect respectively. The hypothesis was that the first and fifth tone should not generate any differences in the source reconstruction. Indeed the first tone does not include auditory irregularity. In this analysis, we examined the global effect, then we decided to select both conditions with local deviant and only change the global irregularity in both conditions analysed. Finally, the early response generated by the fifth tone should not be significant for the global effect.

Method

The ECD method is applied for the source reconstruction with a model of four symmetric dipoles. It consists of two pairs of symmetric dipoles with one pair placed in the temporal area, and the other in the frontal area, to reproduced a model from (Garrido et al. 2008). This inversion is applied for the 18 subjects, and for the two conditions RLDGS and RLDGD. For each of the time sample of interest (i.e. first tone, fifth tone and late effect) the closest peak on the GFP of each subject was selected, and the scalp map related to this peak used for the source reconstruction.

The results were compared between the two different conditions for each effect. A statistical paired t-test has been applied to each dipole location between global deviant and global standard. The distance of each dipole from the origin has been used to compare the two conditions. The distance is computed as follow: $D = \sqrt{x^2 + y^2 + z^2}$, for each dipole, each condition and each subject. The dipoles are successively temporal left, temporal right, frontal left and frontal right. The conditions are either RLDGS or RLDGD. Moreover, the 18 subjects were included

for the statistical test. Then for each dipole, we explored the null hypothesis that there is no difference in the location between the two conditions. Finally, the mean location for each dipole is also computed to report on the results.

Results

We first looked at the source localisation for the first tone. The mean location results for the first tone are shown in Table 8. For each dipole listed in the first column, the mean location for the RLDGS and RLDGD conditions is reported in the x, y and z columns respectively. The dipoles between both conditions have a similar location, with the frontal dipoles being more central in the RLDGS condition compared to the RLDGD.

Dipoles	RLDGS			RLDGD		
	x	y	z	x	y	z
Temp_L	-23.2	-34.7	-6.03	-26.21	-37.36	-0.17
Temp_R	28.31	-27.83	-2.13	27.99	-33.47	-3.12
Front_L	26.31	-2.42	-9.53	35.61	-3.54	-10.11
Front_R	-25.84	-13.92	-7.01	-34.64	-4.02	-12.48

Table 8: Localisation of the dipoles in each condition for the first tone. Each row is related to a dipole location, with name in the first column. Then, the mean location for each dipole is reported in the x, y, and z coordinates for the RLDGS condition and RLDGD condition.

The results of the statistical test for each dipole between both conditions are shown in Table 9. We can see that there is no difference between conditions in this first component in any of the dipoles. This absence of difference is expected as the response from the brain after the first tone should be similar between all conditions.

Then, the source reconstruction on the effect in the early window after the fifth tone was analysed. The results for inversion to the fifth are shown in Table 10

Dipoles	$P_{(1,17)}$
Temp_L	0.67
Temp_R	0.32
Front_L	0.41
Front_R	0.35

Table 9: ECD statistics for the source inversion for the first tone. Each row is related to a prior location, whose name is in the first column and the p-value between both condition is in the second column. For each of the 4 dipoles, the p-value after a t-test between dipole location for conditions RLDGD and RLDGS is not significant.

with the mean location of each dipole. We see that the right frontal dipole is more ventral in the global deviant condition compared to the standard condition. The results of the statistical test between both conditions for each dipole are shown in Table 11.

Dipoles	RLDGS			RLDGD		
	x	y	z	x	y	z
Temp_L	-32.82	-29.14	1.29	-41.53	-31.88	1.12
Temp_R	36.61	-27.42	-1.43	41.39	-37.87	-0.94
Front_L	32.45	1.63	-21.53	38.22	7.56	-22.38
Front_R	-33.05	2.19	-17.28	-36.83	7.66	-23.57

Table 10: Dipole localisation for the early effect, with two different conditions. Each row is related to a dipole location, with name in the first column. Then, the mean location for each dipole is reported in the x, y, and z coordinates for the RLDGS condition and RLDGD condition in the last three columns.

We observe a statistical difference in the mean location. The early window effect generates a difference on two of the dipoles. In particular, the dipoles in the right hemisphere are significant for an alpha level of $\alpha = 0.05$, with a more posterior dipole in temporal for the global standard condition compared to a more anterior dipole for the global deviant.

Finally, the results for inversion to the late window effect are shown in Table 12 for the mean location.

Dipoles	$P_{(1,17)}$
Temp_L	0.063
Temp_R	**0.012**
Front_L	0.432
Front_R	**0.045**

Table 11: ECD statistics for the source inversion in the early window effect. P-Value of the t test between RLDGS and RLDGD conditions, for the early window effect. Each row is related to a prior location, whose name is in the first column and the p-value between both condition is in the second column. Significant values are in bold.

Dipoles	RLDGS			RLDGD		
	x	y	z	x	y	z
Temp_L	-28.4	-25.47	-0.72	-24.29	-43.44	-4.28
Temp_R	29.19	-25.81	-1.80	27.05	-45.34	-4.47
Front_L	20.72	17.33	-13.47	27.84	7.71	-10.31
Front_R	-24.92	-4.99	-11.22	-26.95	17.90	-7.79

Table 12: Source reconstruction dipole localisations for the late window effect. Each row is related to a dipole location named in the first column. Then, the mean location for each dipole is reported in the x, y, and z coordinates for the RLDGS and RLDGD condition.

The results of the statistical test between both conditions are shown in Table 13. There is a significant difference between dipoles for this late window effect. In particular, all dipoles but the left frontal one are significant for an alpha level of $\alpha = 0.05$, with the most significant difference being in the temporal with $p = 0.009$ and $p = 0.001$ for left and right dipole respectively.

Dipoles	$P_{(1,17)}$
Temp_L	**0.009**
Temp_R	**0.001**
Front_L	0.8
Front_R	**0.018**

Table 13: ECD statistics for the source inversion in the late window effect. P-value of the T-test between RLDGS and RLDGD conditions, for the late effect. Each row is related to a prior location named in the first column and the p-value between both condition is in the second column. Significant values are in bold.

The source reconstruction on the late effect is shown in Fig. 35. Blue dipoles shown for the RLDGS condition are located more centrally in the brain. Magenta dipoles for the RLDGD condition are located more posterior on the brain. The most significant dipole locations are respectively temporal right and temporal left.
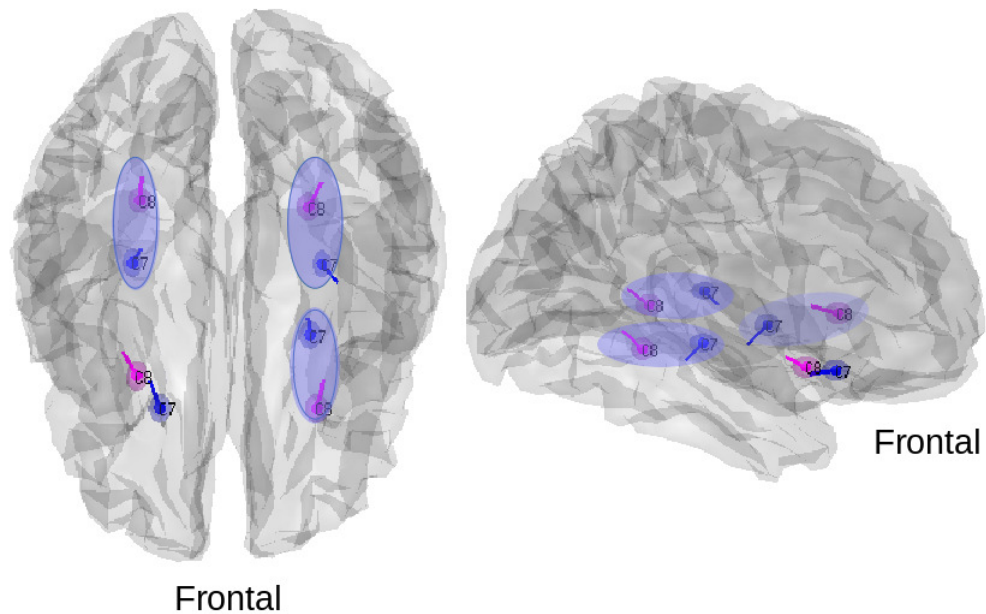
Figure 35: ECD source reconstruction in the late effect. Two perspectives of ECD source reconstruction, with frontal on the bottom for the left view, and on the right on the right view. Both RLDGS and RLDGD inversion are presented, with dipoles in blue for the RLDGS condition, and dipoles in magenta for the RLDGD condition. Dipole locations for temporal left, temporal right and frontal left are significantly different between both condition. These dipoles are highlighted with a blue shade. The frontal right dipole locations are not significantly different.

Conclusion

The source reconstruction for the local-global experiment shown a difference for the late effect in both temporal and frontal dipoles. This was expected as the global effect may involve a broader network. Also, this model of four dipoles may

be weak as it does not include dipoles in parietal lobe which is likely to be involved in the global effect (Dehaene and Changeux 2011). The localisation during the early window is also significant between both conditions for the right hemisphere. This can be related to contingent negativity, as there is an increased of expectation related to the global deviation, which can occur before the fifth tone.

Therefore, in the next section, we performed source localisation analysis using dipoles from different brain regions. Some models involve more brain regions than others. Model comparisons were performed on these models.

4.4.7   Local-Global Model Comparison

In this analysis, we analysed different neuronal models that could explain local deviant and global deviant components. We focussed on the RLDGD condition, being the condition which involve both local and global deviant, to investigate different models for the local deviant on the early window response, and the global deviant on the late window response. Models were defined by a combination of dipoles used for the source reconstruction. They were constructed by including the main brain areas: in frontal with the Inferior Frontal Cortex (IFG), in temporal with the primary auditory cortex (A1) and Superior Temporal Gyrus (STG), and parietal with Superior Parietal (SP) and Dorsolateral Parietal Cortex (DLPC).

For the model comparison, 12 models were included. The first four models consisted of one pair of symmetric dipoles respectively in: Frontal (Fr), Superior Temporal Gyrus (STG), primary auditory cortex (A1), and Parietal (Par). The next models combined two pairs of symmetric dipoles based on the four possible

locations. These are models Fr-STG, Fr-A1, A1-Par, STG-Par, Fr-Par, and STG-A1. Finally, the lasts two models for the local effect are Fr-STG-A1 and STG-A1-Par, to compare the influence of frontal and parietal with the dipoles in temporal (STG-A1).

After source inversion for each dipole model at a group level, the model evidence given by the Free Energy was used for Bayesian model comparison. We selected the most plausible model which had the highest Free Energy. The results for the local deviant condition are displayed in Figs. 36 and 37.
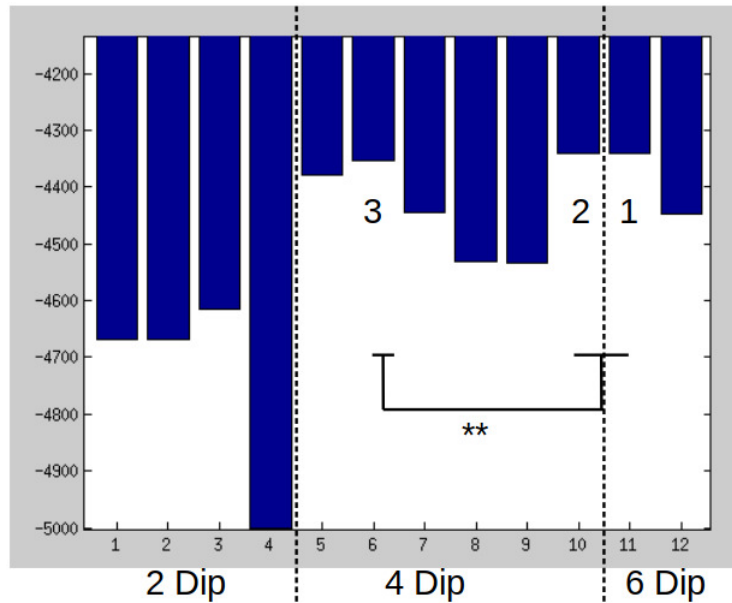
Figure 36: Model selection for local deviant, with 2 dipoles, 4 dipoles and 6 dipoles models. 12 models are compared by their free energy for the local deviant modelling. Models are presented in table 14. The two best models are models 10 and 11. There is no significant difference between these two. There is strong evidence compared with the third-ranked model, i.e. model 6 highlighted by the two stars. Model from 1 to 4 have one pair of dipoles. Models from 5 to 10 have two pairs of dipoles and models 11 and 12 have four pairs of dipoles.

From Table 14, we can see that the worst models are models with only one pair of dipoles, like the first four models. The two models which come first are the

Model number	Dipoles	Group Free-energy	Model ranking
1	Fr	-4669.3	11
2	STG	-4667.7	10
3	A1	-4613.9	9
4	Par	-5002.4	12
5	Fr-STG	-4379.8	4
6	Fr-A1	-4352.1	3
7	A1-Par	-4444.1	5
8	STG-Par	-4530.0	7
9	Fr-Par	-4533.2	8
10	**STG-A1**	-4341.0	1
11	**Fr-STG-A1**	-4341.0	2
12	STG-A1-Par	-4446.4	6

Table 14: Model description and evaluation for the local deviant. The first column is the index regarding the different models. Each model is described in the second column. The third column presents group free energy, and the last column gives the ranking for the local deviant.

models 10 and 11, and they have the same value of Free Energy. Model 10 includes both pairs of dipoles in the temporal lobe, while model 11 adds frontal dipoles. This means that the frontal dipoles do not add more information to make a model for this effect. If only one dipole is used for the temporal lobe, frontal dipoles are better than parietal dipoles (models 6 and 5 ranked respectively three and four, compared to models 7 and 8, ranked five and seven). The model including no dipoles in the temporal lobe (model 9) is better than only one pair of dipole in temporal. This result reflects the necessity of a model with at least a complexity of two pairs of dipoles. Three pairs of dipoles can also reveal the local activity if the third pair is in frontal (model 11), but not if in parietal (model 12).

The models used for the model comparison both for the local effect and the global effect is presented in table 15. The first column is the number of the model. The 'Dipoles' column shows the dipoles included for the model. The third column presents the ranking of the model for the early window effect on the local deviant.

The model with the highest evidence ranks first, and the model with the lowest evidence has the last rank. The fourth column presents the ranking for the late window effect related to the global deviant. One means the highest evidence, and number nine means the lowest model evidence ranking.

From this first model selection, we reduced the number of models. It was shown previously that only one pair of dipoles is not enough to model the local effect. Then, at least two pairs of dipoles were included. The models with two pairs of dipoles are Fr plus A1 (model 1) and STG plus A1 (model 2), as shown in Table 15. Parietal was not included in the two pairs dipoles due to the lack of evidence from the previous analysis in table 14. For models with three pairs of dipoles, they consisted of Fr, STG and A1 (model 3); STG, A1 and parietal (model 4); Fr, STG and Par (model 5). We also included another choice for the parietal cortex by involving the Dorso-Lateral Parietal Cortex (DLPC). We used it for model 6 with Fr, A1 and DLPC. We used two models with four pairs of dipoles. They included Fr, STG, A1 and either DLPC (model 7) or parietal (model 8). Finally, the last model included all of the priors (five pairs of dipoles). The five pairs of dipoles model a higher complexity.

The model selection with these nine models for the local deviant is shown in Fig. 37 and for the global deviant is shown in Fig. 38. We see that the best model for the local effect is both model 2 and model 3. Model 2 involves dipoles in STG and A1, while model 3 also includes frontal dipoles. The worst model for the local effect is the model 4, including STG, A1 and Par. It can be understood due to the parietal dipoles which are unlikely involved in the early processing stages for the local deviant. For the global effect, the best model is model 8, which includes four pairs of dipoles from temporal (STG, A1), Fr and Par. However, a four-location model as the one with DLPC in parietal is not appropriate, as it ranks

111

Model number	Dipoles	Local ranking	Global ranking
1	Fr-A1	4	6
2	STG-A1	**1**	4
3	Fr-STG-A1	2	3
4	STG-A1-Par	9	2
5	Fr-STG-Par	6	7
6	Fr-A1-DLPC	8	8
7	Fr-A1-STG-DLPC	3	5
8	Fr-A1-STG-Par	5	**1**
9	Fr-A1-STG-Par-DLPC	7	9

Table 15: Model description and comparison for local and global deviant condition. First column is the index of the different models. The model is described in the second column. The third column presents the model ranking for the local deviant and the last column presents the ranking for the global deviant.

5. Similarly, an over-complex model with five locations does not fit the data and has the lowest rank (rank nine). The second best model is model 4, with three pairs of dipoles, in STG, A1 and Par.

4.5   Discussion

Equivalent Current Dipole source reconstruction was used to reconstruct the sources from a particular brain pattern. The time chosen for the source inversion should represent a specific event of interest. Once the dataset is known, parameters are needed to create a model. This consists of the number of dipoles used to fit the data, location and orientation priors. After optimisation based on the model, dipole locations can be retrieved and compared between different conditions. The Free Energy of the model (model evidence) can also be used for Bayesian model comparison. By using the ECD method, we have been through these different steps:

- Sanity check
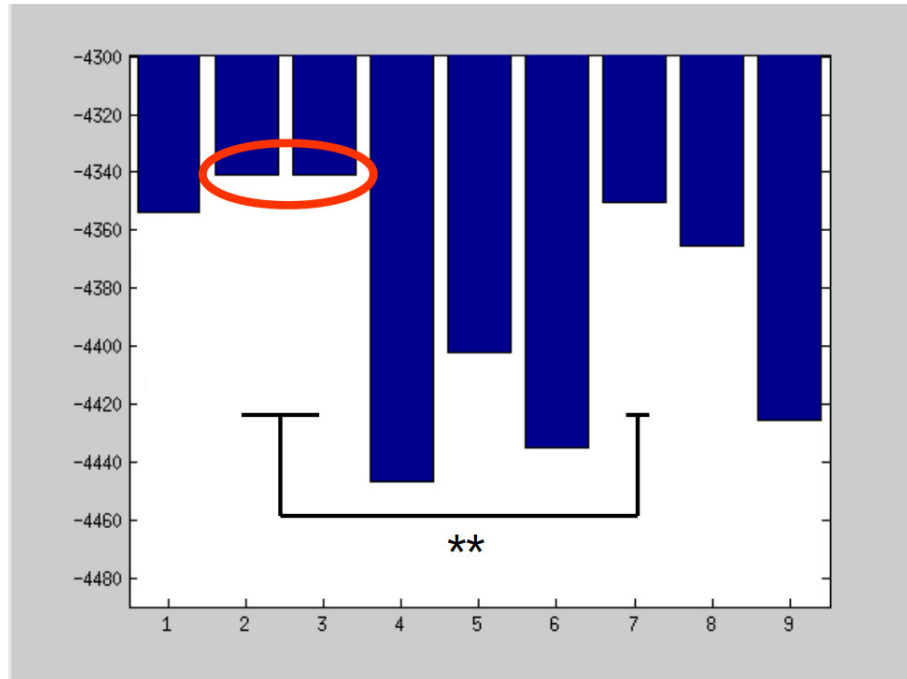
Figure 37: Model selection for the local deviant with 9 models. Nine models are compared by their free energy for the local deviant modelling. Models are presented in table 15. The two best models are highlighted with the red ellipse i.e. models 2 and 3. There is no significant different between these two, but a strong evidence compared with the next model i.e. model 7, as highlighted with the two stars.

The stability of source localisation on auditory stimulus has been evaluated. By varying the position of the prior and comparing the final location, we have shown good stability at a group level relative to the 'ground truth'.

- Dipole location and statistical comparison

The location of dipoles has been compared between two conditions. They reveal significant statistical differences. No location difference is found in the first tone. The late effect, however, shows a strong difference between global deviant and global standard. With priors in temporal and frontal, the most significant difference is in the temporal sources; left frontal dipole is also significant between both conditions. There is also a difference between

113
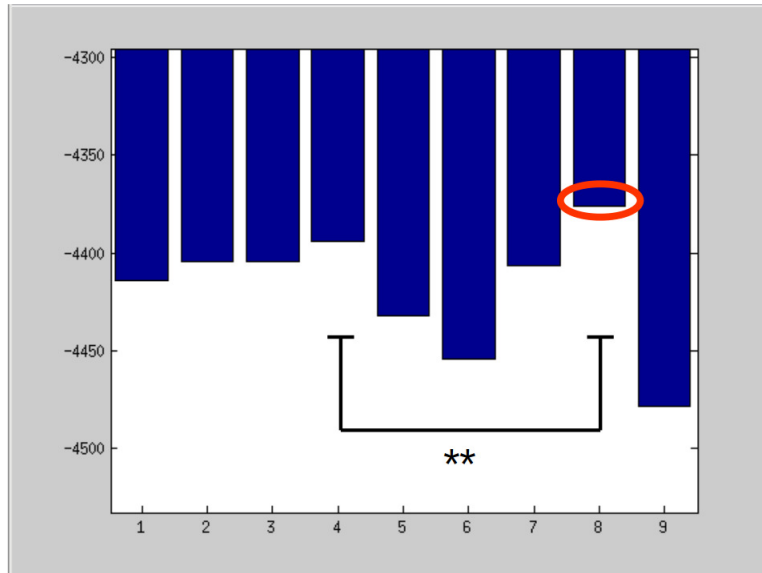
Figure 38: Model selection for the global deviant with nine models. Nine models are compared by their free energy for the global deviant modelling. Models are presented in Table 15. The best model is highlighted with the red ellipse i.e. model 8. There is a strong evidence of model 8 compared with the next model 4, as shown with the two stars.

global deviant and standard in the early response after the fifth tone, which

may be due to the contingent negativity.

- Model comparison on synthetic data

  Beyond the anatomical location, Free energy of the inversion (model evidence), can be used as model comparison using the Bayes factor. On synthetic dataset, we have shown how the model comparison can be applied to one pair of dipoles modelling two different locations. Bayes factor has been used to select the most plausible model, related to a synthetic scalp-map.

- Finally, a model comparison has been applied to the local-global experiment. This shows a simpler model for the local effect composed of temporal dipoles, while the global effect is best modelised by a more complex model which covers frontal, temporal and parietal brain area. This large network during

114

access to consciousness confirms the global workspace theory from Dehaene and Changeux (2011).

This ECD method is particularly well adapted for a simple experimental design and a neuronal model which include few dipoles. However, ECD methods have some drawbacks. It is well adapted only for a few numbers of dipoles. With ten dipoles included in a model, the computational power required for the optimisation algorithm to converge took time. For these analyses, it was used an HPC to run the different models. A description of HPC computation applied to ECD inversion is provided in Appendix B. Finally, this source inversion is hypothesis-driven, and a good selection of the models included for the source reconstruction is required. However, other hypotheses may be more adapted for the model comparison. By using imaging methods, a more flexible solution is proposed in the next chapter.

Chapter 5

Local-Global with Sedation - MSP Inverse Reconstruction

5.1   Chapter Outline

This chapter presents a source level analysis on the local-global experiment with sedation. Using the local-global experimental design, we applied Multiple Spare Prior (MSP) imaging inversion to find the sources involved during different time windows. A description of the methods for sources inversion and statistical analysis was presented. We then showed the results of the source localisation and particularly the fronto-temporal clusters in the local by global interaction during the middle window which is part of a three-phase theory of the local-global. A three-way interaction is significant with a frontal cluster highlighting the role of the inferior frontal cortex during sedation. Finally, we discuss these results.

5.2 Introduction

A general overview of consciousness was given in Fig. 1 following a 2-dimensional map of levels of awareness and wakefulness. Theoretically, different views on consciousness need to be assessed by models which can explain the manifestation of consciousness. From a practical point of view, a better understanding of mechanisms of consciousness will be useful to implement treatment or diagnosis tools for impaired consciousness. One practical example is related to anaesthesia. This medical procedure applied before a surgical operation is needed to let the patient be unconscious during surgical. However, many cases occur when the patient is still aware or partially aware of the environment after anaesthesia. Increasing the robustness of this procedure is of particular importance to physicists for the safety of the patients.

To solve this issue, a better understanding of consciousness and the availability to distinguish between conscious and unconscious state is necessary. One recent model of perception is the predictive coding, which is based on Prediction Error (PE) (Rao and Ballard 1999). The prediction error is related to the difference between the data (i.e. environment) observed from our sensory input (e.g. visual, auditive etc.), and the prediction made by our internal state as a representation of the world. This internal representation is based on past experiences and expectation of coming events (Friston 2010). In particular, two pathways are competing with each other: bottom-up and top-down. The first one refers to the sensory input and the backward neural activity which is going to generate a perception related to the input. The second signal is the feed-forward neural activity which is an expectation or prediction of the incoming sensory input. Different hierarchical levels in the brain are propagating these two pathways, and the interaction

between both of them at a particular level create an internal loop of prediction error (Friston 2010).

One basic example where predictive coding can apply is for sounds irregularities. When a pattern of sounds is presented to a subject, then brain establish an internal representation of the stimuli from a learning procedure or habituation. However, if an irregularity appears in the stream of stimuli, this generates a mismatch between the expected pattern coming from the internal representation and the incoming auditory stimulus. Different mismatches, from mismatch negativity or P300 occur, depending on the experimental manipulation. On the other hand, Global Workspace Theory (Dehaene and Changeux 2011) proposed an activation of long range connection which give rise to consciousness on a late and more stable time window.

A two-levels of hierarchical auditory paradigm have been devised (Bekinschtein et al. 2009), which embeds both a response to a local irregularity and a late response to a global irregularity. These effects of local-global paradigm have been explored in the literature, and it has been proposed that these two effects come from two distinct components. A first component is related to the local effect which is not affected by a change in consciousness, and a second component, the global effect, is more specifically related to conscious processing. This difference reflects organization in the brain to process information. This is not only related to time-scale, but occurs also with other patterns. However, little has been done to study the interaction between both local and global levels. In this study, we were particularly interested in this interaction. Moreover, we used a local-global experiment with a third effect due to sedation. The subject was induced moderate sedation before being exposed to the local-global paradigm twice: during sedation and again once recovered.

A previous analysis had been published from this experiment with analysis at the scalp level (Shirazi-Beheshti et al. 2018). In this paper we have explored the sharpness of the transition between local and global temporally and functionally. Here we will explore the sharpness of this transition neuro-physiologically. That is, we are asking the following question. Can we in respect of brain areas, observe a progression from a localised prediction hierarchy to a brain-scale meta-stable state? Furthermore, can we source localise the transition between these two, which we tentatively propose is an additional intermediate phase? A further key question is the role of awareness in this hierarchy. In particular, as Dehaene et al. would argue, is it only the late, global workspace brain circuits that correspond to states of awareness (Dehaene and Changeux 2011)?

To answer these questions, we present a Multiple Sparse Priors (Friston et al. 2008) source localisation of the local-global task. This imaging source inversion method allow us to get more than a few dipoles. This will enable us to characterise the neurophysiological trajectory of brain activation as it propagates from rapidly changing responses restricted to sensory areas (for us in auditory cortices) to slowly changing (meta-stable) broadly dispersed responses (involving temporal, frontal and parietal areas). In this respect, our key finding will be that the transition between these two modes, (1) sensory-bound to (2) brain-scale, involves a transiently engaged superior temporal inferior frontal network. Furthermore, the interaction between local and global encapsulated in this network is modulated by propofol sedation.

5.3 Method

The source inversion takes place in three steps:

- A co-registration step which maps the sensors coordinates to the source space coordinates.

- A forward model for the transformation matrix (Leadfield) from dipole activity to scalp activity.

- The inverse transformation which optimizes the solution at the source level to fit the scalp activity.

Co-registration between the scalp level and the source level in MRI space was applied. Coordinates at the scalp level come from a standard GSN-Hydrocel template with 128 channels. Three fiducials are used to map the coordinates from the scalp-level to the source-level: nasion, left peri-auricular point and right peri-auricular point. As no MRI scans were recorded for the participants, a template head model based on the MNI brain was applied with a cortical template mesh of 8196 dipoles, which describes all the coordinates of the dipoles. Due to the lack of MRI scans, inaccuracies may occur during the source inversion. As a result, we constrained the cortical mesh by selecting only the cortical areas that are most likely to be involved in the experiment, i.e. regions of the temporal, frontal and parietal lobes were included for source reconstruction. Fig. 39 shows the cortical mesh, and supporting text in the Appendix C) give a priori justification for this choice. We did not select for sources deep in the brain, which cannot be accurately reconstructed, as well as the occipital and motor cortices as we are not aware of any prior evidence suggesting these regions are related to the effects of interest in the present study.

The forward model uses the physical properties of the brain to map the dipole activity to the scalp activity at the sensor level. It was computed using the BEM (Boundary Element Method) option as suggested in SPM 12 (Friston 2007) for
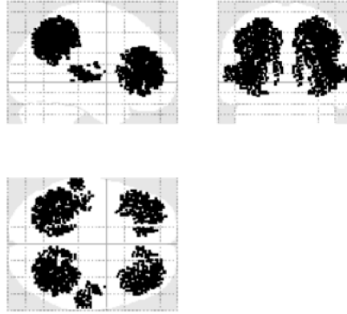
Figure 39: Cortical mesh with dipoles used for source inversion. Sub-cortical mesh which constrained dipole locations (each black dot is a dipole) for the source reconstruction. Regions of the temporal (both primary auditory cortex and superior temporal gyrus), frontal and parietal lobes were included for source reconstruction.

EEG-based source localisation analysis, with a three layer head model, i.e. skin, skull and brain.

5.3.1   Imaging Method

A general framework based on Bayes theory has been developed during the last years using Bayesian method (Baillet and Garnero 1997; Lopez et al. 2014), to find the most appropriate solution based on prior assumption from brain properties. The inverse model performs an optimisation to find the best solution, which explains the activity at the scalp level. By the imaging method, location and orientation of the dipoles are fixed on a brain mesh and the solution can be solved linearly. The source reconstruction can be described by the following equation (Baillet and Garnero 1997):

$$Y = L \cdot A + \epsilon \tag{18}$$

where, $Y \in \Re^{[N,T]}$ being the signal recorded at the scalp level, with $c = 1, ..., N$ being the number of channels and the time series t ranging from 1 to T samples. At the sources level, a mesh based on an MRI template is used to simulate the d dipoles activities in the brain. The $L \in \Re^{[N,d]}$ term is the lead-field matrix applied to all participants. Matrix $A \in \Re^{[d,T]}$ represents the activity at the source level, and works under the assumption that the activity is represented by a zero mean Gaussian process with covariance matrix: $Cov(A) = Q_d$. Lastly, ϵ is the Gaussian noise at the sensor level, which is assumed to have a mean of zero and covariance matrix $Cov(\epsilon) = Q_\epsilon$. The source estimation $\widehat{A}$ calculates the activity at the source level by: $\widehat{A} = E[P(A|Y)]$, and can be described in a Bayesian framework. The posterior probability for the activity matrix A conditioned on the data Y is given by Bayes theorem:

$$P(A|Y) = \frac{P(Y|A) \cdot P(A)}{P(Y)} \tag{19}$$

Where $P(Y|A)$ is the conditional probability for the data given the source activity, and $P(A)$ the prior distribution reflecting our prior expectations about the sources. Because Y is the observed EEG data, the evidence $P(Y)$ is known and constant, giving us:

$$P(A|Y) \propto P(Y|A) \cdot P(A) \tag{20}$$

In these conditions, the source activation is optimised by maximising the posterior probability. This is the same as finding the source activity where the gradient of $log(P(A|Y))$ is 0 (Lopez et al. 2014). Finding a good solution of the source activity is equivalent to finding the best estimates of the covariances matrices Q_ϵ

and Q_d (Dale and Sereno 1993). The source estimation was given as

$$\widehat{A} = Q_d L^T (Q_\epsilon + L^T Q_d L)^{-1} Y \tag{21}$$

The noise covariance matrix Q_ϵ is due to the EEG recordings, and is defined by: $Q_\epsilon = h_0 \cdot I_N$, with I_N being the identity matrix for N sensors and variance h_0, which is the same for all sensors. This can be adapted, for example by using an empty room recording to describe the ambient noise and having a more accurate noise sensor variance. The covariance matrix Q_d is related to properties of the brain. For minimum norm, it can be expressed as $Q_d = h_1 \cdot I_d$, where h_1 is the dipoles noise variance, and I_d the identity matrix for d dipoles. Accordingly minimum norm recovers a source distribution with minimum overall energy, without spatially prior information. This results in source activity that is scattered broadly abroad the brain, where the activity took place.

The Multiple Sparse Prior (MSP) method developed recently (Friston et al. 2008; Lopez et al. 2014), enables the covariance matrix to be defined as a weighted sum of prior components: $Qd = \sum_{i=1}^{q}(h_i \cdot C_i)$, where hyper-parameters h_i weight the covariance components C_i. Singular value decomposition is used to facilitate the algebraical solution of the equation. In particular, the source covariances are projected into the sensor space which reduces the dimensionality of the data to optimize.

To find the optimum solution for Q_d, minimising of Free Energy is used as the objective function, and optimised with a Variational Laplace scheme, as a generalization of Expectation-Maximisation (Friston et al. 2007). Briefly, given a chosen parameter values, the EM calculates the probability that each point of the dataset belongs to a particular distribution and then use these probabilities

to compute a new estimate for the parameters (which maximize the likelihood). This loop continues until the estimates of the parameters stabilize or change very little. In particular, this algorithm use the following steps:

- Select initial set of parameters for the distributions.

- **repeat**

- **Expectation Step** For each point of the data, calculate the probability that the point belongs to the distributions.

- **Maximization Step** Given the probabilities from the expectation step, find the new estimates of the parameters that maximize the expected likelihood.

- **until** The parameters are stable. (Alternatively, stop if the change in the parameters is below a specified threshold.)

The optimal combination of the hyper-parameters h_i is achieved for the maximum negative Free Energy value, where: $h_i = argmax(-F)$, where the Free Energy approximate the log evidence. To find the optimum solution, a Variational Free Energy calculation is used as an objective (or cost) function, and optimised with a Variational Laplace scheme (Friston et al. 2007). The iterating algorithm loops until the Variational Free Energy stay stabilise: $\Delta F < 0.01$, see Friston et al. (2007) for details of the algorithm. Finally, the temporal response in source space was evaluated using the temporal projector created during the data reduction step.

5.3.2 EEG source reconstruction

All analyses are focussed on the evoked transient set up by the fifth tone in a quintuple for the data described in Section 4.4.1. Trials were baseline corrected

with a baseline 200ms before the onset of the fifth tone, which occurred between 400ms to 600ms from trial (i.e. 1st tone) onset. With this configuration, we are not interested by activation of the sources for the 4 first tones but instead focus on the effect of the 5th tone depending of the conditions. The time segment used for inversion was -200ms (from fifth tone) to the end of the trial at 696ms from fifth tone onset. A group inversion was performed to minimize the variance between participants using the Bayesian inversion scheme within SPM that applies Multiple Sparse Priors (MSP) (Litvak and Friston 2008). We select a time-frequency window for the source reconstruction. The frequency band used is similar to the one applied for the pre-processing with a frequency band of $[0.5 \ 20] \ Hz$. After inversion, three windows of interest were selected as explained in the next section to study the sources involved in activity after the fifth tone. For each window, images were extracted for each condition and participant. The General Linear Model (GLM) was used to explore significant sources for different effects. The maps at the source level were corrected for multiple comparisons using Random Field Theory.

5.3.3 Windows placement for images extraction

After source inversion, two more analyses were performed in order to gain insight into the spatial and temporal activity of the brain. The first was the image extraction to spatially summarise the brain activity in three dimensional images. This format allows standard second-level SPM fMRI statistical analysis. The second analysis was to explore temporal activity by selecting a Region Of Interest (ROI) and extracting the time-series at the source level. The source location for the ROI came from the results of statistical inference as explained below.

The image extraction summarizes the activity on the mesh, across the segment of time chosen. The power of the brain activity was averaged across time for the frequency range [0.5 20] Hz. A spatial filter was used to smooth the dipole activity on the three dimensional source space.

To obtain such three dimensional maps from the four dimensions – three of space and one of time – generated by the MSP algorithm, windows in time were placed and collapsed across, by calculating the root mean squared across the window. Statistical inference in this context, then, required the placement of windows in time. Tailoring such windows post-hoc to the landmarks of M/EEG data, will inflate false positive rates (e.g. (Brooks, Zoumpoulaki and Bowman 2017)). The prior precedents for these placements were taken from Bekinschtein et al. (2009), which used the same experimental paradigm, but with analysis applied on a different dataset. Specifically, we looked at the following three effects, with time relative to 5th tone onset.

- Early window [100, 150] ms: to consider the local effect, ie. the mismatch negativity;

- Middle window [250, 350] ms: to see the interaction between the local and global effects, which is most likely to occur when both local and global effects are present;

- Late window [400, 600] ms: to observe the global effect, which manifests as a P3b.

We document here how we have arrived at our window placements, the prior precedents for which are taken from Bekinschtein et al. (2009), the article that introduced the local-global effect. We identified relevant scalp maps in Bekinschtein
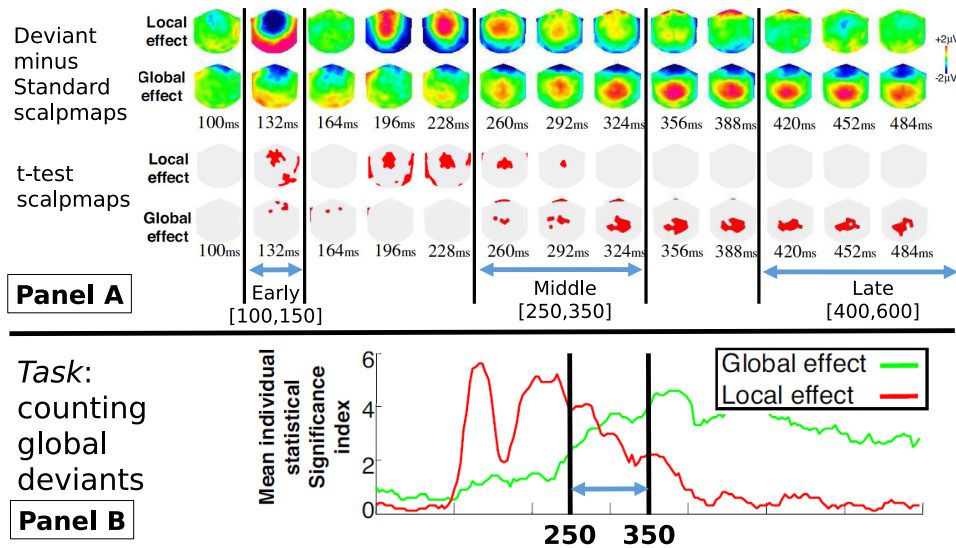
Figure 40: Window placement. Figures from Bekinschtein et al. (2009), reproduced here to explain the window placements and the prior precedents for them. Panel A is the top part of figure 2 from Bekinschtein et al. (2009), which shows the basic local and global effects observed. Panel B is part of figure 4 from Bekinschtein et al. (2009): it is a counting global deviants condition, which is the task performed in our experiment. The windows we have selected are shown with light blue double arrows.

et al. (2009), Fig.2 (see our Fig. 40, panel A), and placed windows between relevant and the first adjacent non-relevant scalp maps. As shown in Fig. 40, our local effect window starts at the beginning and finishes at the end of the local effect scalp map in Bekinschtein et al. (2009).

The middle window was selected as the largest period in which both local and global effects are present. This is because investigating the local x global interaction in the P3a region was an a priori assumption, mandating a region in which both local and global effects are present. The middle window extends out beyond the 324 ms scalp map. This is because figure 4, top-row, right hand panel of (Bekinschtein et al. 2009), which is reproduced in Fig. 40 (panel B), shows that the local effect remains substantial (and the global effect even more so) out to the

350 ms region marked in our Fig. 40 (panel B).

Our late window had been selected to be sufficiently far from the middle window that we investigate a distinct region of the time series. However, we kept the gap between middle and late windows relatively small (50 ms), since, as evident in (Bekinschtein et al. 2009) (reproduced in Fig. 40), the P3b may be waning in size from around 400 ms. We selected a relatively long late window, since there is considerable prior precedent for an extended P3b; see, for example, (King et al. 2014) and panel B of our Fig. 40.

5.3.4 Statistical analysis

Spatial activity

For each subject (18) and each condition (8), three images (one for each window, extracted from MSP source reconstruction algorithm) were used to be processed by the General Linear Model (GLM) for statistical analysis. A total of 144 scans per window were used for the statistics. The experimental design can be summarized as a 2x2x2 within-subjects design, with 3 factors: sedation, local, and global effects. Each factor is composed of 2 levels: sedation and recovery (for sedation); local standard (LS) and local deviant (LD) (for local); and global standard (GS) and global deviant (GD) (for global). The statistical analysis can be summarized as follows.

The first concern was to understand the relationship between local and global manipulations. To do so, we first looked at the local effect and the global effect individually and then the local x global interaction was studied. Since localisation of the local and global effects has been extensively explored and is well documented in the literature, our analyses of these two effects serve as sanity checks of our

source localisation. That is, if the MSP algorithm localises these to the expected brain areas, we can have confidence that the algorithm will correctly localise the effects for which we have less precedents.

The second is to understand the sedation effect, the sedation x local interaction and the sedation x global interaction; and the last is to analyse the three way interaction between sedation, local and global. We conducted a flexible ANOVA analysis, which employs a two-step threshold to control for multiple comparisons (Friston 2007). The first level cluster-forming threshold used an alpha level of 0.001 to define which voxels are treated as statistically significant. The voxels that cross this threshold form clusters, i.e. 3D regions of continuous significance. Secondly Random Field Theory was used to determine the likelihood that a cluster of significant neighbouring voxels of a particular size will arise, under the (null) assumption that the data is Gaussian noise with a particular smoothness. The second level significance threshold which for us was an alpha level of 0.05, was then applied on cluster extents, providing a Family Wise Error corrected significance. Seven contrasts were applied to the data to perform the three analyses outlined above. F-contrast thresholds corresponding to the cluster forming alpha-level were computed and applied at each voxel as the result of the analysis contrast. The significant clusters after subjection to the family-wise error correction just discussed can be visualized on a 3D brain.

A list of contrasts was applied to explore the effects of the different conditions and interactions of the experimental design. Seven contrasts are analysed in this study, related to the three goals we planned above. These effects are: local effect, global effect, local by global interaction, sedation effect, sedation by local, sedation by global and sedation by local by global. For example, for the sedation effect, the contrast vector is [-1 -1 -1 -1 1 1 1 1], where all the sedation conditions are set

to minus one and all the recovery conditions are set to plus one, to differentiate between the Beta images of the two groups. For an interaction effect, E.g. local by global, a difference of differences is computed to find the interaction: (LDGD-LDGS)-(LSGD-LSGS). The first pair of brackets gives the global effect for the locally deviant conditions. The second pair of brackets gives the global effect for the locally standard conditions. Both pairs are subtracted to compute the interaction. It applies equally for sedation and recover conditions, which gives a contrast vector of: [1 -1 -1 1 1 -1 -1 1]. The same applies for the three way interaction.

Temporal activity analysis

The source analysis reveals which cortical areas are significantly related to the different effects of interest (as highlighted previously), within the different time windows. We also investigated how the temporal activity changes at the source level, by the following steps. The location in each brain region selected to plot the source time-series was taken from the peak of the significant cluster, during the middle window [250, 350] ms. Specifically, we selected the temporal lobe sources located at the peak of the cluster for the local effect, the frontal lobe sources located at the peak of the cluster in the local x global interaction, and the parietal sources located at the peak of the cluster for the global effect.

The sources were then extracted within a ROI of 5 mm and the corresponding time-series for these sources were exported for each subject and each condition. Only the left hemisphere time-series are presented for illustration, the time course for the right hemisphere is though similar. The 3D brain images generated by SPM correspond to the average of the time-series for each window, namely, the early window [700 750] ms, the middle window [850 950] ms and the late window

[1000 1200] ms. We therefore performed signal processing on the times-series data for the underlying sources to aid comparison for the 3D brain images. There are a number of steps performed to achieve this goal. For each sample in the time-series, a hamming window was used to convolve with the power of the time-series. As the size of the early, middle and late windows are different, it is not possible to apply a fixed-size window. We therefore needed to develop a mechanism to incorporate the following two transition periods: 1) transition between early and middle window, 2) transition between the middle and the late window. The width of the hamming window was computed relative to the position of the sample. All the points up to the end of the early window employed a hamming window width of 50 ms. The length of the hamming window increased linearly from 50 to 100 ms up to the beginning of the middle window to deal with the first transition period. Then, the window size remained the same until the end middle window. To deal with the second transition period, the size of the hamming window again increased linearly from 100ms to 200 ms until the beginning of the late window. From the beginning of the late window onward, the hamming window length was 200 ms. Finally, the square root mean was applied on the source time-series transformed by the hamming window. To deal with edge effects, the data were mirrored at the begin and the end of the epoch.

5.4   Results

In this section, the results of the local effect, the global effect, the local by global interaction and the three way interactions are presented. Note that, since power is taken from MSP output before statistical inference is performed, all the condition time-series we present here are positive, i.e. show power amplitude.

5.4.1 Local effect
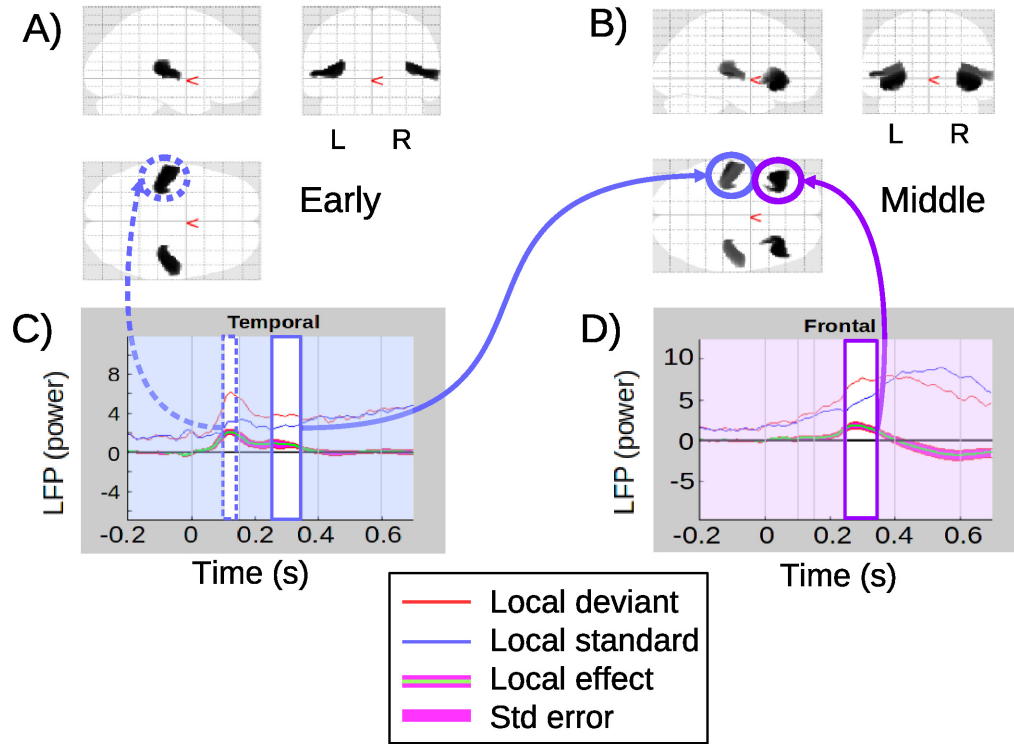
Figure 41: Local effect. A,B) present the SPM results with the significant clusters in a 3D brain image for the early (A) and middle (B) windows. C,D) The source time-series are plotted for the clusters at the temporal (C) and frontal (D) lobes. Zero is the onset of the (critical) fifth tone, a baseline of 200ms was used prior to zero. The times-series are summarized across subjects and shown in red and blue for local deviant and local standard conditions respectively. The local effect between the two conditions is plotted in green, and the standard error in magenta.

The local effect (green line) is found significant at the temporal sources during both the early and middle windows, as shown in Fig. 41A) and B). The time course for the temporal area is shown in Fig. 41C) where the MMN appears clearly with a peak in the early window (dashed blue arrow). The local effect is again significant in the temporal region during the middle window (solid blue arrow), whereas it is not significant in the late window. Fig. 41B) shows that frontal clusters are

also significant in the middle window. This is shown by the time course of the frontal cluster in Fig. 41D), with a peak during the middle window. A reversal of the local effect (green line) is present during the late window but not significant. Table 16 summarizes the statistical results for each cluster in the early and middle windows. For each cluster, the peak location is described in the first column as well as the uncorrected F-statistics for the peak cluster in the third column. Then the family wise error corrected P-value is presented with the size of the cluster. This shows a strong effect ($P_{FWE} < 0.001$) for all the clusters shown in the table.

Clusters	Peak location	$F_{(unc.)}(1,119)$	$P_{(unc.)}$	$P_{(FWE)}$	K cluster size
Early window					
Left temporal	(-58,-24,4)	15.24	<1e-3	<1e-3	383
Right temporal	(52,-24,4)	15.14	<1e-3	0.001	312
Middle window					
Left temporal	(-58, -24, 4)	21.02	<1e-3	<1e-3	491
Right temporal	(42, -20, 8)	18.9	<1e-3	<1e-3	365
Left frontal	(-46, 20, -10)	22.65	<1e-3	<1e-3	591
Right frontal	(-44, 22, -12)	22.59	<1e-3	<1e-3	584

Table 16: Local effect statistics. Statistics for each cluster for the early and middle windows. Each cluster, named in the first column, is characterized by its peak location in MNI coordinates as shown in the second column, the F-value (third column), the p-value (fourth and fifth column) and the cluster size (last column). The first p-value is the uncorrected value at the voxel level of the peak location. The second p-value refers to the p-value for the cluster after family-wise error correction, set to 0.05.

5.4.2 Global effect

The global effect is presented in Fig. 42. In the early window, the global effect is significant at both left and right frontal sources, as shown in Fig. 42C). This early global effect can be related to the contingent negative variation (CNV) (Chennu et al. 2013). Indeed, the time course for the frontal area in Fig. 42F) shows
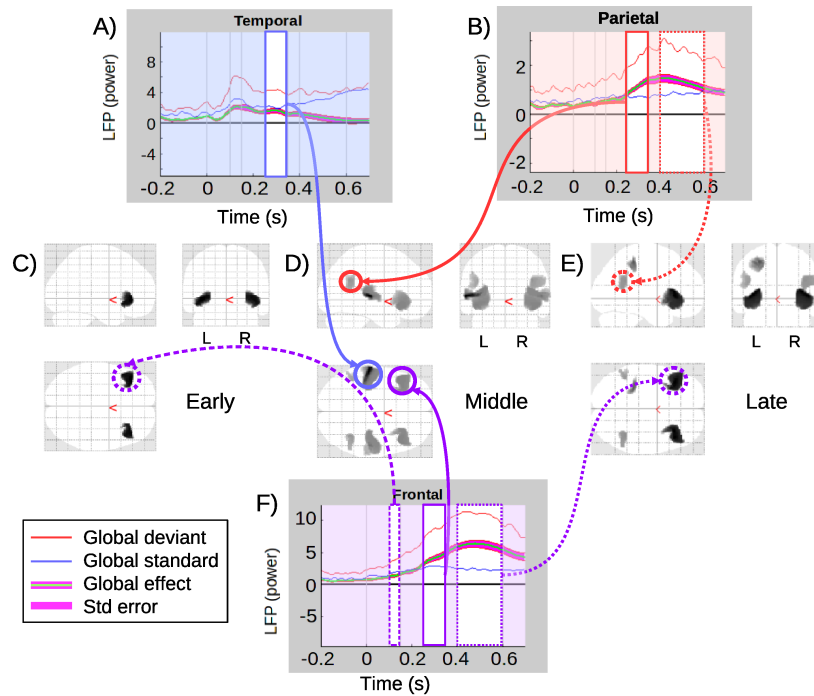
Figure 42: Global effect. A) Source time-series corresponding to the temporal lobe cluster, with significant effect in the middle window; B) Source time-series corresponding to the parietal cluster, with significant cluster in middle and late windows. C,D,E) 3D brain images with significant clusters in early, middle and late window. F) Source time-series at the frontal cluster for all three windows. Zero is the onset of the (critical) fifth tone.

that the global deviant is above the global standard before and during the early window. During the baseline, a small global effect (before the onset of the fifth tone) is also representative of this CNV effect as an anticipation of the global deviant quintuple.

During the middle window, as shown in Fig. 42D), the global effect is significant in the temporal, parietal and frontal regions with the time course represented respectively in Fig. 42A), Fig. 42B) and Fig. 42F). This window involves a complex network of brain activity indicated by the significant clusters. Fig. 42A) shows the time course in the temporal area. The global deviant diverges from global

standard, but is significant only during the middle window, before disappearing in the late window.

In the late window, Fig. 42E), the global effect is significant in a network comprising both frontal and parietal regions. The time course for the parietal cluster is plotted in Fig. 42B), which shows the global effect is significant during the middle and late window with a peak at the beginning of the late window. Additionally, specifically on the left side, a second more dorsal parietal cluster appears, which was not present in the middle window. Finally, Fig. 42F) shows the frontal time course of the global effect is significant in all three windows with a peak in the middle of the late window. This frontal area is the most activated for the global effect, starting from the CNV, until achieving the strongest effect during the late window.

The statistical results from SPM for each significant cluster are shown on Table 17 below. The clusters in the early window have p-value after FWE of approximately 0.01, while the strongest effects appear during the middle window, with p-value after FWE below 0.001 for all clusters.

5.4.3 Local by global interaction

The local by global interaction is significant only in the middle window, as shown in Fig. 43B). The left temporal time course is shown in Fig. 43A), with a small not significant increase in the interaction effect (green line), which peaks after the early window, this is followed by a significant ($P_{FWE} = 0.003$) second increase that is in the middle window. Stronger clusters are in the frontal area. Fig. 43C) shows the time course for the left frontal cluster. The interaction is significant for the middle window ($P_{FWE} = 0.009$), with a positive interaction before a reversal of the effect

Clusters	Peak location	$F_{(unc.)}(1,119)$	$P_{(unc.)}$	$P_{(FWE)}$	K cluster size
Early window					
Left temporal	(-58,-24,4)	15.24	<1e-3	<1e-3	383
Left frontal	(-40, 32, -4)	18.05	<1e-3	0.01	177
Right frontal	(44, 26, -6)	17.77	<1e-3	0.013	165
Middle window					
Left temporal	(-60, -24, 4)	53.88	<1e-3	<1e-3	682
Right temporal	(52, -24, 4)	31.28	<1e-3	<1e-3	561
Left frontal	(-46, -20, 10)	28.54	<1e-3	<1e-3	669
Right frontal	(44,22,-12)	28.21	<1e-3	<1e-3	651
Left parietal	(-44, -50, 26)	22.62	<1e-3	<1e-3	126
Right parietal	(38,-54,26)	24.92	<1e-3	<1e-3	265
Late window					
Left frontal	(-36, 26, 4)	37.5	<1e-3	<1e-3	847
Right frontal	(44, 26, 2)	38.32	<1e-3	<1e-3	822
Right parietal	(40, -50, 24)	20.37	<1e-3	0.003	281
Left parietal 1)	(-28, -38, 52)	27.51	<1e-3	0.033	158
Left parietal 2)	(-46, -50, 22)	19.44	<1e-3	0.048	140

Table 17: Global effect statistics. Statistics for each cluster for the early, middle and late windows. Each cluster, named in the first column, is characterized by its peak location in MNI coordinates, as shown in the second column, the F-value of the peak (third column), the p-value (fourth and fifth column) and the cluster size (last column). The first p-values is the uncorrected value at the voxel level of the peak location. The second p-values is for the entire cluster after family-wise error correction, set to 0.05.

(green line) in the late window, which does not reach significance. The details of the statistical results from SPM are presented in Table 18. This interaction in the middle window suggests that a fronto-temporal network is responsible for linking the local and global effects, and that these two effects (local and global) are not independent.
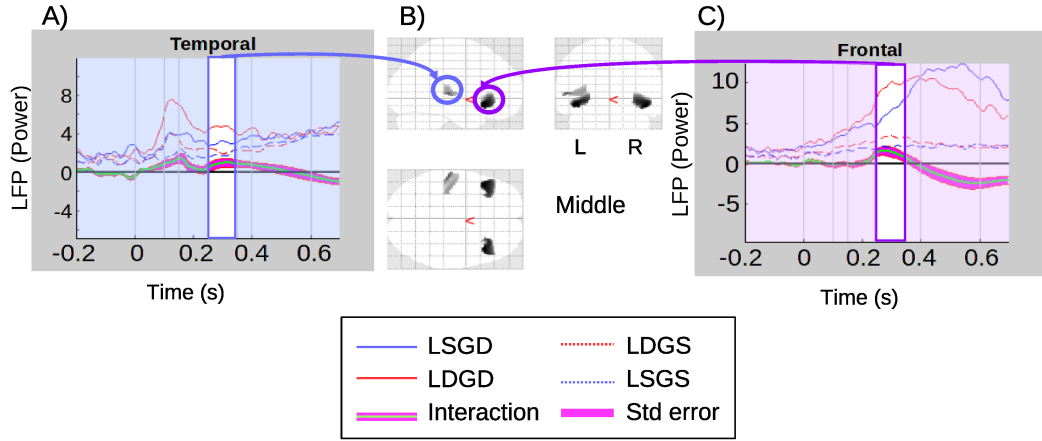
Figure 43: Local by global interaction. A) Source time-series at the temporal cluster, which is significant in the middle window, B) glass brain of significant clusters for the middle window; C) source time-series at the frontal cluster, which is significant in the middle window. Zero is the onset of the (critical) fifth tone.

Clusters	Peak location	$F_{(unc.)}(1,119)$	$P_{(unc.)}$	$P_{(FWE)}$	K cluster size
		Middle window			
Left frontal	(-46, 20, -10)	13.11	<1e-3	0.003	244
Right frontal	(44, 22, -12)	13.02	<1e-3	0.003	234
Left temporal	(-46, 20, -10)	12.45	<1e-3	0.009	186

Table 18: Local by global statistics. Statistics for each cluster for the middle windows. Each cluster, named in the first column, is characterized by its peak location in MNI coordinates as shown in the second column, the F-value at the peak (third column), the p-value (fourth and fifth column) and the cluster size (last column). The first p-value is the uncorrected value at the voxel level of the peak location. The second p-value is for the cluster after family-wise error correction, set to 0.05.

5.4.4 Three way interaction

Finally, the time-series for all conditions and three-way interaction (local by global by sedation) with its standard error is shown in Fig. 44A). The three way interaction is significant in the late window, with its corresponding significant clusters in the frontal lobe shown in Fig. 44D). To identify the causes of the three way interaction, we explored the two simple effects interactions that constitute it.

Specifically, the local by global interaction is presented separately for sedation and recovery in Fig. 44B) and Fig. 44C) respectively. Notably, the local by global interaction was significant in the late window when participants had recovered, but not when they were sedated. Indeed, the local by global effect (green line) had opposite polarities when sedated and recovered for much of the late window. This difference between sedated and recovered seems to be carried by two properties. Firstly, the LDGD condition terminates more sharply when recovered, and secondly, the LSGD condition has a dramatically higher amplitude when recovered. The former of these is exactly consistent with the deceleration of the accelerated
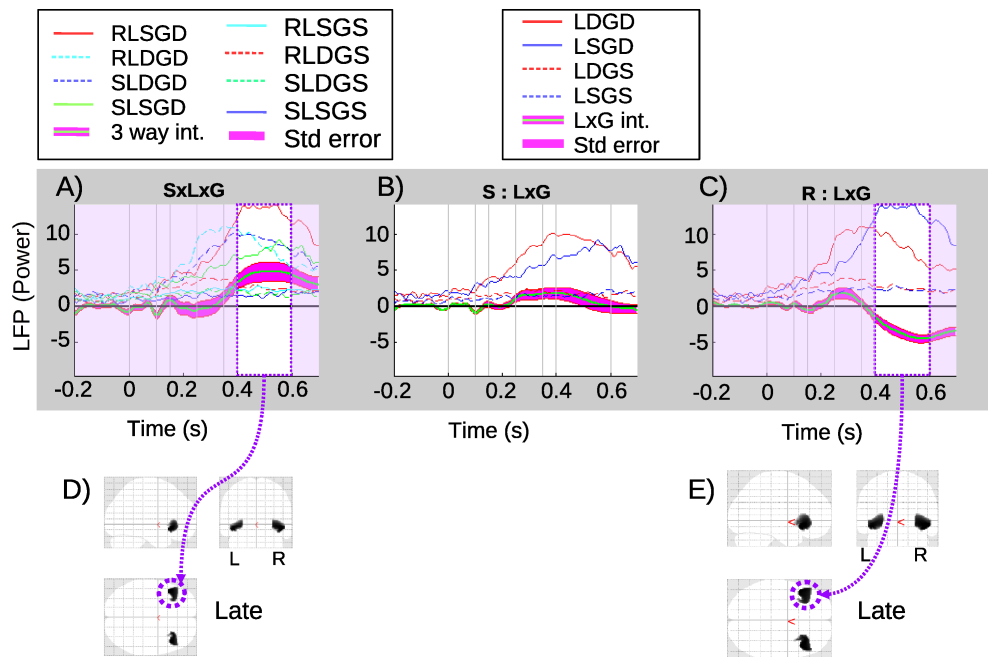
Figure 44: Three way interaction. A) Source time-series for the frontal left cluster of the three -way interaction and the height conditions involved. B) Local by global interaction source time-series for the sedation condition in frontal cluster. C) local by global interaction source time-series for the recovery conditions in frontal cluster. D) 3D brain of the significant clusters for the three way interaction in the late window. E) 3D brain of the significant cluster for the local by global interaction when recovered.

prediction error reported in (Shirazi-Beheshti et al. 2018), suggesting that inferior frontal regions are the source of this shifting neural responsiveness. The latter of these properties (amplitude increase for LSGD) is particularly striking, and important, since the LSGD condition is in a sense the most cognitively demanding condition. In particular, there is no bottom-up deviance (as there is in the LDGD condition) signalling an infringement of global regularity. Thus, higher levels in the processing hierarchy effectively need to detect global deviance by the absence of a driving bottom-up prediction error. Our findings suggest that this capacity is realised by inferior frontal regions, consistent with the often discussed role of prefrontal regions in working memory maintenance and update (Polich 2007). Fig. 44E) shows the significant clusters for the local by global interaction (recovery) in the late window. The statistical results for the three way interaction are presented in Table 19, with p-value (FWE) being 0.005 for both clusters.

Clusters	Peak location	$F_{(unc.)}(1,119)$	$P_{(unc.)}$	$P_{(FWE)}$	K cluster size
Late window					
Left frontal	(-46, 20, -10)	12.21	0.001	0.005	267
Right frontal	(46, 22, -10)	12.22	0.001	0.005	261

Table 19: Three-way interaction statistics. Statistics of three way interaction for both frontal clusters in the late windows. Each cluster, named in the first column, is characterized by its peak location in MNI coordinates as shown in the second column, the F-value of the peak (third column), the p-values (fourth and fifth column) and the cluster size (last column). The first p-value is the uncorrected value at the voxel level of the peak location. The second p-value is for the cluster after family-wise error correction, set to 0.05.

5.4.5 Sedation level

Additionally, we found a significant effect of sedation in the temporal region, and a significant sedation by local interaction in the frontal region. The sedation by

global interaction is not found to be significant in the current analysis.

Sedation Effect

The sedation effect is significant in the temporal sources both in the early and middle window, as shown in Fig. 45A) and B) and Table 5 below. Fig. 45C) shows the time course for the temporal cluster, with the most important effect in the first window.

Sedation by Local Interaction

The sedation by local interaction is significant at both the left and right frontal lobes, as shown in Figs. 45E) and F) with the 3D brain and Table 21 below. The time-series for the left frontal cluster is presented in Fig. 45D), with a first peak in the middle window and an effect reversal in the late window.
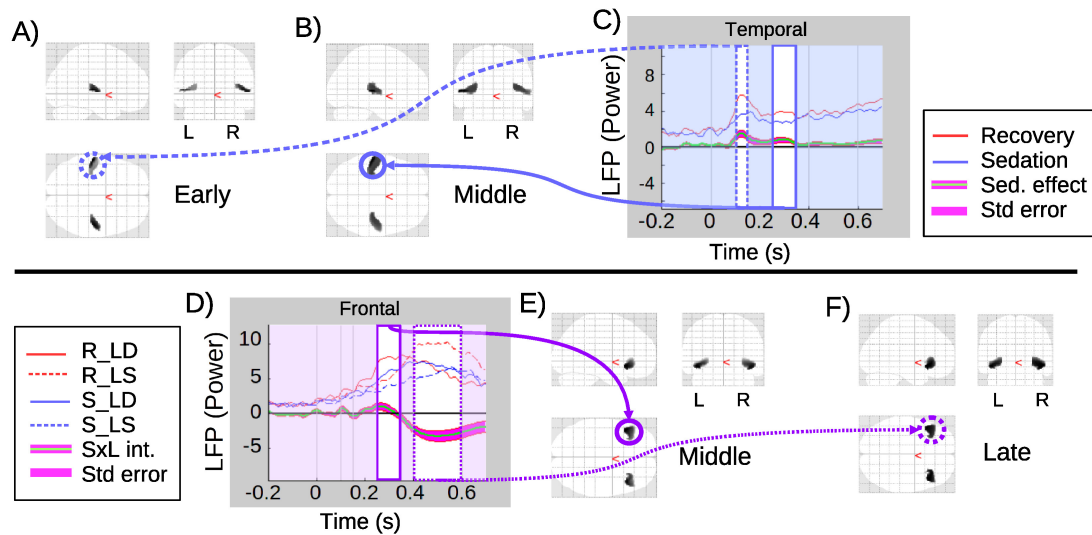
Figure 45: Sedation effect and sedation by local interaction. Results of the inversion for the sedation effect (A-C) and for the sedation by local interaction (D-F).

Clusters	Peak location	$F_{(unc.)}(1,119)$	$P_{(unc.)}$	$P_{(FWE)}$	K cluster size
		Early window			
Left temporal	(-48, -26, 4)	21.81	<1e-3	<1e-3	518
Right temporal	(50, -20, 4)	21.58	<1e-3	<1e-3	408
		Middle window			
Left temporal	(-46, 24, 4)	14.79	<1e-3	<1e-3	364
Right temporal	(42, -20, 8)	13.81	<1e-3	0.002	269

Table 20: Sedation effect statistics. Statistics of the sedation effect in the early and middle windows. Each cluster, named in the first column, is characterized by its peak location in MNI coordinates as shown in the second column, the F-value (third column), the p-value (fourth and fifth column) and the cluster size (last column). The first p-value is the uncorrected value at the voxel level of the peak location. The second p-value refers to the p-value of the cluster after family-wise error correction, set to 0.05.

Clusters	Peak location	$F_{(unc.)}(1,119)$	$P_{(unc.)}$	$P_{(FWE)}$	K cluster size
		Middle window			
Left frontal	(-46, 20, -10)	12.58	<1e-3	0.007	199
Right frontal	(44, 22, -12)	12.48	0.001	0.009	188
		Late window			
Left frontal	(-46, 20, -10)	12.08	0.001	0.007	241
Right frontal	(46, 22, -10)	12.1	0.001	0.006	248

Table 21: Sedation by global interaction statistics. Statistics of the sedation effect in the middle and late windows. Each cluster, named in the first column, is characterized by his peak location in MNI coordinates as shown in the second column, the F-value (third column), the p-value (fourth and fifth column) and the cluster size (last column). The first p-value is the uncorrected value at the voxel level of the peak location. The second p-value refers to the p-value of the cluster after family-wise error correction, set to 0.05.

5.5 Discussion

In this section, we analyse the results in relation with the mismatch negativity, related mostly to the local effect in the early window, the P300 effect which takes place during the middle and the late window, decomposed respectively in the P3a and the P3b components. The effect of sedation and the interactions are also explained regarding those windows.

During the early window, the main effect of local is significant. This effect is found in temporal, with the implication of frontal activity during the middle window. The temporal area is implicated in the first stage of auditory perception (Naatanen et al. 2007), while the mismatch negativity was proposed to include both temporal and frontal areas (Garrido et al. 2008).

The global effect starts from the early window with a frontal activation. The CNV can explain this first global effect (Chennu et al. 2013). During the middle window, a full network of frontal, temporal and parietal clusters are included for the global effect. Then a fronto-parietal activation appears during the late window for the global effect consistent with the global workspace theory (Dehaene and Changeux 2011).

The interaction between the local effect and the global effect is found significant for the middle window in temporal. This interaction shows that these two effects are not independent (as proposed in (King et al. 2014)), but they have a relationship: a change in the local effect will affect the global effect. Then, temporal cortex provides a gate between the early and late effect. We propose the hypothesis that temporal region is a hub from the early stage of information processing (with low-level sensory input in the early window) to the higher processing during the late window. From a predictive coding perspective, this interaction is made possible by the relationship between the feed-forward and the backward communication. The former comes from low-level of sensory input which propagates to higher levels. On the contrary, the latter is due to the neural processing of internal representations, i.e. prediction, which is fully activated during the global effect. We further hypothesise that a functional interaction is fundamental for the prediction error, i.e. to have a mental representation which fits with the sensory input, to minimise the prediction error.

To summarise, we propose a three-phase theory for the local-global processing, as shown in Fig. 46. We would argue that the three phases can be distinguished according to the following characteristics.

Phase 1 (input sensory circuit): activation is restricted to (auditory sensory) superior-temporal regions, giving the circuit a local-area scale for low-level processing. The area acts with a short time frame, with its neural response being the forward propagation of a bottom-up (sensory) prediction error.

Phase 2 (gateway circuit): this is hypothesised to be a meso-scale network, involving an exchange between (auditory) superior-temporal and inferior-frontal sources. The network incorporates modulatory dynamics, which may implement a priority-based enhancement. This gateway circuit exhibits a more sustained phasic response but is not meta-stable in the sense of phase 3. This gateway circuit may be a critical component to allow a large-scale global workspace of phase 3 or to inhibit low-level feedforward signals during preconscious or subliminal perception.

Phase 3 (spanning): this circuit is argued to be large-scale, spanning the long-range cortical sheet. It would naturally be related to the global workspace (Dehaene and Changeux 2011) and would exhibit a meta/macro-stable response, as discussed in (King et al. 2014).

To elaborate further, the interaction between local and global (phase 2) in the middle window suggests a multiplicative exchange between superior-temporal regions and inferior frontal areas. The former of these implementing circuits realising sensory prediction which underlie the local effect, and the latter implicated in higher order processing, which integrates over a more extent temporal window.

This network may effectively be a sub-circuit of the brain spanning global workspace, being a transition state on the way to it, indeed perhaps a proto-workspace. Although further work is certainly required to confirm the hypothesis,

Phase 1
Sensory Circuit

Phase 2
Gateway Circuit

Phase 3
Spanning Circuit

B. V1

Version 1

A

Phase 2
Gateway Circuit

C

B.V2

Version 2
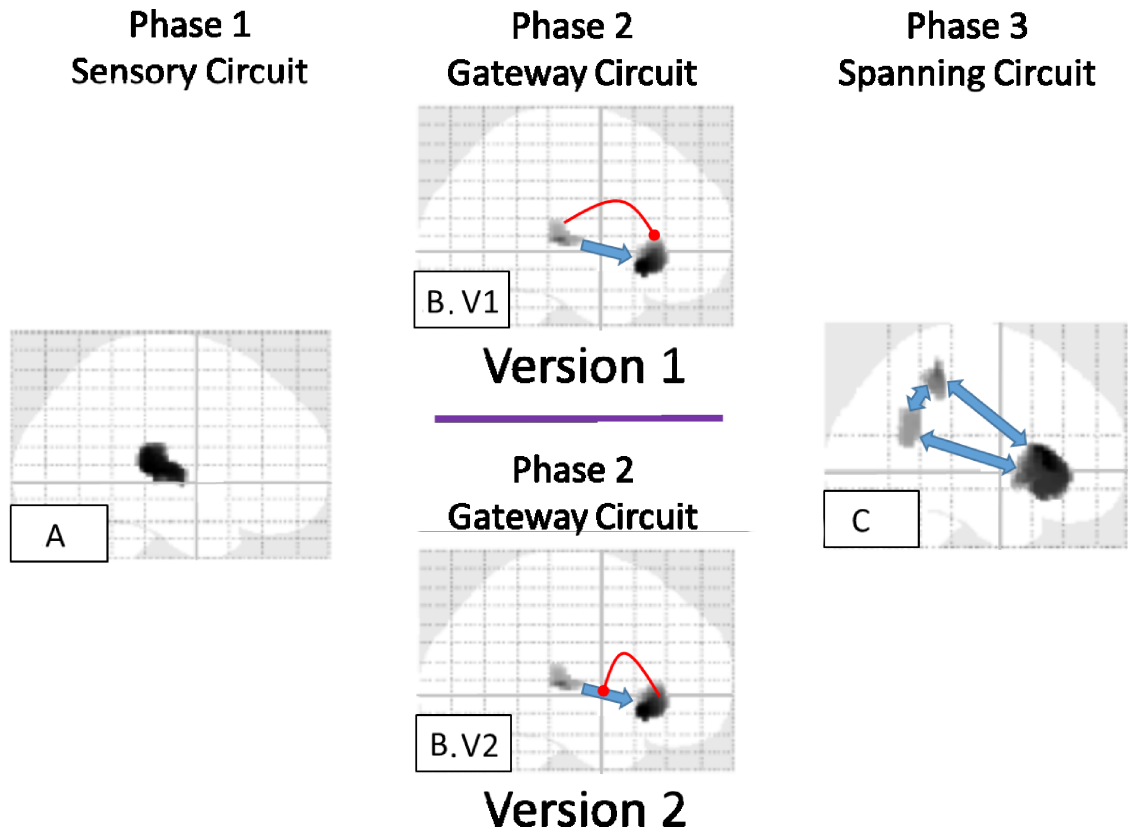
Figure 46: Three phases theory of local-global processing. Phase 1 (c.f. panel A), the neural circuit on the left is localised in the sensory areas related to low-level processing with sensory prediction error. Phase 2, the gateway circuit in the middle, involves interaction between sensory areas and an inferior frontal region. Two different versions are proposed (c.f. panel B.V1 and B.V2) which are distinguished by the direction of the modulatory activity. Phase 3 (c.f. panel C), the spanning circuit on the right, involves a brain-scale circuit similar to a global workspace activation. We hypothesise that phase 2 interfaces between phase 1 and phase 3, to modulate 'ignition' of the global workspace. This modulation may be associated with the feedforward signal.

it might be argued that the local by global interaction in the middle window

is suggestive of bidirectional exchanges between layers in a predictive hierarchy,

with the multiplicative interaction between levels suggestive of modulation of gain

control, which, under predictive coding, could be generated by feedback of preci-

sion (Kanai et al. 2015).

The sedation effect in frontal for the early window strengthens the finding from Boly et al. (2012), which shows that frontal cluster modulates the feedback connexion between frontal and temporal for the mismatch negativity. In particular, Boly et al. (2012) found that reduced consciousness patients (vegetative state) exhibited a reduction in effective connectivity for a feedback link from inferior frontal to superior temporal regions. Furthermore, this link was found absent during a mismatch negativity task, very similar to the local component of the local-global task. While we are limited in our capacity to decompose our temporal region (which effectively arises from a lack of structural scans), and thus directly implicate superior temporal regions beyond primary auditory cortex, we have found effects of sedation specifically in (superior) temporo and inferior-frontal regions. Thus, two different forms of reduced awareness (vegetative state and sedation) seem to impact the same brain network. However, with the statistical power available to us, we did not find any effects of sedation on parietal areas, while strong effects were found fronto-temporally. This stands against an existing finding of propofol-induced modulation of parietal networks (Schrouff et al. 2011). From a global workspace perspective, this might seem surprising, since it has been argued to be the site of conscious experience. This said, with classical statistics, null effects are always difficult to interpret, and there remains the possibility that a more highly powered experiment would find an effect at parietal lobe.

The three-way Interaction was observed at an inferior frontal source. When we decompose this three-way interaction into its component two-way simple effects – local by global when recovered and when sedated – the cause of the three-way is clear. The acceleration of the global deviant response by the coincidence of local deviance (the double surprise acceleration effect as shown in (Shirazi-Beheshti et al. 2018)), is evident at the inferior frontal source both when sedated

145

and when recovered, with this acceleration being stronger when recovered. This accelerated response is apparent in the sharper onset and offset of the LDGD condition when recovered compared to sedated; see Figs. 44B), C). This suggests that the deceleration of the accelerated prediction error described in (Shirazi-Beheshti et al. 2018), can be localised to inferior frontal regions.

The most striking feature driving the three-way interaction at frontal in the late window is the dramatically higher LSGD condition when recovered than when sedated; see Figs. 44B), C). Importantly, the LSGD condition is most dependent upon long-term temporal integration. In particular, this global deviance is not marked by a sensory prediction area (since it arises during a local standard quintuple). Thus, the deviance is not initiated by a strong bottom-up signal (i.e. a local prediction error). That is, it is a real global deviance condition, with its detection intrinsic to higher hierarchical levels. Then, this can be related to a more important prediction error (higher level). Indeed this condition is the more demanding cognitively, and minimising the free energy to detect the global deviance pattern while the local condition is standard requires more effort, hence an increase of prediction error. It takes a longer time for the global deviant prediction, however, this effect is more stable compared to the LDGD which has a double acceleration but vanish quickly.

Finally, such an experiment would been of interest at a single subject level. One can think of a machine learning algorithm to be able to detect states of sedation and find the transition to recovery.

Chapter 6

Difference of Cortical Activity in Elite Cycling Athletes

6.1 Chapter Outline

In this chapter, we investigate the brain differences between two categories of elite athletes. The EEG patterns in sprinter cycling athletes and endurance cycling athletes were analysed. These analyses are an exploratory part of states of consciousness on awake expert subjects. In particular, we were testing the hypothesis that two different populations of individuals highly skilled can present different neural patterns and the effect of Time on Task (ToT) on elite athletes. First, we present the dataset and the context of this research in the field of cognitive states. Then we describe the methods of spectral power analysis used for the analysis, and finally, the results are presented. A discussion closes this chapter.

6.2 Introduction

During the previous chapters, we have been interested to different cognitive states, either pathological (coma/QBD), or induced sedated. We investigate in this chapter cognitive states of healthy subjects. One can be either in a resting state (not engaged in a specific activity) or engaged in a cognitive and/or physical action. For any cognitive task, this needs to be trained. It can be done either by a short instruction, as during the local-global experiment. In this simple task participants need to count the number of global deviant. But there is also the case of long training, as with elite athletes or skilled/expert man or woman who have thousand hours of practice. In this analysis, we are interested in the impact of high training in the brain of highly skilled athletes. There are strong evidences which show a modification of the cerebral activity with elite athletes during preparation and anticipation of their actions (Yarrow, Brown and Krakauer 2009), compared to a control group.

Moreover, it is assumed that these trainings which occurs with elite athletes or other skills make long term changes in cortical activity. Different imaging modalities have been used to highlight this process of neuronal plasticity. We present here two examples, one on EEG with long term meditations participants, the other with fMRI applied to taxi drivers which reflects brain plasticity in highly trained people. In the first example, two groups were asked to focus for few minutes on a state of awareness. Their EEG activity was recorded during this task. It has been shown that people with a long training of meditation develop a more strong power activity in the gamma band ($> 40Hz$), compared to a control group without meditation training (Lutz et al. 2004). In the second study, taxi drivers and bus drivers were doing driving simulation task and their brain activity

was recorded with fMRI. It has been shown that taxi drivers develop an increase of gray matter volume in the posterior hippocampi which correlates with years of navigation experience Maguire, Woollett and Spiers (2006). Volume is also significantly greater for taxi drivers than for bus drivers who navigate the city along a small number of fixed routes, compared to taxi drivers.

However, little as been done on investigating the brain plasticity of athletes at rest. In our experiment, we are comparing two different kind of elite athletes. One group of athletes is specialized in endurance cycling. The other group of athletes is specialized in sprinter cycling. We expect to find different cognitive signatures between these two different populations. A cognitive task is also performed by the participants to induced a fatigue state. Mental fatigue usually incurs performance with ToT. It can lead to decreased physical performance, however little is known about mental fatigue in elite athletes, and between different population of athletes. We expect the endurance cyclists to be less influenced by the fatiguing cognitive task, due to the ability to perform physical activity for a long period of time during their preparation. On the contrary, sprinter cyclists performed strong efforts during a short period of time, therefore we can expect that performing a cognitive task for 30 minutes with no interruption may induced mental fatigue on their brain.

6.3 Dataset

6.3.1 Experimental Design

The experiment was performed in collaboration with the Australia Institute of Sport [1] and University of Canberra. There are two groups on the experiment. The first group had 10 participants who are elite endurance cyclists and the second group had 10 participants who are elite sprinter cyclists. Both groups were involved in the mental fatigue task, which consisted of a Stroop task using the E-Prime 3.0 software. Fig. 47 shows the experimental design. The participants were sat on a chair in front of a computer screen. The experimental task started with a resting state for 4 minutes, with 2 minutes eyes open (as the baseline) and 2 minutes eyes closed. The screen in front of them shown a black cross that the subjects were asked to look at when they had the eyes open and try not to blink. This allows the subject to relax and not gaze around randomly. After the resting period, a Stroop task was performed. It consists on color words displayed on the screen. The color used to display the word can be congruent with the meaning of the color word (e.g. the word 'Yellow' is displayed on the screen in yellow), or it can be non-congruent with the word (e.g. the 'Yellow' word displayed with red ink). The participants were asked to speak aloud the ink color. This task is well known to induce errors related to the incongruent words, i.e. when there is a mismatch between both the color (which activated visual cortex areas related to color) and the meaning of the word (which induced cortex areas related to reading). The task ran for 30 minutes to induce fatigue on the participants. After the task, the participant stayed on the seat for a resting state period of 4 minutes. During this resting state, they had eyes open for 2 minutes looking at the cross

---

[1] http://experienceais.com

on the screen, and then eyes closed for 2 minutes.
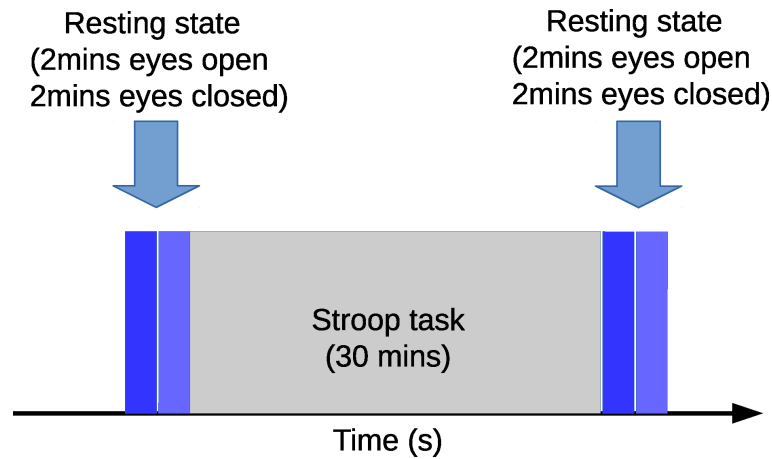
Figure 47: Experimental design for the cycling experiment. Each participant had to sit in a chair in front of a computer screen. A first resting state occurred for 4 minutes, with 2 minutes eyes open and 2 minutes eyes closed. Then the participant performed the stroop task for 30 minutes. At the end of the cognitive task, another resting was done for 4 minutes, with 2 minutes eyes open and 2 minutes eyes closed.

6.3.2   EEG Recordings

The EEG data were recorded using a 10-20 recording system with an Enobio [2] device with 20 channels. Among these channels, 19 were used in the location corresponding to P7,P4, Cz, Pz, P3, P8, O1, O2, T8, F8, C4, F4, Fp2, Fz, C3, F3, Fp1, T7 and F7. One other channel was used as the reference recorded via the earlobe. The sampling rate for recording is $500Hz$, with an input impedance $Z_{in} < 10k\Omega$. The channels used are Silver-Silver Chloride (Ag/AgCl). Fig. 48 shows a sample of 10 seconds recording of EEG from a participant in endurance cycling group.

---

[2]http://www.neuroelectrics.com/products/enobio
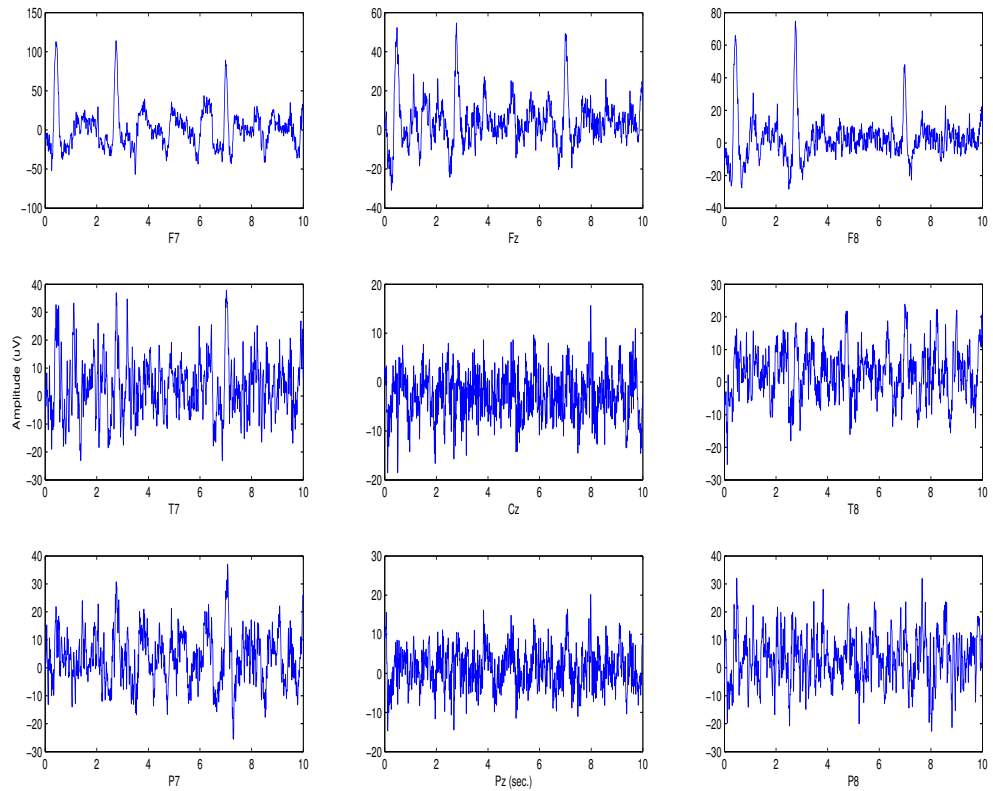
Figure 48: EEG sample for endurance athlete. 10 seconds of EEG resting state eyes open, from top to bottom: frontal, temporal and parietal brain areas; left, center and right of the brain.

6.4 Methods

A spectral power analysis was performed to evaluate the EEG power to evaluate the effect of time and group. The spectral power was extracted in three steps:

- Band pass filtering in the appropriate frequency band

- Hilbert transform of the filtered signal

- Extraction of the power for a 5 second window

The EEG signal was band-pass filtered for the five frequency bands: delta $[1 - 4Hz]$, theta $[4 - 7Hz]$, alpha $[8 - 13Hz]$, beta $[13 - 30Hz]$, and gamma $[30 - 45Hz]$. A FIR filter of order 100 was created to compute the spectral power in each of those bands. On the filtered signal we applied Hilbert transform to have an analytical signal. Any signal can be decomposed as an analytical signal by 'filtering out' the negative frequency. To do this, each sinusoid component of the signal should have been shift by a quarter cycle, the *Hilbert transform filter*. Let $y(t) = H_x(t)$ be the Hilbert transform of the temporal signal filtered $x(t)$. Then, the corresponding analytical signal is $z(t) = x(t) + jH_x(t)$.

This analytical signal $z(t)$ can also be represented by:

$$z(t) = \frac{1}{2\pi} \int_0^\infty Z(\omega)e^{j\omega t}d\omega \qquad (22)$$

For an analytic signal, the magnitude function $a(t)$ and the phase function $\theta(t)$ are given by:

$$a(t) = \sqrt{x^2(t) + y^2(t)} \quad and \quad \theta(t) = arctan\frac{y(t)}{x(t)} \qquad (23)$$

where the envelope of the original signal is described by $a(t)$ which is the instantaneous amplitude of the signal and $\theta(t)$ represents the instantaneous phase of $x(t)$ (Hahn 1996). The power in each frequency band was constructed by the squared amplitude of the envelop $a(t)$. EEG time-frequency power follows a $1/f$ phenomenon, the power at higher frequency like gamma, has a much smaller scale than the power at lower frequency like delta. As such, it is difficult to make quantitative comparison between frequency. Then, a scaling need to be performed to be able to compared equally different frequency band. A baseline

normalisation was applied for each band. The baseline normalization has the following advantages: it transform all power signal to the same scale. This allow to compare, visually and statistically , results from different conditions, electrodes or frequency bands. Also, baseline normalisation put put power results in a easily numerically and common interpretable measure. The baseline normalisation was performed by applying decibel conversion on the signal to baseline ratio. We applied the following equation:

$$Power_{db}(f) = 10 \cdot log10 \left(\frac{Power(f)}{BaselinePower(f)} \right) \tag{24}$$

The $BaselinePower(f)$ is the mean power f of the channel during the first resting state condition eyes open. This power is used as a baseline to normalise the power during the task. The $Power(f)$ is the power for a specific channel and condition. The power is scaled to the $BaselinePower(f)$ (during resting state). The scaled power was finally converted in decibel. This frequency power was changed in power-frequency related to baseline rather than the absolute level of power. This normalise power was compute for the 5 first minutes of the cognitive task and the 5 last minutes, which allow us to compare the time on task effect.

We analysed effects of ToT by evaluating the change in EEG power in five frequency bands during the 5 first minutes of the cognitive task and the 5 last minutes. Based on these measures, we test the statistical significance in each channel for each frequency band at a group level (between-subject factor: sprinter *vs* endurance) and at a task level (within-subject factor: beginning of the task *vs* end of the task) by a 2-by-2 ANOVA. As the EEG was recorded on 19 channels and analysed in 5 frequency bands, we have an issue of multiple comparisons (5 × 19 = 95) which could inflate the type I error. To deal with it, we applied

a non-parametric statistical test with permutation (Maris and Oostenveld 2007) based on the F-value with 2000 random permutations. From this permutation between the twwo groups, we create a surrogate distribution of F-values. From this distribution we compute the final p-value and the ones below 0.05 are selected as significant.

6.5   Results

Table 22 shows the corrected p-value between groups (endurance *vs* sprinter, collapsed by early/late test) for each pair: channel *vs* frequency bands. Table 23 and 24 present the statistics for respectively ToT effect and interaction between cycling and ToT with no significant p-value.

From this analysis, we do not find any effect with ToT during the cognitive task and no interaction effect is found for the resting state and the cognitive task. However, at a group level for the cognitive task we find that power is greater in endurance group than sprinter group. There is a difference of power in the gamma band for $F3$ ($p < 0.03$) and $F8$ ($p < 0.03$); in the beta band for $F3$ ($p = 0.035$); in the alpha band for $P3$ ($p < 0.05$) and $O1$ ($p < 0.03$). In the theta band for $O1$ ($p < 0.03$) and $O2$ ($p < 0.02$); and in the delta band for $O2$ ($p < 0.03$), as shown in Figure 49.

There are statistically significant differences between endurance and sprinter cyclists. In the lower frequency i.e. delta and theta, occipital channels are significant. As the frequency increases, the significant channels are more frontal. Finally, for the higher frequency i.e. gamma the frontal channels are significant. Moreover, as shown in Fig. 50, the endurance group as a stronger global increase of power compared to sprinter. This is particularly true for the theta band on

155

Channels	Delta	Theta	Alpha	Beta	Gamma
P7	0.62	0.48	0.99	0.39	0.19
P4	0.67	0.39	0.48	1	1
Cz	0.78	0.57	1	1	1
Pz	0.78	0.39	1	1	1
P3	0.48	0.43	0.05	1	0.95
P8	0.97	0.87	0.95	0.91	0.57
O1	0.11	0.02	0.02	0.52	0.67
O2	0.02	0.02	0.14	1	1
T8	1	1	1	1	1
F8	1	1	1	0.33	0.03
C4	0.57	0.14	0.78	1	1
F4	1	0.62	0.48	0.22	0.24
Fp2	1	1	1	1	0.97
Fz	0.99	0.67	0.43	0.73	0.39
C3	0.78	0.36	0.33	1	0.95
F3	0.78	0.11	0.24	0.04	0.02
Fp1	1	1	1	1	0.83
T7	1	1	0.91	0.3	0.48
F7	1	1	1	0.19	0.16

Table 22: P-value for cycling effect. P-value after maximum statistic for cycling effect (sprinter vs endurance). The first column indicates the channels, and the five next columns show the p-value for the frequency bands analysed, respectively delta, theta, alpha, beta, gamma. Significant p-value are highlight in red.

the scalp map, where the increase of power covers all the channels, but is only significant for $O1$ and $O2$. Finally, the power in the sprinter group remains stable, with an exception for the theta band, where an increase of activity in frontal is present.

From this experiment the absence of effect for the ToT level during the cognitive task can be explained by the short duration of the task (30 min). Indeed expert athletes used to train themselves for thousand of hours before having a good performance. In contrast, we find significant difference between both groups of elite athletes with stronger EEG power activation in endurance compared to sprinter cyclists, as shown in Figs. 49 and 50.

Channels	Delta	Theta	Alpha	Beta	Gamma
P7	1	1	1	1	1
P7	1.00	1	1	1	1
P4	1	0.99	0.57	1	1
Cz	1	1	1	1	1
Pz	1	1	0.92	1	1
P3	1	1	0.99	1	1
P8	1	1	1	1	1
O1	1	1	1	1	1
O2	0.92	0.87	0.98	1	1
T8	1	1	1	1	1
F8	1	1	1	0.41	0.75
C4	1	1	0.99	1	1
F4	1	1	1	0.99	1
Fp2	1	1	1	1	0.87
Fz	1	1	1	1	1
C3	1	1	1	1	1
F3	1	1	1	1	1
Fp1	1	1	1	1	0.98
T7	1	1	1	1	1
F7	1	1	1	0.57	0.75

Table 23: P-value for time on task effect. P-value after maximum statistic for the time on task effect (beginning vs end of cognitive task). The first column indicates the channels, and the five next columns show the p-value for the frequency bands analysed, respectively delta, theta, alpha, beta, gamma. No p-value is significant.

Channels	Delta	Theta	Alpha	Beta	Gamma
P7	1	1	1	1	1
P4	1	1	1	1	1
Cz	1	1	1	1	1
Pz	1	1	1	1	1
P3	1	1	1	1	1
P8	1	1	1	1	1
O1	1	1	1	0.97	1
O2	1	1	1	1	1
T8	1	1	1	1	1
F8	0.64	0.55	1	1	1
C4	1	1	1	1	1
F4	1	1	1	1	1
Fp2	1	0.81	0.97	1	1
Fz	1	1	1	1	1
C3	1	1	1	1	1
F3	1	1	1	1	1
Fp1	0.97	0.48	0.68	1	1
T7	0.95	0.90	1	1	1
F7	1	0.84	0.98	1	1

Table 24: P-value for cycling by TOT interaction. P-value after maximum statistic, for interaction between cycling expertise and time on task. The first column indicates the channels, and the five next columns show the p-value for the frequency bands analysed, respectively delta, theta, alpha, beta, gamma. No p-value is significant.
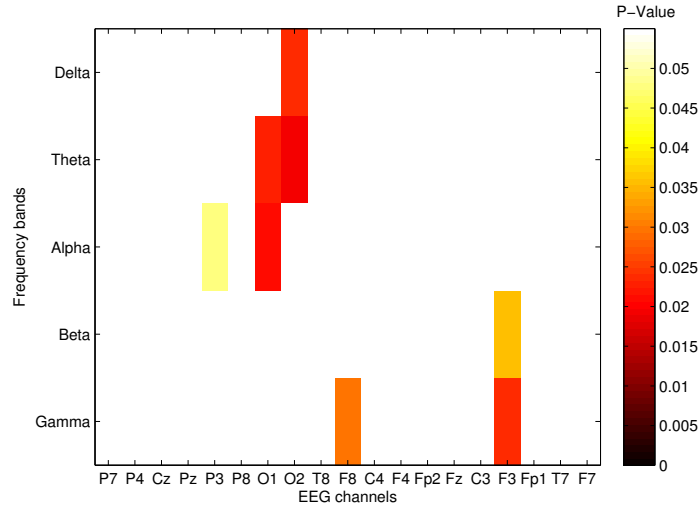
Figure 49: P-value with threshold at 0.05 for main effect of cycling. The p-value which are significant are shown with the frequency band on the y-axis, from top to bottom: delta, theta, alpha, beta and gamma. The x-axis represents the 19 channels used for the recording. The graph bar indicates the strength of the p-value, from 0.05 in light yellow to 0.005 in dark red. Occipital channels (O1, O2) are significant for lower frequency, and frontal channels (F3, F8) are significant for higher frequency.

6.6   Discussion

We have shown on this analysis the possibility to distinguish between two categories of experts. In particular, these cycling experts have been recorded during resting state and cognitive task. We made the hypothesis that the Stroop task may have an effect on the brain due to the mental exhaustion made by the cognitive task. We also made the hypothesis that the different expertise may be revealed at the brain level with different electrical activity patterns.

The first hypothesis (H_0: mean of power EEG brain activity is the same before and after the cognitive task) is true. There is then no difference of the brain activity in terms of spectral power analysis before and after the task, due to the
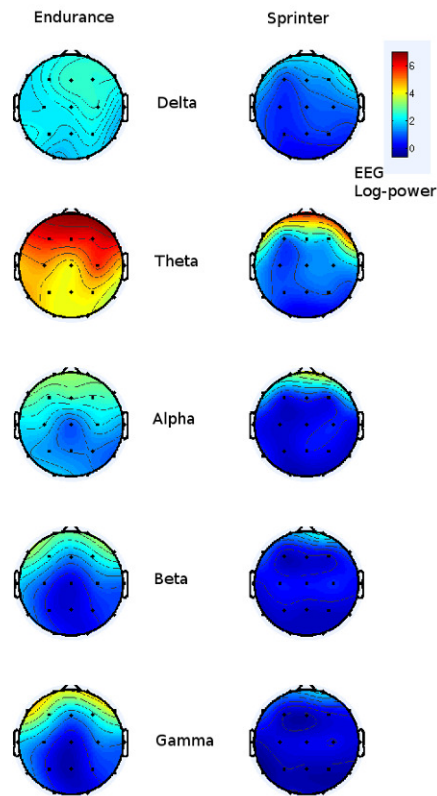
Figure 50: Mean log-power between endurance and sprinter. This shows the scalp-map in a log-power scale for endurance group is on the left, and for sprinter group on the right, for each frequency band respectively: delta, theta, alpha, beta, and gamma. The baseline reference is the resting state eyes open, before task.

mental effort put on the task. This can be explained as the group of participants involved in the task are cycling athletes used to do long session of exercise.

The second hypothesis (H_0: mean of power EEG brain activity is the same between endurance elite cyclists and sprinter elite cyclists) has been rejected. Cycling expert present significant differences between both groups, starting from occipital for lower frequencies, and moving through frontal brain area for the higher frequencies. First, delta band shows differences in occipital right. In the theta

band, both O1 and O2 in occipital are significantly different. For the alpha band, the right hemisphere is significant in occipital and parietal. This difference switch in frontal left in the beta band (in F3). Finally, for the gamma band both left and right frontal brain areas (F3, F7) are significant. This difference low frequency in occipital, high frequency in frontal, may reflect that the brain of elite athletes processes information in a more efficient way, with a better brain organization, and particularly differently between different expertise, which may be reflected by difference in frontal brain area. For example, this has been proposed as a 'neural efficiency' by Yarrow, Brown and Krakauer (2009) from EEG of elite athletes.

Elite athletes have a deliberate practise with optimised training strategies and feedback for thousand of hours in order to achieve high performance (Yarrow, Brown and Krakauer 2009). This high level of expertise may be reflected for the subject's ability to conduct cognitive activity. This expert practice is not found only in sport. For example, with trained practitioners of meditation, their practice revealed an increased in the gamma frequency band, as shown on Fig. 51. Interestingly, we see that during the meditative state, which can be compared to a state mental preparation for cycling, the difference in gamma is also present in frontal areas, as we found in our analysis. The increased of power is present in all the practitioner mainly in frontal and parietal areas of the brain. However, the gamma power increase is not present in the control group (Lutz et al. 2004).
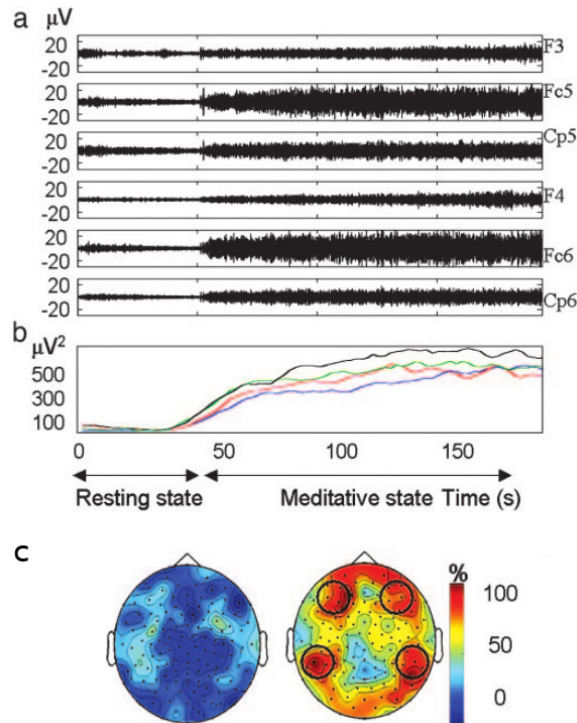
Figure 51: Gamma activity during mental training. a) Raw electroencephalogram signal for 6 channels. At $t = 45s$, a trained practitioner started generating a state of non-referential kind of meditation. b) Time course of gamma activity during four blocks. The power is averaged on the 6 channels. c) Scalp distribution of gamma activity during meditation. The color scale indicates the percentage of subjects in each group that had an increase of gamma activity during meditation compared to the neutral state. (Left) Controls. (Right) Practitioners. Particularly, frontal gamma is significant as found with cycling group effect. Figure from Lutz et al. (2004).

Chapter 7

Source Reconstruction on Lift Fatigue Data

7.1   Chapter Outline

In this chapter, we study how the brain reacts to physical task including motor control. In particular, we devised an experimental design implying physical activities while recording the brain activity at the scalp level using EEG. After an introduction to the interaction with the brain during physical activity, we presented the experiment and dataset used for these analyses. There are two explanatory factors, one being fatigue and the other being weight. We then presented the method of source localisation using MSP for these analyses before the results. We shown in this study a main effect of weight during the rising phase of experiment and discussed these results at the end.

7.2   Introduction

In the following study, we are interested in the evolution of cortical activity during a physical task. Few studies have been done on the relationship between cortical activity as measured from EEG and perception of effort during physical tasks. The research in this chapter aimed to test the correlation between the perception of effort during a physical task and the central motor command related to the cortical activity from EEG. A key idea in motor control is that the brain makes an internal simulation known as a *forward model*, to predict the changes in an internal state of body or external state of object that will result from an outgoing command, as shown in Fig. 52. This can be included in a more broader model of predictive coding (Friston et al. 2007) in which the brain is doing a simulation of the outer world to adapt the inner representation of the world to the sensory inputs. In these conditions, the brain is constantly adapting itself to minimize the predictive error and make a consistent inner representation of the outer world given by the sensory input.

For this analysis, two experimental manipulations were applied. The first factor is to control the intensity of the weight by asking participants to lift a light weight and a heavier weight. As a second factor, one of their arms was fatigued by eccentric exercise, to be compared with a non-fatigued arm from another session. Analyses of perception of effort were already performed at the scalp level and found significant fatigue and weight effect, mainly at Cz (de Morree, Klein and Marcora 2012). The purpose of this research is to understand the neural activity related to these effects. Thus, we applied imaging source reconstruction methods in two windows: the first one for the weight raising and the second one for weight lowering. We also extracted the source time-series to explore the evolution of
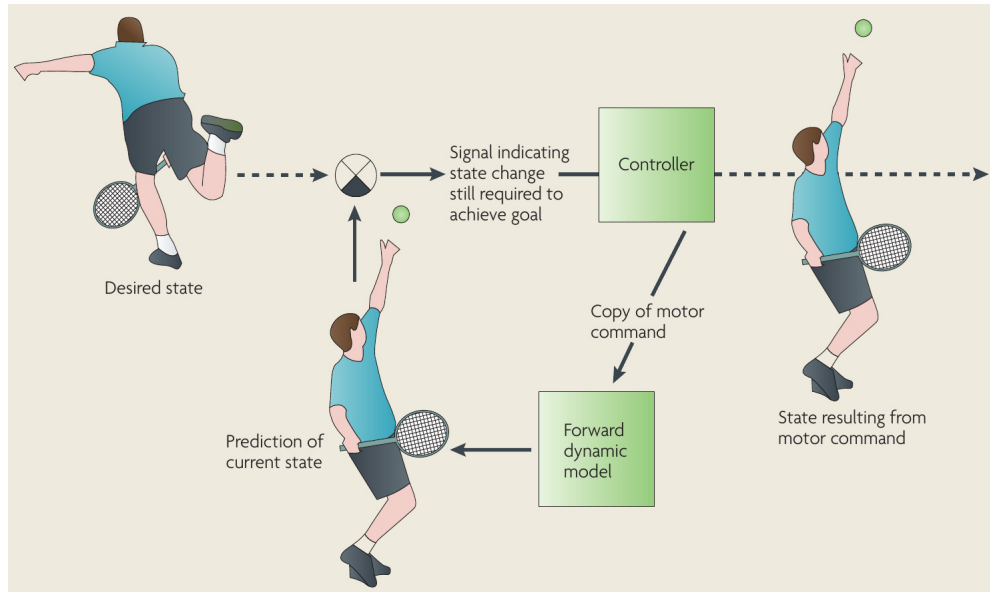
Figure 52: Forward model for motor control. The forward model allows the brain to have an inner representation of the world to anticipate and prepare the output to send to the motor control for a specific goal.

neural activity in the different condition.

7.3   Dataset

7.3.1   Participants

For this study, 21 male volunteers participated. Due to excessive artefacts, five participants were excluded. We therefore present the data of 16 subjects (mean age and standard deviation 27 ± 7 years). Participants were right-handed and had no known mental or neurological disorders, based on self-report. All experiments were approved by the ethics committees of the School of Sport, Health and Sciences and the School of Psychology of Bangor University, and conformed to the standards set by the Declaration of Helsinki.

7.3.2 Experimental Design

The participants visited the laboratory twice. The first visit was a familiarisation session, while the second visit was the experimental session. During the session, the measured variables were Rate of Perceptive Exhaustion (RPE), Muscle Related Cortical Potential (MRCP) and electromyogram (EMG). The first independent variable was weight: participants were asked to lift two weights based on the maximum weight they could lift: a lightweight (20% of one repetition maximum 1RM) and a heavier weight (35% 1RM). The second independent variable was muscle fatigue, defined as an exercise-induced reduction in the ability to produce force with a muscle during a maximal voluntary contraction (Enoka and Duchateau 2008). During the experiment, it was controlled potential confounding effects of increased sensory feedback by keeping them constant between conditions and a 20 s recovery separated repeated eccentric contraction.

7.3.3 Familiarization Session

During the first meeting, participants gave written consent and completed a questionnaire about their medical and physical activity. First, instructions about the CR10 test were given to the subject, for the rating of perceived effort (Borg 1982). The effort was defined to the participants as to how hard they had to push their arm to lift the weight. This test has 11 levels from 0 (*no effort at all*) to 10 (*maximal effort*). It includes verbal anchors of perception of effort, such as light, moderate, and hard for intermediates values. The rating should be based exclusively on effort and not any burning sensation in the arms (one sensation that is usually described as muscle pain).

Then, the participants were monitored to evaluate the one repetition maximum

(1RM) for elbow flexion of the right arm. They sat on a chair with the right arm on a support and a cushion under the elbow. They had to lift a handheld dumbbell until they touched a flexible ruler that was placed 2 cm above it, first for a few warm-ups. Then, the weight was gradually increased until it was too heavy for the participants to lift it. The heaviest successfully lifted weight was recorded as 1RM. The participants were encouraged and asked to rate their effort to familiarised with the RPE scale. The maximal scale of the RPE was set when the presented weight was too heavy to lift despite maximal effort. During the later session, participants were free to rate above this level if they felt the effort was higher than the maximal score during the preliminary test. Finally, after establishing the 1RM participants were familiarised with the protocol for the second visit. They repeatedly lift handheld dumbbells of 20% and 35% 1RM in a set rhythm. As for the 1RM procedure, participants had to fix their gaze on a fixation cross. The rhythm for lifting the weights was done by E-Prime 1.2 (Psychology Software Tools Inc., Sharpsburg, PA): beeps were presented at a rate of 1 Hz. The cue to rise and lower the weight were indicated by two high tone beeps, while rest periods were indicated by six low tone beeps. Participants were asked to use a regular pace for lifting the weights and do not wait high tone beeps to respond to. The beeps were used only to give the pace of lifting, but the trigger was set up by the EMG.

7.3.4   Experimental Session

During the 24 hours preceding the experimental session, participants were asked to avoid alcohol consumption and intense exercise, to maintain their usual diet and to drink 40 ml of water per kg body weight. Moreover, they should sleep more

than seven hours before the test and avoid smoking and caffeine consumption at least three hours before the test, and two hours before the test, they had a light meal.

A gap of at least five days took place between the familiarisation session and experimental session to ensure the participants recovered from the 1RM protocol. The right and left arm were randomly selected to be fatigued by eccentric exercise on a dynamometer. Both arms were tested for isometric Maximal Voluntary Contraction (MVC) torque of the elbow flexor muscle, starting with the control arm. First, they held the lever arm of the dynamometer with their active arm. The axis of rotation of the dynamometer was aligned with the humerus. After three sub-maximal warm-up and familiarisation trials (25%, 50%, and 75% of maximal effort separated by a 30s rest), they were asked with strong encouragement to maximally contract for 5 s. One min rest periods were taken between these MVC trials. The MVC value was chosen as the average of the two maximal torque values. Then, the participants performed eccentric contractions of the elbow flexors with the selected arm for the fatiguing protocol. They should maximally resist elbow extension generated by the dynamometer. When the participants' arm reached full extension, they were instructed to relax their arm, which was then returned to the starting position by the experimenter. This procedure was repeated for 20 s, with encouragement to maintain maximal torque levels throughout each contraction. The goal was to reduce the maximal contraction torque by 35% of strength loss. On average, participants did 56 ± 12 maximal eccentric contractions. After the trials on the fatigued arm, the same procedure was applied on the non-fatigued arm. Once these exercises were performed, the participants were transferred to the EEG laboratory to wear the EEG electrodes. They were required to lift the light and heavy weight (20% and 35% of 1RM) with the fatigued and non-fatigued

arm, resulting in four blocks, presented in random order: light-fatigued, heavy-fatigued, light non-fatigued and heavy non-fatigued. Each block was composed of 50 trials, for nine minutes, and after every ten trials, the RPE scale was asked for 20 s. Blocks were separated by a rest period during which participants can rest and relax by drinking some water if needed.

7.3.5   Electro-Physiological Recording

The EEG recording was performed in a Faraday cage, with 62 Ag/AgCl electrodes used with abrasive electrolyte gel as a conducting agent. The electrodes take place using the 10-10 positions. The reference electrode was positioned at Cz, with FPz used as ground. Sampling rate for the EEG recoding was 1000 Hz, and data were recorded using Brain Vision Recorder 1.033 (Brain Product).

7.3.6   Data Analysis

Brain Vision Analyser software (Brain Product) was used for the pre-processing. The pre-processing was performed before the source reconstruction procedure, by the same team who did the recording. EEG data were filtered with a 0.05 to $40Hz$ band pass filter. Artefact were removed using independent component analysis (ICA) for each subject using FastICA method. The components related to blink, eyes movement, EMG were identified as independent components and removed from the data. After rejection, EEG data were re-referenced to the average to reduce noise common to all the channels. EMG onset and offset were detected by visual inspection, and used to segment the data 2 seconds (2 s) before the EMG onset to 4 seconds after. A low pass filter of 8 Hz was applied for MRCP analyses. Then, a baseline correction was applied on all trials from -2 s to -1.5 s, selected to

be not to close to the onset of MRCP and not containing activity from previous trial. Trials can be decomposed in four epochs: 1) readiness potential from -1.5 s to 0; 2) weight raising from 0 to 1 s; 3) weight lowering from 1s to 2s; and 4) recovery from 2 s to 4 s. In the Fig. 7.3.6 is shown the grand average for the four conditions, on the Cz channel.
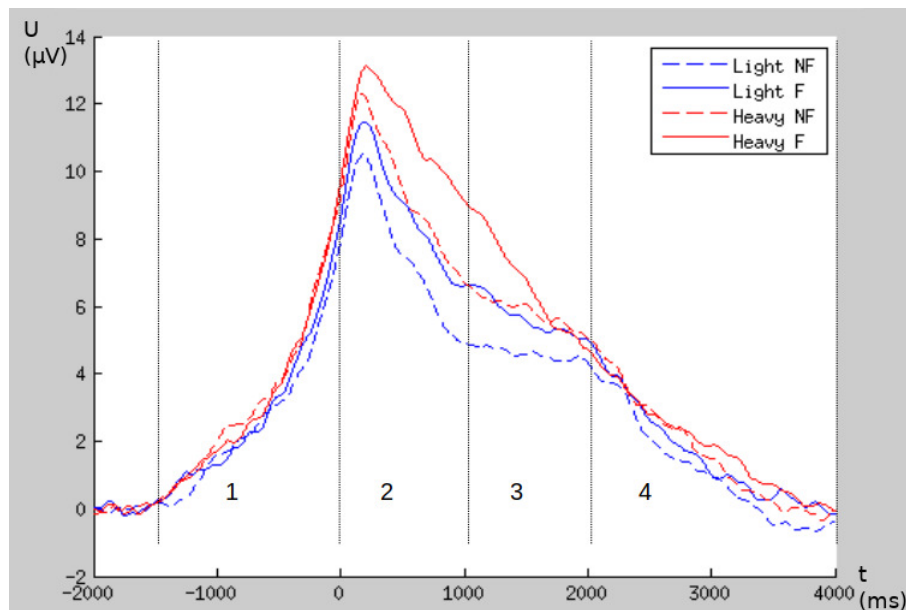
Figure 53: Lift experiment: MRCP for Cz channel. The four conditions represented by the MRCP are, light non-fatigue (dashed blue), light fatigue (blue), heavy non-fatigue (dashed red) and heavy fatigue (red). The vertical lines represent the four windows, which are as follow. 1: readiness potential, 2: weight raising, 3: weight lowering, 4: recovery.

Previous analyses shown significant effect of weight along the midline, and significant effect of fatigue on Cz. Therefore, we were interested to analyse the effect at the source level and their interaction. In particular, we explored neural activity at the primary motor cortex, the primary sensory cortex and the anterior cingulate cortex for the rising window and the lowering window. The main scientific question is to establish the neural sources where these effects originate.

7.4 Methods

The framework for the source inversion analysis follow the steps shown below:

- Co-registration

- Forward model

- Group inversion

7.4.1 Co-Registration

Co-registration between the scalp level and the source level in MRI space was applied. Coordinates at the scalp level come from a standard GSN-Hydrocel template with 64 channels. Three fiducials are used to map the coordinates from the scalp-level to the source-level: nasion, left peri-auricular point and right peri-auricular point. As no MRI scans were recorded for the participants, a template head model based on the MNI brain was applied with a cortical template mesh which describes the dipoles.

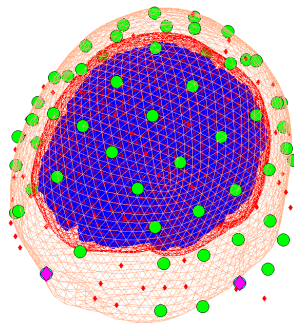Figure 54: Co-registration between EEG channels (green dots) and source space (blue mesh). The co-registration is applied between the MNI space with the mesh volume (brain, CSF and skull), and the sensor space (sensors represented by green dots). The three fiducial shown in magenta, are used for the change of referential.

7.4.2 Forward Model

The forward model uses the physical properties of the brain map dipole activities to the scalp activities at the sensor level. It results on the lead-field matrix. The forward model has been computed using the BEM (Boundary Element Method) option as suggested by SPM 12 (Friston 2007) for EEG-based source localisation analysis, with a three layer head model, i.e. skin, skull and brain.

7.4.3 Group Inversion

The Multiple Spare Priors source inversion algorithm has been used for the source reconstruction (Friston, Kilner and Harrison 2006; Lopez et al. 2014). We selected two windows to reconstruct the cortical activity, the readiness potential and weight raising. A sub-space has been selected for the source reconstruction, to focus on the areas involved in motor control and fatigue. The sub-space is applied based on literature, but others may also be appropriate. Further analysis could be used to differentiate between different sub-space. In these analysis, we used primary motor cortex and primary sensory cortex (Anderson et al. 2011). These neural sources are expected to be active during the experiment. One other component was used to gather extra-information not included in the motor or sensory cortex. Anterior Cingulate Cortex (ACC) was selected, as it is an important contributor to the perception of effort and for motor control (Paus 2001). Table 25 show the coordinates used for the sub-masks and the radius of the sphere which define the mask.

Name (Mask)	Hemisphere	Coord. (x	y	z)	Radius (mm)
Primary Motor Cortex	L	-8	-14	74	10
(PMC)	R	12	-16	74	10
Primary Sensory Cortex	L	-8	-34	70	10
(PSC)	R	8	34	70	10
Anterior Cingulate Gyrus	L	-18	32	32	10
(ACC)	R	18	32	32	10

Table 25: Coordinates of the masks included for the source inversion. The first column indicates the name of the prior mask location. Then, for either left (L) or right (R) hemisphere the coordinates (x,y,z) are indicated in MNI space. The last column describes the radius of the mask.

7.4.4 Statistical analysis

The statistical analysis for the source space inversion was done using SPM12, with a 2x2 within-subject ANOVA design. For both windows rise and lowering, brain images were extracted for each subject. These images were used for a second level analysis in SPM 12. The first level cluster-forming threshold used an alpha level of 0.05 to define which voxels are treated as statistically significant. The voxels that cross this threshold form clusters, i.e. 3D regions of continuous significance.

For the regions which had significant voxel, we applied a t-test at the source level from the time-series. Time-series were extracted using prior location with a radius of 10 mm. A convolution with a hamming window was applied to smooth the data and generate time-series that can be compared with the SPM analyses, and a square root mean was finally applied. We selected the value in the middle of each window for each condition for the statistical analyses. A paired t-test with an alpha level of 0.05 was applied to evaluate the weight effect, the fatigue effect and the weight by lift interaction.

7.5 Results

We present the source reconstruction results during the rise period and the lower period for the weight effect, fatigue effect and weight by fatigue interaction.

7.5.1 Fatigue Effect

Results for the fatigue effect are shown in Fig. 55. The most significant voxel in both the rising and lowering window are located in the ACC, Figs. 55C) and D). Few voxels are presented from the 3D brain in the window (lowering) Fig. 55D). From the time-series for the sources, as shown in Fig. 55B), fatigue effect increases regularly with a maximum in the lowering window. Interestingly, maximum of fatigue in the primary sensory cortex occurs at the end of the lowering window (Fig. 55A)), while maximum of fatigue in ACC occurs between the rising and lowering windows. This can also be due to other factors than fatigue, e.g. due to pain. Nevertheless the standard error is hight in both sources and the statistics at the source level are not significant ($P_{ts} > 0.05$) as shown in Table 26.

7.5.2 Weight Effect

The weight effect is shown in Fig. 56. During rising window Fig. 56C), left PSC and ACC present significant voxels in left hemisphere, with ACC being more significant. In lowering window Fig. 56C) both left and right SCP present significant voxels, and similarl;y for the left ACC. From the sources time-series, the maximum of weight effect occurs in the middle of the lowering window for SCP Fig. 56A), while it occurs between the rising and lowering window for ACC, Fig. 56B). The PSC source activity for the heavyweight condition is regularly increasing up to the end of the lowering window in Fig. 56A), and the ACC source activity for has

Figure 55: Source inversion for fatigue effect. A,B) The source time-series are plotted for the sources at the primary sensory (C) and anterior cingulate (D) cortex. The times-series are summarized across subjects and shown in red and blue for fatigue and non-fatigue conditions respectively. The fatigue effect between the two conditions is plotted in green, and the standard error in magenta. C,D) Present the SPM results with the significant voxels in a 3D brain image for the rising (C) and lowering (D) windows which survived alpha threshold of 0.05. Zero is the onset of the lift.

his maximum between both riging and lowering windows as shown in Fig. 56B).

In particular, statistics at the time-series level, table 27, show that both PSC and ACC sources are significant at an alpha level of 0.05, and specifically for the PSC on both left and right hemispheres ($p = 0.002$).

Source	SPM $P_{unc.}$	Location	P_{ts}	Location
		Rising		
ACC Left	0.004	(-26, 30, 26)	0.206	(-18, 32, 32)
ACC Right	0.014	(20, 42, 26)	0.376	(18, 32, 32)
		Lowering		
ACC Left	0.001	(-26, 30, 26)	0.149	(-18, 32, 32)
ACC Right	0.002	(30, 44, 30)	0.133	(18, 32, 32)
PSC Left	0.036	(-18, -44, 62)	0.584	(-10, -38, 70)
PSC Right	0.042	(18, -40, 62)	0.419	(10, 34, 70)

Table 26: Statistics for fatigue effect. The first column describes the source, columns 2 is the uncorrected p-value for the most significant voxel whose location is described in column three. Last two columns are the p-value from the times-series and the center of location for the source. Results are presented for the rising and lowering windows successively. There is no significant source based on the time-series.

Source	SPM $P_{unc.}$	Location	P_{ts}	Location
		Rising		
ACC Left	0.004	(-20, 40, 24)	0.039	(-18, 32, 32)
PSC Left	0.036	(-24, -38, 60)	0.016	(-10, -38, 70)
		Lowering		
ACC Left	0.012	(-24, 32, 30)	0.01	(-18, 32, 32)
PSC Left	0.013	(-22, -42, 64)	0.002	(-10, -38, 70)
PSC Right	0.016	(22, -36, 62)	0.002	(10, 34, 70)

Table 27: Statistics for weight effect. The first column describes the source, columns 2 is the uncorrected p-value for the most significant voxel whose location is described in column three. Last two columns are the p-value from the times-series and the center of location for the source. Results are presented for the rising and lowering windows successively. Significant results from the time-series for an alpha level of 0.05 are presented in red for the ACC and in blue for the sensory cortex.
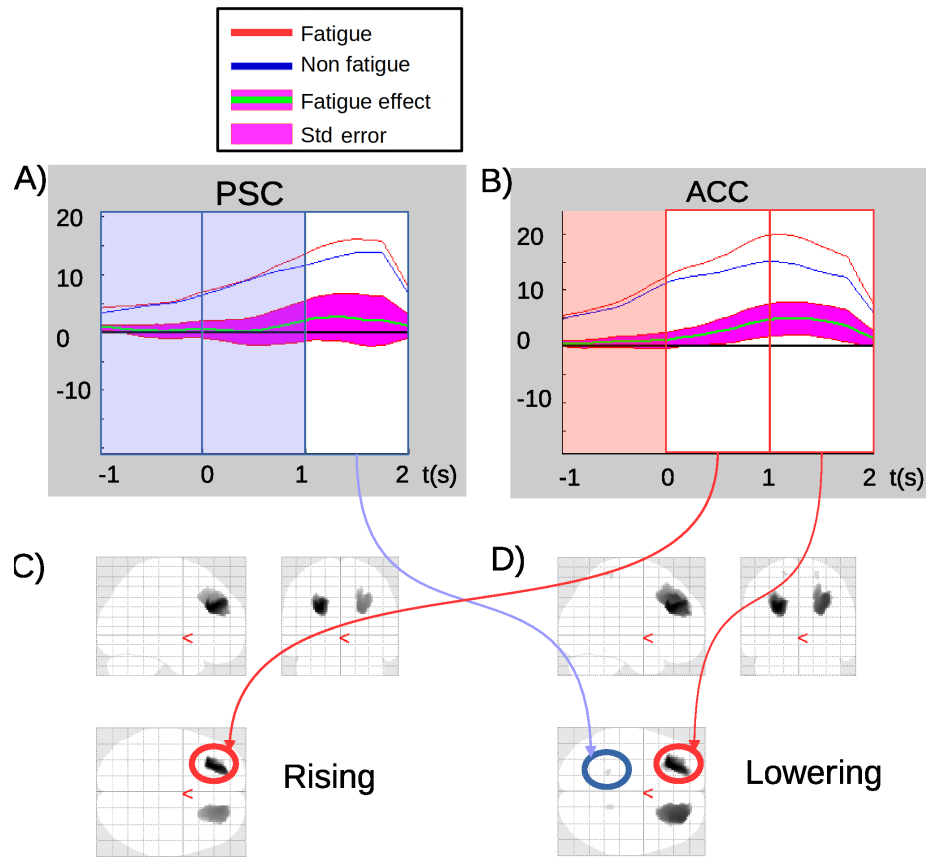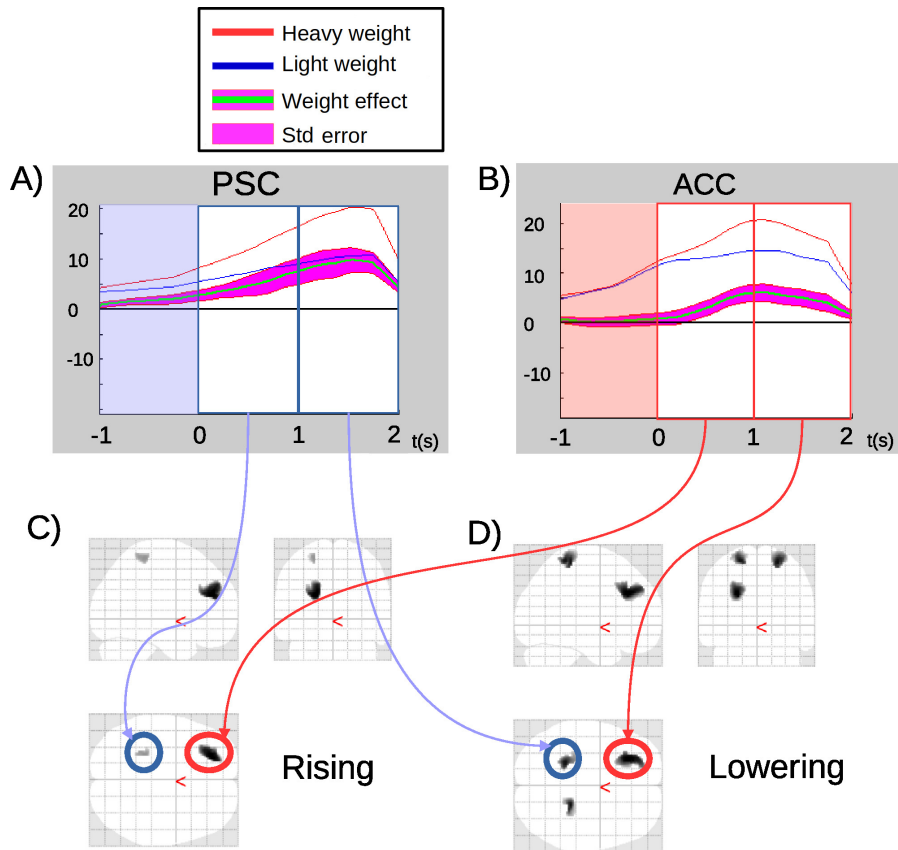
Figure 56: Source inversion for the weight effect. A,B) The source time-series are plotted for the sources at the primary sensory (A) and anterior cingulate (B) cortex. The times-series are summarized across subjects and shown in red and blue for heavyweight and lightweight conditions respectively. The weight effect between the two conditions is plotted in green, and the standard error in magenta. C,D) Present the SPM results with the significant voxels which survived alpha threshold of 0.05, in a 3D brain image for the rising (C) and lowering (D) windows. Zero is the onset of the lift.

7.5.3 Weight x Fatigue Interaction

The interaction between weight and fatigue level is only visible in the PSC as shown in Fig. 57. Mainly, the most significant voxels appear for the lowering window for the left sensory cortex. However, at the source time-series level, PSC statistics are not significant as shown in Table 28 (p¿0.1) which can be due to the high variance between subjects, shown with the standard error in magenta.
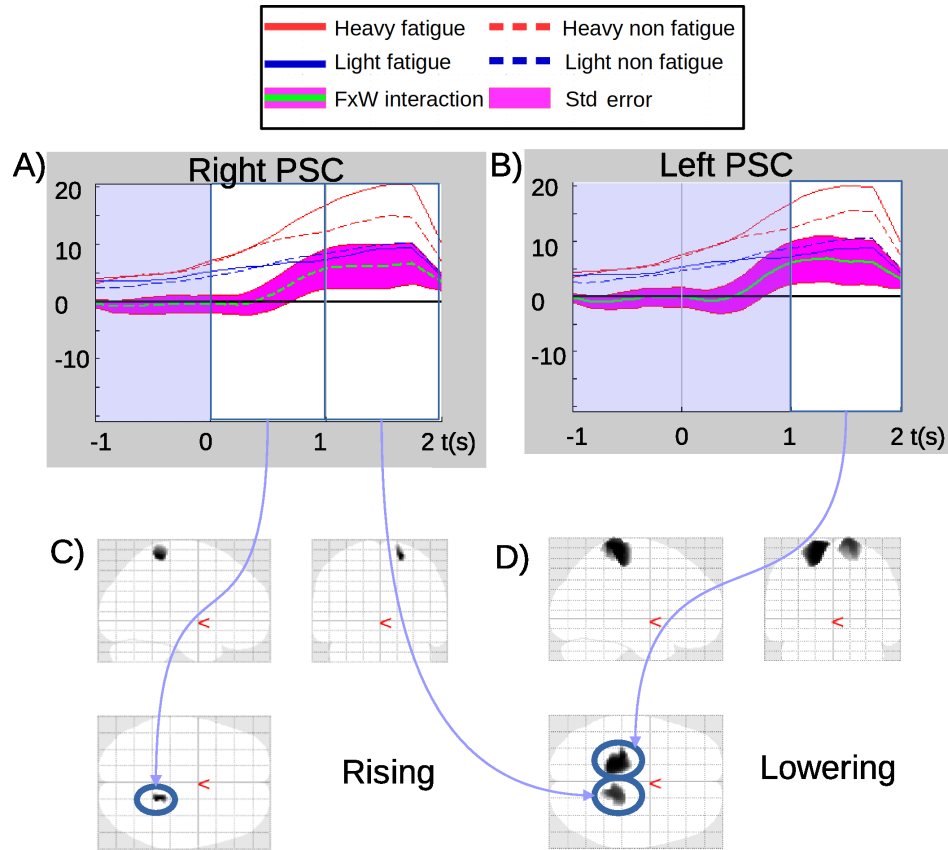
Figure 57: Source inversion for the weight by fatigue interaction. A,B) Source time-series are plotted for the sources at respectively the right (A) and left (B) primary sensory cortex. The times-series are summarized across subjects. Weight by fatigue interaction for the heavyweight condition is shown in red with either the fatigue condition (plain line) or non-fatigue condition (dashed line). The lightweight condition is shown in blue with either the fatigue condition (plain line) or non-fatigue condition (dashed line). The weight by fatigue interaction is plotted in green, and the standard error in magenta. C,D) Present the SPM results with the significant voxels which survived alpha threshold of 0.05 in a 3D brain image for the rising (C) and lowering (D) windows. Zero is the onset of the lift.

7.5.4 Motor Cortex Activity

We present in Fig. 58 the source time-series for the motor-cortex. Respectively weight effect, fatigue effect and weight by fatigue are shown in Figs.58A), B) and C). Because no voxels from the motor cortex were significant at the first

Source	SPM $P_{unc.}$	Location	P_{ts}	Location
		Rising		
PSC Right	0.02	(18, -42, 64)	0.599	(10, 34, 70)
		Lowering		
PSC Left	0.002	(-18, -34, 70)	0.127	(-10, -38, 70)
PSC Right	0.004	(16, -36, 76)	0.103	(10, 34, 70)

Table 28: Statistics for weight by fatigue interaction. The first column describes the source, columns 2 is the uncorrected p-value for the most significant voxel whose location is described in column three. Last two columns are the p-value from the times-series and the center of location related to the source. Results are presented for the rising and lowering windows successively. No significant results from the time-series are available for the interaction.

Source	P_{ts}	Left Location	P_{ts}	Right Location
		Rising		
PMC	0.049	(-20, -14, 70)	0.037	(20, -16, 70)
		Lowering		
PMC	0.029	(-20, -14, 70)	0.031	(20, -16, 70)

Table 29: Statistics from motor cortex source. Statistics for motor cortex are significant only for the weight effect. The results at the source level are presented with the p-value for the left location in column 2 and the p-value for the right location in column 4. Columns 3 and 5 are respectively the center of location for the source. Cells in green are significant results for the motor cortex.

level analysis in the source space the time-series for the motor cortex were not presented. Table 29 present the significant effects for this source. Only the weight effect is significant and for both rising window and lowering window. Fatigue and weight by fatigue interaction have high standard error which explains the lack of significance. The maximum of activity for the motor cortex source occurs during the beginning of the rising period for both fatigue and weight factors.
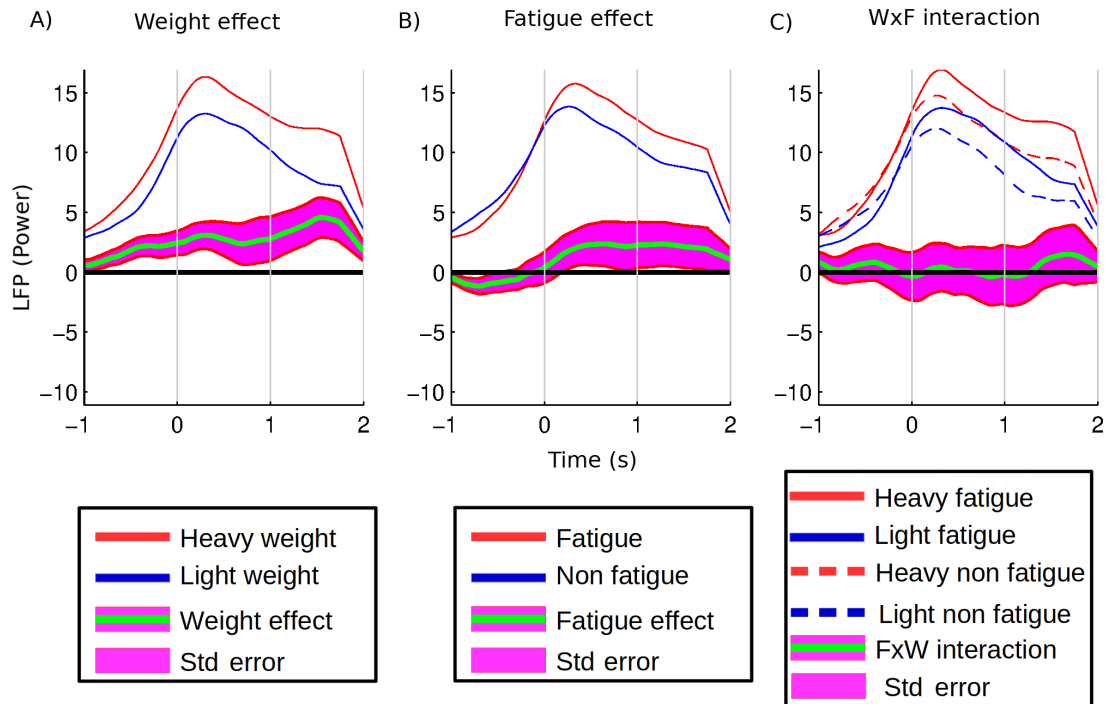
Figure 58: Time-series from the primary motor cortex. Time-series for weight effect A), fatigue effect B) and weight by fatigue interaction C) are presented for the left motor cortex. The effect or interaction is shown in green with standard error in magenta. In the left panel for the weight effect, the time-series for the heavyweight condition is in red and for the light one in blue. In the middle panel for the fatigue effect, the time-series for the fatigue condition is in red and for the non-fatigue in blue. The right panel for weight by fatigue interaction shows the heavy condition in red with either the fatigue condition (plain line) or non-fatigue condition (dashed line). The light condition is in blue with either the fatigue condition (plain line) or non-fatigue condition (dashed line).

7.6   Discussion

For the significant voxels at the first level threshold in source space, we explored significant sources from the time-series, particularly for the rising and lowering windows. For all the sources (except right hemisphere during rising window), weight effect is significant in both rising and lowering windows. This shows that brain is sensitive to external condition and different weight lifting as an important

effect in the brain processing.

Analyses at the scalp level reveal a significant fatigue effect, this is no more the case at the source level. This can be explained as the scalp activity has been decomposed in several sources in the brain. Also, as shown in 58, the standard error is relatively important for the fatigue effect which explains the absence of significant effect. Because we applied source inversion in a subset of mask in the neocortex, we do not know if more deep sources can be significant for the fatigue effect. Different models could be used and compare with Bayes factor.

From the three sources we explored, there is a peak of activity initially in the motor cortex, during the lift i.e. in the rising window. It can be understood as the motor cortex initiate the weight lifting. Then between the rising and lowering window the maximum is reached in ACC area. The ACC is known to be related to decision making, and can be proposed as a marker of motor control as its peak corresponds with the beginning of the lowering period. Finally, the primary sensory cortex shows an increase of activity from the beginning of the time-series which peaks in the middle of the lowering window. The sensory cortex may be implied in the feedback of the sensory-motor loop as described by the particularly high weight effect(Fig. 56A)).

This research rise important questions both in sport science and in fatigue research. Indeed, we show in our work that lifting different weights present different neural signatures in the brain, with a significant difference in PSC between a light and heavy weight. One can think of a training program to help lifting weights. Further research should be done to evaluate if expert weightlifter present this difference. Without difference with expert weightlifter, we can think of one class classifier being able to distinguish expert weightlifter at an individual level. Similarly, this would be able to train people toward this class of expert, compared to

a class of naive or untrained weightlifter. On the source time-series we have been able to show that primary motor cortex could be used to differentiate different levels of weights.

Another aspect of research is related to fatigue. The hypothesis was to find neural correlates of fatigue during the experiment. We didn't find any significant difference at the source level, but the trajectory of fatigue is initially more important in primary motor cortex with a peak at the beginning of the rising period. Then, the peak of fatigue is the latest in cingulate cortex, occurring during the middle of the lowering period. We can think that reducing the peak in ACC would reduce effect of fatigue, but more experiment design should be investigate to first find a strong bio-marker of fatigue.

Chapter 8

Conclusion and Future Directions

8.1 Summary

In previous chapters, we presented results to evaluate different cognitive states, from lower states of unawareness to higher states of expert athletes. In this chapter, we will give a summary of the results to show that different mental states can be distinguished using different methodologies. In particular, we highlight the three-phases theory of the local-global task and discuss how they can be involved in a larger perspective of dynamical causal modelling. Finally, we discuss what are the future directions that can be taken to improve both brain states identifications and understanding of cognitive mechanisms involved in perception and consciousness.

In this thesis, we first presented a review of an EEG-based mental states identification framework (Witon et al. 2016). Then we showed different approaches to distinguish different cognitive states. First between Coma and QBD by applying phase synchrony. Then, using methods for source reconstruction, we presented the effect of sedation on the local-global experiment. For normal awake states, brain patterns were extracted to distinguish for different weight lift experiments. Using spectral power, we distinguished brain states between endurance cycling and sprinter cycling. We show in this thesis that healthy or pathological mental states can be distinguished using the same framework. To be more specific, two types of analyses have been applied.

The first is related to the induced states of brain activity. In these analyses, the brain signal is not locked to a specific stimulus. A global brain property was analysed, as with the phase synchrony to distinguish between QBD or coma (Li et al. 2014; Berthelot, Witon and Li 2017) presented in chapter 3. On these analyses we showed a lower synchrony index for quasi-brain-death and particularly a significant difference between both conditions for delta-alpha and theta-alpha cross-frequency coupling. With spectral power analysis we have been able to distinguish between endurance cycling or sprinter cycling (Witon et al. 2015a,b) presented in chapter 6. In particular, we have shown that higher frequency in occipital allows finding differences between both conditions. In the frontal region, the lower frequency is significant between these two conditions.

Second, based on the evoked activity of the brain, either from ERP or MRCP, we analysed neural processing of the brain. In these conditions, subjects were performing experimental task i.e. local-global with sedation with results shown in chapters 4 and 5 or lift task analysis studied in chapter 7. With the lift experiment, an effect of weight is found during both the rising period and the lowering period

for the different sources. Interestingly the time-course at the source level, for both fatigue effect and weight effect, reveals a peak in successively the motor cortex, anterior cingulate cortex and sensory cortex. This reveals the action of each neural source during the cognitive process of the lift task. Dynamical causal modelling would provide more information on effective connectivity as a future direction.

By using source reconstruction, we were able to highlight which sources were implicated in the different conditions (Witon et al. 2017, 2018). With ECD analysis, two levels of inference were applied to find 1) best parameters of ECD given a particular model. 2) By applying model comparison we tested different models for local deviant and global deviant condition. We highlight in the next section the key findings of the local-global analysis.

8.2 Predictive Coding and Global Workspace Theory

The relationship between subjective experience and consciousness is supported by the predictive coding framework which suggests that a brain is a predictive machine trying to make the best evaluation model of the external world (Friston 2010). On the other-hand, to sustain a conscious activity, a large network needs to be activated as proposed by the global neuronal workspace shown in Fig. 2.

With the source inversion framework applied to the local-global paradigm modulated by sedation, we found a three phases activation between auditory sensory input and attentional awareness, as shown in Fig. 46.

The early effect, as a local response to auditory irregularity, presents activation in the superior-temporal region. This is the first phase related to the sensory

circuit in Fig. 46A). This phase includes the sensory processing which acts in a short time frame. Its key response is the feed-forward propagation of a bottom-up prediction error send to the second phase.

We found a significant fronto-temporal network of clusters for the local by global interaction which is related to the phase 2 as a gateway circuit. We make the hypothesis that this circuit is crucial to do the transition between the sensory processing and a global workspace 'ignition'. More information on the characteristics of this circuit should be studied. We proposed two versions, Figs. 46 B.V1 and B.V2 depending on the direction of the modulatory effect. This gateway circuit exhibits a more phasic response but is not meta-stable as a global workspace.

The late effect shows a network involving frontal and parietal brain areas related to the spanning circuit in Fig. 46C). This network involves a large brain-scale activation, spanning the cortical sheet similarly to the global workspace.

To be more accurate on the gateway circuit, the local by global interaction in the middle window suggests a neural pathway between superior temporal gyrus and inferior frontal areas. With the former of these implementing circuits realising sensory prediction and which underlie the local effect, and the latter implicated in higher order processing, which integrates over a longer temporal extent. This network may effectively be a sub-circuit of the brain spanning global workspace, being a transition state on the way to it, as proto-workspace. Although further work should be required to confirm the hypothesis, it might be argued that this interaction is suggestive of bidirectional exchanges between layers in a predictive hierarchy, with the multiplicative interaction between levels suggestive of modulation of gain control. Under predictive coding, this could be generated by feedback of precision.

The local-global experiment had been modulated by sedation. A sedation

effect was found in the early window and observed in temporal sources. However, we failed to find any sedation effect in parietal areas which might seem surprising as parietal has been argued to be the site of conscious experience. Null effects are difficult to interpret, and there is the possibility of a more highly powered experiment that would find an effect at parietal.

Finally, the most interesting effect was the local by global by sedation, which was significant in the late window. This three-way interaction was observed at an inferior frontal source. When decomposed into its two-way simple effect: local by global when sedated and when recovered as shown in Fig. 44, then there is a clear effect of sedation for the simple local by global interaction.

It seems then that sedation impairs this capacity to detect deviance intrinsically at higher levels, at least at inferior frontal sources. This finding is in many respects consistent with the intent of the local-global task, i.e. to differentiate processing that requires temporally sustained integration over an extended period of time and the role of consciousness in this temporally extended accumulation. Thus, our findings provide suggestive evidence that, in respect of the action of propofol, reduced awareness diminishes long duration processing of temporal integration, supported by inferior frontal sources.

From a predictive coding perspective, the sedation effect provides a multiplicative gain on the prediction error i.e decreased precision (inverse of variance), that reduces the reliability of the sensory input. With sedation, the brain is less likely to react to the global effect.

Further work should be done to understand the link of the sedation effect between inferior frontal to temporal areas. In studies with vegetative patients (Boly et al. 2012), authors suggest that patients with impaired consciousness exhibit a

reduction in effective connectivity from inferior frontal to superior temporal regions as a feedback link. Then, two different manifestations of reduced awareness (vegetative state and sedation) seem to impact the same brain network. Further analyses using dynamical causal modelling could be investigated to have a more accurate view of the effective modulatory effect. This would enable to reply to the question presented in Fig. 46, panel B) about the direction of the modulatory effect.

8.3 Future Directions on Identification of Consciousness

States of consciousness was described as a two-dimensional space, as shown in Fig. 1. The first axis along the x-coordinate represents the level of consciousness, in term of wakefulness. The second axis on the y-coordinate stands for the content of consciousness, or awareness. This is relevant for disorders in states of consciousness, like vegetative states where there is a normal level of wakefulness but very low-level of awareness. Also, from this state to the state of higher awareness, one go through minimal consciousness up to normal conscious state (Laureys et al. 2010; Laureys and Schiff 2012).

However as shown in Fig. 59 in green, the main states during the lifetime of a healthy person should balance from deep sleep to drowsiness up to conscious wakefulness. In regard to these states, another description for consciousness can be proposed using the axis in which consciousness is the mostly represented i.e. from deep sleep to conscious wakefulness. This is proposed in Fig. 59 with the new axis in the diagonal of the graph. The second component is set-up in the
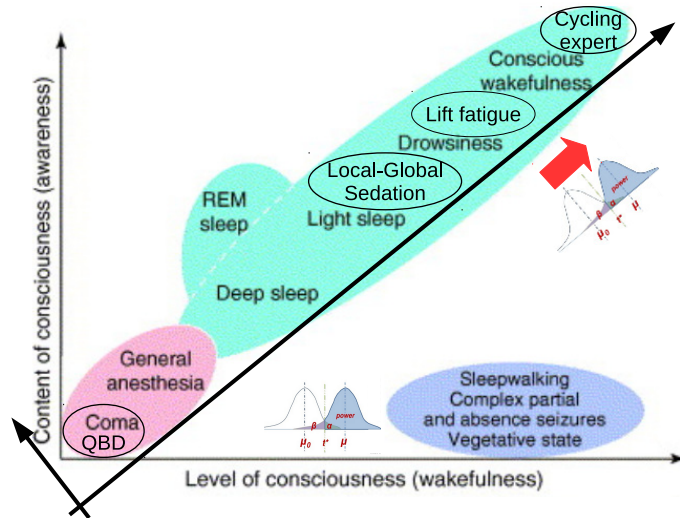
Figure 59: A new proposition on overview of mental states. From original proposition in (Laureys 2005), another dimension of consciousness can be proposed based on the different states (in green) oneself go through during the daily life, from deep sleep to conscious wakefulness.

orthogonal direction. This new dimensional space may increase the power of the statistical test between different states, as shown with the red arrow.

Features like phase synchrony, based on entropy measure is good candidates for consciousness identification as shown to distinguish between coma and QBD. Recently, a feature called Perturbation Complexity Index (PCI) has been proposed as a marker of consciousness (Casali et al. 2013). This feature is based on Transcranial Magnetic Stimulation (TMS) to bypass stimulation of the brain by the conventional sensory input. This stimulation engages distributed interaction of the brain as a step called integration. The second step compresses the spatio-temporal pattern of the cortical responses to measure their complexity. PCI reliably discriminated the level of consciousness in a single individual during

wakefulness, sleep and anaesthesia.

Features like spectral analysis have been able to distinguish different type of elite athletes. Further brain network analysis is needed to evaluate the relationship between network measures, as centrality, and the brain. It was shown that information flow in the brain represented by a high level of hub centrality is correlated with general intelligence. Then, a correlation between expertise e.g. people which are more skilled and conscious experience could bring more insight into the brain of skilled people (Stam 2014; Vakhtin et al. 2014).

Finally, we may expect to create an atlas which defines and modelizes these different states to be able to decipher the language of the brain. More researches need to be done to find more accurately what distinguish between these different states (coma/QBD, cycling, sedation). However, such an atlas could be used to monitor a log of mental states for a clinical purpose (i.e. subjective levels of sedation, neuro-rehabilitation) or sports training (i.e. to an increased level of achievement in sport).

Appendix A

Acronym

Acc: Accuracy

ANN: Artificial Neural Network

ApEn: Approximate Entropy

BSS: Blind Source Separation

DTF: Direct Transfer Function

ECG: Electrocardiogram

ECD: Equivalent Current Dipoles

EEG: Electroencephalogram

EMG: Electromyogram

EOG: Electro-oculogram

ER: Error Rates

ERP: Event Related Potential

fMRI: functional Magnetic Resonance Imaging

fNIRS: functional Near-Infrared Spectroscopy

GFP: Global Field Power

HRV: Heart Rate Variability

HNV: Hierarchical Naive Bayes ICA: Independent Component Analysis

Kc: Kolmogorov complexity

LDA: Linear Discriminant Analysis

MATB: Multi Attributes Task Battery

MEG: Magnetoencephalogram

MRCP: Muscle Related Cortical Potential

MSP: Multiple Spare Priors

PDC: Partial Direct Coherence

PLV: Phase Locking Value

PVT: Psychomotor Vigilance Task

RSVP: Rapid Serial Visual Presentation

RT: Reaction Times

RVIP: Rapid Visual Information Processing

SVM: Support Vector Machine

TE: Tsallis Entropy

TMS: Transcranial Magnetic Stimulation

Appendix B

Hyper Parallel Computing for ECD

B.1   Description of the HPC

Because the optimisation algorithm requires a large amount of computational power, it was decided to launch the computation on Hyper Parallel Computer (HPC) provided by the University of Kent.

The has a Hyper Parallel Computing (HPC) runs a Matlab$^{\text{©}}$ cluster, described in Fig. 60 and accessible to the research community at Kent[1]. Fig. 60 describes the process to get access to the HPC.

Four different elements are used for the Phoenix cluster. First a remote machine that is used to work on the cluster. This workstation should be connected to the UNICORN machine by the Remote Desktop Protocol (RDP)For example on Linux, one can use FreeRDP[2], and launch the workstation as:

---

[1]Documentation can be found on: https://sharepoint.kent.ac.uk/hpc/_layouts/15/start.aspx#/ HPC Documentation Wiki/PHOENIX/GettingStarted.aspx
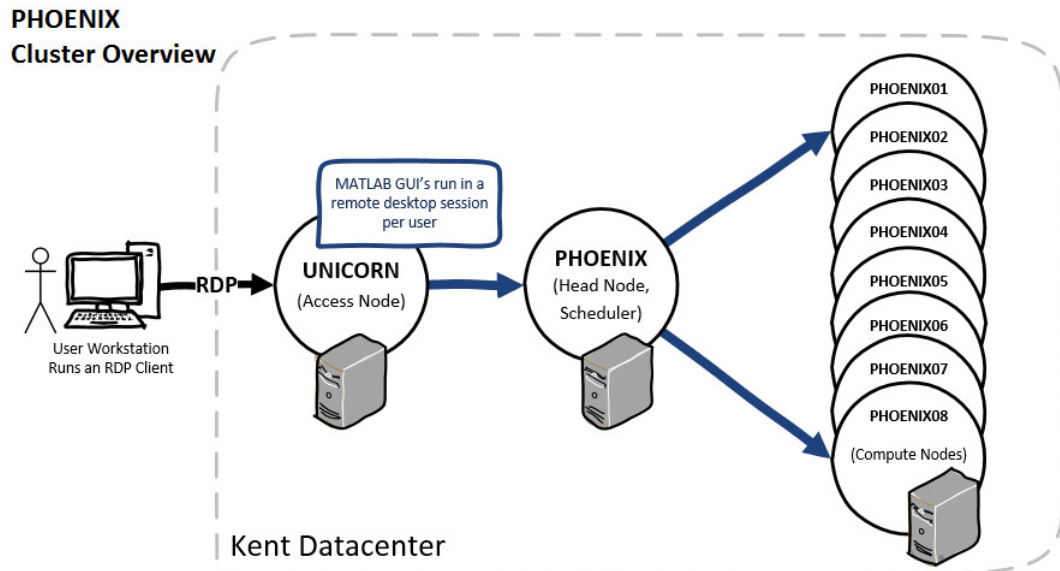
[2]www.freerdp.com

Figure 60: Cluster overview for the Phoenix Hyper Parallel computer at Kent. To run the cluster, the user should first connect to a remote desktop. This workstation runs Matlab on UNICORN, the access node machine. Then the Matlab code runs on Phoenix which includes the scheduler, and the different tasks are dispatched to the 8 phoenix nodes.

```
$xfreerdp unicorn.kent.ac.uk
```

This remote access allows the user to work on UNICORN machine, which provides an access to the Matlb's GUI. Then the third element is the scheduler (head node) which schedules the different tasks to be launched in parallel to the different nodes.

Initialisation should be done on the Matlab interface to create a profile for the Phoenix cluster, to manage the parallel computing to the different nodes. There are 8 different nodes available on the Phoenix cluster, each one have 12 tasks available at the same time. Then there is the possibility to launch simultaneously 96 tasks of the same script, with different parameters or datasets.

Finally, the data files for the analysis are stored in:

```
\\unicorn.ad.kent.ac.uk\userdata\
```

194

B.2   Design procedure for HPC computation

To use the cluster, a job has to be created. This job include multiple tasks, and each task may run several iteration of a final function. Once the job is submitted to the cluster, the scheduler attribute the different tasks to the nodes, and send the results back to Matlab when the job has been completely evaluated. This is summarized in Fig. 61. First, the job can last for days until all tasks are accomplished. One task may take several hours to be performed, and the number of tasks to run in parallel is comprised between 10 to few hundred. Finally, each task run an indefinite number of iteration, each iteration have to be computed in a range of second or minutes to be efficient.
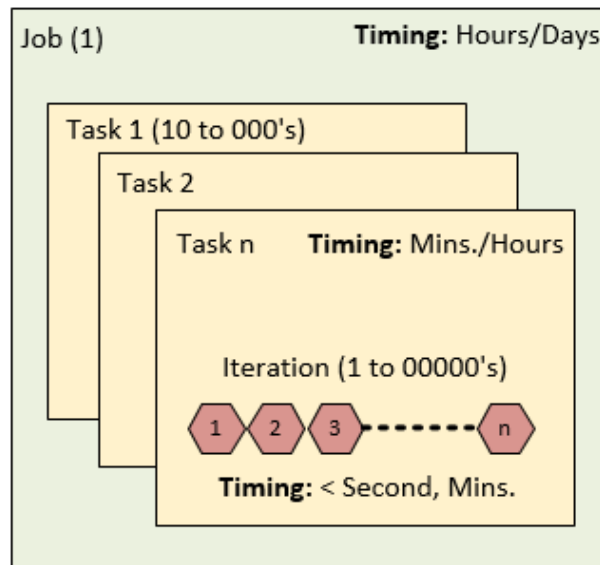

Figure 61: Schematic description of Job, Task and Iteration.

The core part of the HPC is related to the task. This is the element which consume the most time computing power of the HPC. There are eight steps implemented for the cycle of parallel computing process, plus an initialization step used

to prepare the environment. Initialisation requires the number of parallel tasks and the iterations per task that will be used. Below are described the different steps.

- Initialisation During this initialisation is set-up the path for HPC calculation. Also, the parameters for the number of tasks, as well as the number of iteration per task are described.

```
% --- Task configuration constants
files_path = 'U:\userdata\aw448\Documents\MATLAB\LG_MMN\
Code\HPC\HWS\functions ';
        %working files folder under the project folder
log_path = 'logs ';
        % output logs folder under the project folder
num_tasks = NbSubj*NdMod;
        % Number of parallel tasks
opts.task_iter = 20;
        % Iterations per task (in an options structure)
```

The first step is to create a cluster object, related to the cluster registered in the HPC profile of Matlab.

- Step 1: The first step creates a cluster object.

```
clust = parcluster(hpc_profile);   % Run on a HPC Cluster
```

```
clust_job = createJob(clust ,'AttachedFiles ',{ files_path });
```

```
clust_job.AutoAttachFiles = false;   % Speed up
set(clust_job, 'JobData', {opts});   % Job options
```

- Step 3: The third step is to set-up the input parameters for the tasks. In this step, we give a list of cell is given, that is filled with the parameters (inputs), of the tasks. For the ECD source reconstruction, a model with the parameters of the number of dipoles and localisation is provided to each task.

```
task_inputs = cell(1, num_tasks);
for i = 1:num_tasks
        P = Get_DipleLoc(i);
        task_input(i) = P;
end
```

Steps 4, 5, and 6 are successively used: to create the tasks linked to the job, to submit the job to the scheduler, and finally to wait for the job to be done.

- Step 4: This step creates the tasks with the input parameters and task function to use, and link the task to the job.

```
job_task = createTask(clust_job, @ecd_task, 2, task_inputs);
```

- Step 5: On this step, the the job is submitted to the cluster queue, and managed by the scheduler. This is during this step that the HPC starts running the code on the available nodes.

```
submit(clust_job);
```

- Step 6: The code pauses on this step and waits for the job to finish until the cluster queue is empty.

```
wait ( clust_job );
```

- Step 7: Fetch the outputs from job. Once the job is terminated, the results are retrieved. We also check that the state of the job is effectively terminated. Because in some occasion the *wait* function call was terminated while the job was not ready to fetch the results, then if the job is not in a 'finish state', a pause is done until the end of the job.

```
while (~ strcmp ( clust_job . State ,  'finished '))
        pause (2);
end
task_outputs = fetchOutputs ( clust_job );
```

- Step 8: This post-run step is used to retrieve job outputs and display diagnosis. During this step, the results are available in the 'task_output' structure. The output results of interest consist on the models parameters as model evidence and location of dipoles. Others time information are also provided to make some diagnosis on the parallel computing efficiency.

```
for  i = 1:num_tasks      % Process outputs
    P_out_cell = task_outputs ( i ,1);
            % Extract struct from task output
    t_cell   = task_outputs ( i ,2);
            % Extract time from task output
            % Save iteration counts in output vector
    res_vec ( i ,:) =  P_out_cell{1}
```

end

For the HPC on ECD, the main task is:

```
function [Outputs_vect] = ecd_task(P_vect)
        num_runs = jobopts.task_iter;
        for i = 1:num_runs
                Out = spm_eeg_inv_vbecd(P_vect);
                Outputs_vect{i} = Out;
        end
end
```

Which call the SPM function *spm_eeg_inv_vbecd*, to do the inversion based on the parameters from the P_vect with variational Bayes scheme.

Appendix C

Subspace selection and justification for mask placement

Our source localisation analyses have used masks and priors to guide the localisation algorithm. In the absence of structural scans, the provision of what are effectively analysis priors is necessary. We justify the placement of these masks here.

C.1 Local Effect

There is considerable previous literature that presents the generators of the mismatch negativity, which corresponds to our local effect. These prior precedents were reflected in the sources used in Garrido et al, 2008, which are presented in Fig. 62.

The four temporal sources shown in Fig. 62 (lA1, lSTG, rA1 and rSTG) become combined in our analysis into two temporal sources: one on the left and one on the right. In the absence of structural scans, we do not have sufficient temporal
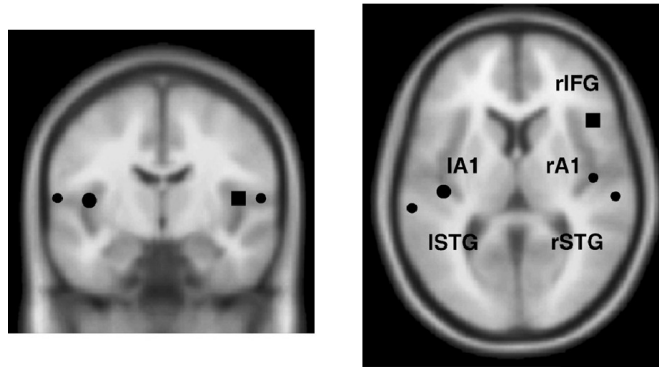
Figure 62: Mask justification for local effect. We present Fig 3 from (Garrido et al. 2008), showing the key MMN sources they use in their DCM fitting.

resolution to distinguish primary auditory cortex from superior temporal gyrus. The central role of superior temporal regions in the MMN is also consistent with the studies of Bekinschtein et al. (2009) and Wacongne et al. (2011), see Figs. 63 B) left panel and C). The Garrido et al work also provides a prior precedent for frontal masks, which include inferior frontal areas, see Fig. 62.

C.2 Global Effect

Localisation precedents for the global effect are somewhat more varied than for the local effect, but nonetheless, there are previous studies that justify placement of broad masks in frontal and parietal regions. Three precedents are shown in Figs. 63 B), C) (middle and right panels) and D) (right panel). As can be seen, a broad range of sources were identified across the cortical sheet, including frontal, parietal and temporal sources.
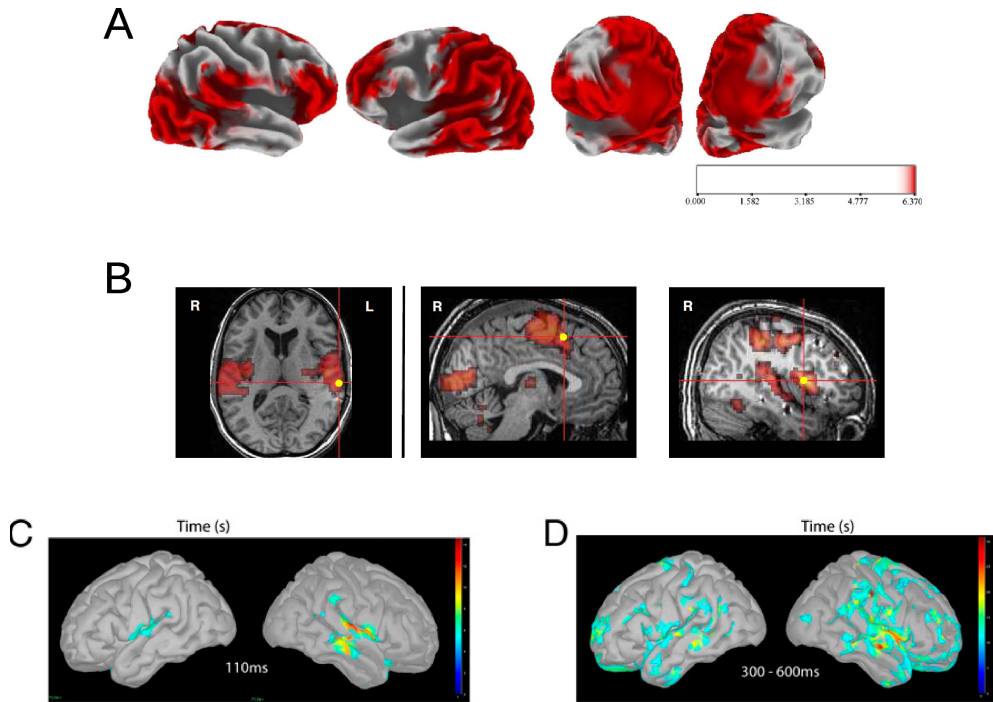
Figure 63: Mask justification for global effect. A) This figure shows panel (A) of Fig 3 of Volpe et al. (2007). The panel presents the generators for the contrast of a non-frequent target against a frequent non-target (i.e. standard). This is the standard P3b condition in odd-ball experiments. B) This figure presents panel (A) of fig 3 of Bekinschtein et al. (2009), which give the results of an fMRI analysis of the local-global task. The leftmost panel presents areas engaged by the local effect, while the middle and right panels shows areas engaged by the global effect. C-D) this figure is from Wacongne et al. (2011), which shows the results of a source localisation of the local-global task. The left panel C) here shows the generators of the local effect, while the right panel D) shows the much more broadly dispersed generators of the global effect.

C.3 Mask localisation

Based on the previous justification, the spheres of the for the ource reconstruction are described in table 30 below.

Name	Hemisphere	Location (x	y	z)	Radius (mm)
Frontal	L	-30	33	10	25
	R	30	33	10	25
A1	L	-42	-22	7	10
	R	46	-14	8	10
STG	L	-61	-32	8	10
	R	59	-25	8	10
Parietal	L	-30	-53	40	25
	R	30	53	40	25

Table 30: Localisation for each mask. The first column indicates the name of the prior mask location. A1: primary auditory cortex, STG: Superior Temporal Gyrus. Then, for either left (L) or right (R) the coordinates are indicated in MNI space. The last column describes the radius of the mask.

Bibliography

Akerstedt, T. and Gillberg, M. (1990). Subjective and objective sleepiness in the active individual. *International Journal of Neuroscience*, 52(1-2), pp. 29–37.

Allen, E. A. et al. (2011). Components of cross-frequency modulation in health and disease. *Front Syst Neurosci*, 5(59).

Anderson, J. et al. (2011). Reproducibility of single-subject functional connectivity measurements. *American Journal of Neuroradiology*.

Baars, B. J. (1988). *A Cognitive Theory of Consciousness*. Cambridge University Press.

Babloyantz, A. and Destexhe, A. (1986). Low-dimensional chaos in an instance of epilepsy. *Proceedings of the National Academy of Sciences*, 83(10), pp. 3513–3517.

Baillet, S. and Garnero, L. (1997). A bayesian approach to introducing anatomo-functional priors in the EEG/MEG inverse problem. *Biomedical Engineering, IEEE Transactions on*, 44(5), pp. 374–385.

Baillet, S., Mosher, J. and Leahy, R. (2001). Electromagnetic brain mapping. *Signal Processing Magazine, IEEE*, 18(6), pp. 14–30.

Barascud, N. et al. (2014). "change deafness" arising from inter-feature masking within a single auditory object. *Journal of Cognitive Neuroscience*, 26(3), p. 514—528.

Bekinschtein, T. A. et al. (2009). Neural signature of the conscious processing of auditory regularities. *Proceedings of the National Academy of Sciences*, 106(5), pp. 1672–1677.

Berthelot, M., Witon, A. and Li, L. (2017). Unconsciousness state identification using phase information extracted by wavelet and hilbert transform. In *2017 22nd International Conference on Digital Signal Processing (DSP)*, pp. 1–5.

Bhattacharya, J. and Petsche, H. (2005). Phase synchrony analysis of EEG during music perception reveals changes in functional connectivity due to musical expertise. *Signal Processing*, 85(11), pp. 2161 – 2177.

Boksem, M. A., Meijmami, T. F. and Lorist, M. M. (2005). Effects of mental fatigue on attention: An ERP study. *Cognitive Brain Research*, 25, pp. 107–116.

Boksem, M. A. and Tops, M. (2008). Mental fatigue: costs and benefits. *Brain Research Review*, 59, pp. 125–139.

Boly, M. et al. (2012). Brain connectivity in disorders of consiousness. *Brain Connectivity*, 2(1).

Borg, G. A. (1982). Psychophysical bases of perceived exertion. *Med Sci Sports Exerc*, 14(5), pp. 377–381.

Borghini, G. et al. (2014). Measuring neurophysiological signals in aircraft pilots

and car drivers for the assessment of mental workload, fatigue and drowsiness. *Neuroscience & Biobehavioral Reviews*, 44(0), pp. 58 – 75.

Braboszcz, C. and Delorme, A. (2011). Lost in thoughts: Neural markers of low alertness during mind wandering. *NeuroImage*, 54(4), pp. 3040 – 3047.

Bressler, S. L. and Seth, A. K. (2011). Wiener–granger causality: A well established methodology. *NeuroImage*, 58(2), pp. 323 – 329.

Brooks, J. L., Zoumpoulaki, A. and Bowman, H. (2017). Data-driven region-of-interest selection without inflating type i error rate. *Psychophysiology*, 54(1), pp. 100–113.

Camkin, H. (1990). Introduction: fatigue and road safety. Road Traffic Authority. In M. Henderson, ed., *Workshop on driver fatigue: report on proceedings.*

Canolty, R. and Knight, R. (2010). The functionnal role of cross-frequency coupling. *Trends in Cognitive Sciences*, 14(11).

Canolty, R. et al. (2006). High gamma power is phase-locked to theta oscillations in human neo-cortex. *Science*, 313, pp. 1626–1628.

Cao, J. and Chen, Z. (2008). *Advanced EEG Signal Processing in Brain Death Diagnosis*, Springer US. pp. 275–298.

Carvalhaes, C. and de Barros, J. A. (2015). The surface laplacian technique in EEG: Theory and methods. *International Journal of Psychophysiology*, 97(3), pp. 174 – 188, on the benefits of using surface Laplacian (current source density) methodology in electrophysiology.

Casali, A. G. et al. (2013). A theoretically based index of consciousness independent of sensory processing and behavior. *Science Translational Medicine*, 5(198), pp. 198ra105–198ra105.

Chennu, S. et al. (2013). Expectation and attention in hierarchical auditory prediction. *The Journal of Neuroscience*, 33(27), pp. 11194–11205.

Comstock, J. R. and Arnegard, R. (1992). The Multi-Attribute Task Battery for human operator workload and strategic behavior research. *NASA Technical Memorandum*.

Cook, D. B. et al. (2007). Functional neuroimaging correlates of mental fatigue induced by cognition among chronic fatigue syndrome patients and controls. *NeuroImage*, 36(1), pp. 108 – 122.

Dale, A. M. and Sereno, M. I. (1993). Improved localization of cortical activity by combining EEG and MEG with MRI cortical surface reconstruction: A linear approach. *Journal of Cognitive Neuroscience*, 5, pp. 162–76.

Dauwels, J. b., Vialatte, F. and Cichocki, A. (2010). Diagnosis of alzheimer's disease from EEG signals: Where are we standing? *Current Alzheimer Research*, 7(6), pp. 487–505.

Davies, D. and Parasuraman, R. (1982). *The Psychology of Vigilance*. London: Academic Press.

de Morree, H. M., Klein, C. and Marcora, S. M. (2012). Perception of effort reflects central motor command during movement execution. *Psychophysiology*, 49(9), pp. 1242–1253.

Dehaene, S. and Changeux, J.-P. (2011). Experimental and theoretical approaches to conscious processing. *Neuron*, 70(2), pp. 200 – 227.

Dehaene, S. et al. (2006). Conscious, preconscious, and subliminal processing: a testable taxonomy. *Trends in Cognitive Sciences*, 10(5), pp. 204 – 211.

Donchin, E. (1981). Surprise!. . . surprise? *Psychophysiology*, 18(5), pp. 493–513.

Enoka, R. M. and Duchateau, J. (2008). Muscle fatigue: what, why and how it influences muscle function. *The Journal of Physiology*, 586(1), pp. 11–23.

Fitts, P. and Posner, M. (1967). *Human Performance*. Brooks-Cole.

Friston, K. (2007). *Statistical Parametric Mapping The Analysis of Functionnal Brain Images*. Karl Friston, John Ashburner, Stefan Kiebel, Thomas Nichols, William Penny.

Friston, K. (2010). The free-energy principle: A unified brain theory? *Nature Reviews Neuroscience*, 11(2), pp. 127–138.

Friston, K., Kilner, J. and Harrison, L. (2006). A free energy principle for the brain. *Journal of Physiology-Paris*, 100(1–3), pp. 70 – 87, theoretical and Computational Neuroscience: Understanding Brain Functions.

Friston, K. et al. (2007). Variational free energy and the laplace approximation. *NeuroImage*, 34(1), pp. 220 – 234.

Friston, K. et al. (2008). Multiple sparse priors for the m/eeg inverse problem. *NeuroImage*, 39(3), pp. 1104 – 1120.

Garrido, M. I. et al. (2008). The functional anatomy of the mmn: A {DCM} study of the roving paradigm. *NeuroImage*, 42(2), pp. 936 – 944.

Gevins, A. et al. (1998). Monitoring working memory load during computer-based tasks with EEG pattern recognition methods. *Human Factor*, 40, pp. 79–91.

Goncharova, I. et al. (2003). EMG contamination of EEG: spectral and topographical characteristics. *Clinical Neurophysiology*, 114(9), pp. 1580 – 1593.

Grandjean, E. (1988). *Fitting the Task to the Man*. Taylor and Francis, London.

Gwizdka, J. (2010). Using stroop task to assess cognitive load. In *Proceedings of the 28th Annual European Conference on Cognitive Ergonomics*, ACM, ECCE '10, pp. 219–222.

Hahn, S. (1996). *Hilbert Transforms in Signal Processing*. Artech House signal processing library, Artech House.

Harris, W. et al. (1995). Performance, workload, and fatigue changes associated with automation. *Int J Aviat Psychol*, 5, pp. 169–185.

Hart, S. and Staveland, L. (1988). *Development of NASA-TLX (Task Load Index): result of empirical and theoretical research*. North-Holland, Amsterdam.

Henson, R. (2015). *Brain Mapping: an Encyclopedic Reference*, vol. 1. Academic Press.

Hilti, C. C. et al. (2013). Evidence for a cognitive control network for goal-directed attention in simple sustained attention. *Brain and Cognition*, 81(2), pp. 193 – 202.

Hoddes, E. et al. (1973). Quantification of sleepiness: A new approach. *Psychophysiology*, 10(4), pp. 431–436.

Hopstaken, J. F. et al. (2014). A multifaceted investigation of the link between mental fatigue and task disengagement. *Psychophysiology.*

Hudetz, B. et al. (2003). Cholinergic reversal of isoflurane anesthesia as measured by cross-approximate entropy of the electroencephalogram. *Anesthesiology*, 99(5), pp. 1125–1131.

Imanishi, A. and Oyama-Higa, M. (2006). The relation between observers' psychophysiological conditions and human errors during monitoring task. In *Systems, Man and Cybernetics, 2006. SMC '06. IEEE International Conference on*, vol. 3, pp. 2035–2039.

Jasper, H. (1958). Report of the committee on methods of clinical examination in electroencephalography: 1957. *Electroencephalography and Clinical Neurophysiology*, 10, pp. 370–375.

Jung, T.-P. et al. (1997). Estimating alertness from the EEG power spectrum. *Biomedical Engineering, IEEE Transactions on*, 44(1), pp. 60–69.

Kanai, R. et al. (2015). Cerebral hierarchies: predictive processing, precision and the pulvinar. *Philosophical transactions of the Royal Society of London Series B, Biological sciences*, 370(1668).

Kiebel, S. J. et al. (2008). Variational bayesian inversion of the equivalent current dipole model in EEG/MEG. *NeuroImage*, 39(2), pp. 728 – 741.

King, J.-R. et al. (2014). Two distinct dynamic modes subtend the detection of unexpected sounds. *PLoS ONE*, 9(1), p. e85791.

Klimesch, W. (1999). EEG alpha and theta oscillations reflect cognitive and memory performance: a review and analysis. *Brain Research Reviews*, 29(2–3), pp. 169 – 195.

Kybic, J. et al. (2005). A common formalism for the integral formulations of the forward EEG problem. *IEEE Transactions on Medical Imaging*, 24(1), pp. 12–28.

Lachaux, J. et al. (1999). Measuring phase synchrony in brain signals. *Human Brain Mapping*, 8, pp. 194–208.

Lal, S. K. and Craig, A. (2001). A critical review of the psychophysiology of driver fatigue. *Biological Psychology*, 55(3), pp. 173 – 194.

Laureys, S. (2005). The neural correlate of (un)awareness: lessons from the vegetative state. *Trends in Cognitive Sciences*, 9(12), pp. 556 – 559.

Laureys, S. and Schiff, N. D. (2012). Coma and consciousness: Paradigms (re)framed by neuroimaging. *NeuroImage*, 61(2), pp. 478 – 491.

Laureys, S. et al. (2010). Unresponsive wakefulness syndrome: a new name for the vegetative state or apallic syndrome. *BMC Medicine*, 8(1), p. 68.

Lehembre, R. et al. (2012). Resting-state EEG study of comatose patients: a connectivity and frequency analysis to find differences between vegetative and minimally conscious states. *Functional Neurology*, 27(1), pp. 41–47.

Li, L. et al. (2012). Phase-based brain consciousness analysis. In *2012 Annual International Conference of the IEEE Engineering in Medicine and Biology Society*, pp. 1032–1035.

Li, L. et al. (2014). Eeg-based brain connectivity analysis of states of unawareness. In *Engineering in Medicine and Biology Society (EMBC), 2014 36th Annual International Conference of the IEEE*, pp. 1002–1005.

Lim, J. et al. (2010). Imaging brain fatigue from sustained mental workload: An ASL perfusion study of the time-on-task effect. *NeuroImage*, 49(4), pp. 3426 – 3435.

Litvak, V. and Friston, K. (2008). Electromagnetic source reconstruction for group studies. *NeuroImage*, 42(4), pp. 1490 – 1498.

Liu, J., Zhang, C. and Zheng, C. (2010a). EEG-based estimation of mental fatigue by using KPCA-HMM and complexity parameters. *Biomedical Signal Processing and control*, 5, pp. 124–130.

Liu, J.-P., Zhang, C. and Zheng, C.-X. (2010b). Estimation of the cortical functional connectivity by directed transfer function during mental fatigue. *Applied Ergonomics*, 42(1), pp. 114 – 121.

Looney, D. et al. (2009). Measuring phase synchrony using complex extensions of emd. In *Statistical Signal Processing, 2009. SSP'09. IEEE/SP 15th Workshop on*, IEEE, pp. 49–52.

Lopez, J. et al. (2014). Algorithmic procedures for bayesian MEG/EEG source reconstruction in SPM. *NeuroImage*, 84, pp. 476 – 487.

Lorist, M. M. et al. (2009). The influence of mental fatigue and motivation on neural network dynamics; an EEG coherence study. *Brain Research*, pp. 95–106.

Luck, S. J. (2005). *An introduction to the event-related potential technique.* MIT Press.

Lutz, A. et al. (2004). Long-term meditators self-induce high-amplitude gamma synchrony during mental practice. *Proceedings of the National Academy of Sciences*, 101(46), pp. 16369–16373.

M Kilner, J., J Kiebel, S. and Friston, K. (2005). Applications of random field theory to electrophysiology. *Neuroscience letters*, 374, pp. 174–8.

Ma, J. et al. (2012). Muscle artefacts in multichannel EEG: Characteristics and reduction. *Clinical Neurophysiology*, 123(8), pp. 1676 – 1686.

Mackay, D. J. C. (2003). *Information Theory, Inference and Learning Algorithms.* Cambridge University Press.

Mackey, M. and Glass, L. (1977). Oscillation and chaos in physiological control systems. *Science*, 197(4300), pp. 287–289.

Mackworth, N. H. (1948). The breakdown of vigilance during prolonged visual search. *Quarterly Journal of Experimental Psychology*, pp. 6–21.

Maguire, E. A., Woollett, K. and Spiers, H. J. (2006). London taxi drivers and bus drivers: A structural MRI and neuropsychological analysis. *Hippocampus*, 16(12), pp. 1091–1101.

Manly, B. F. (2007). *Randomization, Bootstrap and Monte Carlo Methods in Biology.* Chapman & Hall.

Marcora, S. M., Staiano, W. and Manning, V. (2009). Mental fatigue impairs physical performance in human. *Journal of Applied Physiology*, 106, pp. 857–864.

Maris, E. and Oostenveld, R. (2007). Nonparametric statistical testing of EEG and MEG data. *Journal of Neuroscience Methods*, 164(1), pp. 177 – 190.

Marsh, B. et al. (1991). Pharmacokinetic model driven infusion of propofol in children. *BJA: British Journal of Anaesthesia*, 67(1), pp. 41–48.

Mashour, G. A. and LaRock, E. (2008). Inverse zombies, anesthesia awareness, and the hard problem of unconsciousness. *Consciousness and Cognition*, 17(4), pp. 1163 – 1168.

Massar, S. A. et al. (2010). Manipulation specific effects of mental fatigue: Evidence from novelty processing and simulated driving. *Psychophysiology*, 47(6), pp. 1119–1126.

Miller, G. A. (1956). The magical number seven, plus or minus two: Some limits on our capacity for processing information. *The Psychological Review*, 63, pp. 81–97.

Muthukumaraswamy, S. (2013). High-frequency brain activity and muscle artifacts in MEG/EEG: A review and recommendations. *Frontiers in Human Neuroscience*, 7(138).

Naatanen, R., Gaillard, A. and Mantysalo, S. (1978). Early selective-attention effect on evoked potential reinterpreted. *Acta Psychologica*, 42(4), pp. 313 – 329.

Naatanen, R. et al. (2007). The mismatch negativity (mmn) in basic research of central auditory processing: A review. *Clinical Neurophysiology*, 118(12), pp. 2544 – 2590.

Nichols, T. and Hayasaka, S. (2003). Controlling the familywise error rate in functional neuroimaging: a comparative review. *Statistical Methods in Medical Research*, 12(5), pp. 419–446, pMID: 14599004.

Nichols, T. E. and Holmes, A. P. (2002). Nonparametric permutation tests for functional neuroimaging: A primer with examples. *Human Brain Mapping*, 15(1), pp. 1–25.

Niedermeyer, E. and da Silva, F. L. (2005). *Electroencephalography: basic principles, clinical applications, and related fields.* Lippincott Williams & Wilkins.

Paas, F. and Merrienboer, J. (1994). Instructional control of the cognitive load in the training of complex cognitive tasks. *Educational Psychology Review*, 6, pp. 51–71.

Paas, F. et al. (2003). Cognitive load measurement as a means to advance cognitive load theory. *Educational Psychologist*, 38, pp. 63–71.

Papadelis, C. et al. (2007). Monitoring sleepiness with on-board electrophysiological recordings for preventing sleep-deprived traffic accidents. *Clinical Neurophysiology*, 118(9), p. 1906–1922.

Park, H.-J. and Friston, K. (2013). Structural and functional brain networks: From connections to cognition. *Science*, 342(6158).

Paus, T. (2001). Primate anterior cingulate cortex: where motor control, drive and cognition interface. *Nature reviews Neuroscience*, 2(6), p. 417.

Peat, F. D. and briggs, J., eds. (1990). *Turbulent Mirror: An Illustrated Guide to Chaos Theory and the Science of Wholeness.* HarperCollins Publishers Inc.

Penny, W. et al. (2004). Comparing dynamic causal models. *NeuroImage*, 22(3), pp. 1157 – 1172.

Pincus, S. M. (1991). Approximate entropy as a measure of system complexity. *Proceedings of the National Academy of Sciences*, 88(6), pp. 2297–2301.

Polich, J. (2007). Updating p300: An integrative theory of p3a and p3b. *Clinical Neurophysiology*, 118(10), pp. 2128 – 2148.

Polich, J. and Criado, J. R. (2006). Neuropsychology and neuropharmacology of P3a and P3b. *International Journal of Psychophysiology*, 60(2), pp. 172 – 185, models and Theories of Brain Function with Special Emphasis on Cognitive Processing.

Posner, M. I. and Raichle, M. E. (1994). *Images of Mind*. Scientific American Library.

Prins, J. B., Van der Meer, J. W. M. and Bleijenberg (2006). Chronic Fatigue Syndrome. *Lancet*, 367, pp. 346–355.

Prue, G. et al. (2006). Cancer-related fatigue: a critical appraisal. *European Journal of Cancer*, 42, pp. 846–863.

Rao, R. P. and Ballard, D. H. (1999). Predictive coding in the visual cortex: a functional interpretation of some extra-classical receptive-field effects. *Nature neuroscience*, 2(1), pp. 79–87.

Richman, J. S. and Moorman, J. R. (2000). Physiological time-series analysis using approximate entropy and sample entropy. *American Journal of Physiology - Heart and Circulatory Physiology*, 278(6), pp. H2039–H2049.

Roy, R. N. et al. (2013). Mental fatigue and working memory load estimation: Interaction and implications for EEG-based passive BCI. In *35th Annual International Conference of the IEEE EMBS*, pp. 6607–6611.

Rubio, S. et al. (2004). Evaluation of subjective mental workload: A comparison of SWAT, NASA-TLX, and Workload Profile Methods. *Applied Psychology: an international review*, 53, pp. 61–86.

Schorr, B. et al. (2016). Coherence in resting-state EEG as a predictor for the recovery from unresponsive wakefulness syndrome. *Journal of Neurology*, 263(5), pp. 937–953.

Schrouff, J. et al. (2011). Brain functional integration decreases during propofol-induced loss of consciousness. *NeuroImage*, 57(1), pp. 198 – 205.

Shannon, C. and Weaver, W. (1949). *The mathematical theory of communication*. Illinois Press.

Shirazi-Beheshti, A. et al. (2018). Placing meta-stable states of consciousness within the predictive coding hierarchy: the deceleration of the accelerated prediction error. *Consciousness and Cognition*.

Smith, E. E. and Jonides, J. (1999). Storage and executives processes in the frontal lobes. *Science*, 283, pp. 1657–1661.

Spruston, N. (2008). Pyramidal neurons: dendritic structure and synaptic integration. *Nature Reviews Neuroscience*, 9(3), pp. 206 – 221.

Stam, C. J. (2014). Modern network science of neurological disorders. *Nature Reviews Neuroscience*, 15, p. pages 683–695.

Sun, Y. et al. (2014). Functional cortical connectivity analysis of mental fatigue unmasks hemispheric asymmetry and changes in small-world networks. *Brain and Cognition*, 85(0), pp. 220 – 230.

Tass, P. et al. (1998). Detection of $n : m$ phase locking from noisy data: Application to magnetoencephalography. *Physical Review Letters*, 81(15), pp. 3291–3294.

Thayer, R. E. (1989). *The biopsychology of mood and arousal.* Oxford University Press.

Touryan, J. et al. (2014). Estimating endogenous changes in task performance from EEG. *Frontiers in Neuroscience*, 8(155).

Tran, Y. et al. (2007). Detecting neural changes during stress and fatigue effectively: a comparison of spectral analysis and sample entropy. In *Neural Engineering, 2007. CNE '07. 3rd International IEEE/EMBS Conference on*, pp. 350–353.

Vakhtin, A. A. et al. (2014). Functional brain networks contributing to the parieto-frontal integration theory of intelligence. *NeuroImage*, 103, pp. 349 – 354.

Varela, F. et al. (2001). The brainweb: Phase synchronization and large-scale integration. *Nature Reviews Neuroscience*, 2, pp. 229–239.

Varela, F. J. (1994). Resonant cell assemblies: a new approach to cognitive functions and neuronal synchrony. *Biological Research*, 28(1), pp. 81–95.

Volpe, U. et al. (2007). The cortical generators of p3a and p3b: A loreta study. *Brain Research Bulletin*, 73(4–6), pp. 220 – 230.

Wacongne, C. et al. (2011). Evidence for a hierarchy of predictions and prediction errors in human cortex. *Proceedings of the National Academy of Sciences*, 108(51), pp. 20754–20759.

Walter, W. et al. (1964). Contingent negative variation : An electric sign of sensori-motor association and expectancy in the human brain. *Nature*, 203(4943), pp. 380–384.

Wascher, E. et al. (2014). Frontal theta activity reflects distinct aspects of mental fatigue. *Biological Psychology*, 96(0), pp. 57 – 65.

Wessely, S., Hotpf, M. and Sharpe, M. (1998). *Chronic fatigue and its syndromes*. Oxford University Press.

Wickens, C. D. (2002). Multiple resources and performance prediction. *Theoretical issues in ergonomics science*, 3(2), pp. 159–177.

Witon, A., Bowman, H. and Li., L. (2018). Investigating the within-frequency and cross-frequency phase synchrony for unconsciousness with a strategy to correct multiple comparison problem.

Witon, A. et al. (2015a). EEG brain waves during cognitive load reveal differences of cycling expertise. In *Brain Informatics & Health*, pp. 1–3.

Witon, A. et al. (2015b). EEG difference between cortical activity in endurance and and sprinter elite cycling athletes. In *1st Endurance Research Conference*, pp. 1–3.

Witon, A. et al. (2016). Review on EEG-based detection of mental fatigue. *In preparation*.

Witon, A. et al. (2017). Un-mixing components of a hierarchical auditory paradigm from EEG source reconstruction. In *British Association for Cognitive Neuroscience 2017*, p. 1.

Witon, A. et al. (2018). Localising the local-global : Fronto-temporal sources and propofol modulation of the double surprise acceleration. *To be submitted*.

Yarrow, K., Brown, P. and Krakauer, J. W. (2009). Inside the brain of an elite athlete: the neural processes that support high achievement in sports. *Nature Reviews Neuroscience*, 10(8), pp. 585–596.

Zhang, C. et al. (2014). Phase synchronization and spectral coherence analysis of EEG activity during mental fatigue. *Clinical EEG and Neuroscience*, 45(4), pp. 249–256.

Zhao, C. et al. (2012). Electroencephalogram and electrocardiograph assessment of mental fatigue in a driving simulator. *Accident Analysis & Prevention*, 45(0), pp. 83 – 90.